POLITECNICO DI MILANO

Facoltà di Ingegneria dei Sistemi
Corso di Laurea Magistrale in Ingegneria Fisica
Dipartimento di Fisica

SINGLE PHOTON ACQUISITION IN CCD DETECTORS FOR HIGH RESOLUTION RESONANT INELASTIC SOFT X-RAY SCATTERING

RELATORE: Prof. Giacomo Claudio GHIRINGHELLI

CORRELATORE: Prof. Lucio BRAICOVICH

Tesi di Laurea di:
Andrea AMORESE
Matr. Nr. 783125

Anno Accademico 2012/2013

Contents

List of Figures

List of Tables

Sommario

Lo scattering anelastico risonante di raggi X (RIXS - Resonant Inelastic X-ray Scattering) è una tecnica spettroscopica basata sull'utilizzo della radiazione di sincrotrone che ha dimostrato, nel corso degli ultimi 15 anni, le sue enormi potenzialità per lo studio della struttura elettronica e magnetica di solidi cristallini e di singole molecole. Il campo di applicazione che maggiormente ha beneficiato delle esclusive proprietà del RIXS è lo studio delle proprietà elettroniche e magnetiche di composti contenenti metalli di transizione o terre rare. Tale tecnica spettroscopica offre infatti la possibilità di studiare le eccitazioni elementari di questi materiali con risoluzione in momento ed energia. Essendo una tecnica risonante e utilizzando fotoni sia in ingresso che in uscita dal materiale, essa permette inoltre di discriminare gli elementi e il loro stato di ossidazione, di sondare il volume del campione e di mantenerne la neutralità di carica.

Una delle applicazioni più recenti ed originali del RIXS ha portato alla scoperta di modulazioni della densità di carica in cuprati superconduttori ad alta temperatura critica, in particolare in campioni di YBCO con bassi drogaggi. In questa tesi verranno presentati alcuni risultati recenti che mostrano la presenza di onde di densità di carica (charge density waves - CDW) anche in Bi2212 con drogaggi ottimali. Si tratta di una scoperta molto importante che può aiutare a far luce sulla natura di questi ordinamenti di carica e sulle proprietà della regione del diagramma di fase denominata *pseudogap* in cui le CDW sono state finora rilevate. Un ruolo fondamentale per tale scoperta è da attribuirsi alla risoluzione in energia del RIXS, che ha permesso di riconoscere anche le più piccole modulazioni del picco elastico, separando il suo contributo dal resto dello spettro.

Essendo questa tecnica così promettente, molti dei principali sincrotroni di tutto il

mondo stanno in questi anni progettando e costruendo molti strumenti dedicati al RIXS, dotati di una sempre migliore risoluzione in energia e di controllo sulla posizione angolare del campione. In questo contesto, il gruppo guidato dal Prof. Giacomo Ghiringhelli e dal Prof. Lucio Braicovich presso il Politecnico di Milano ha contribuito alla progettazione e costruzione di un nuovo spettrometro RIXS ad alta risoluzione per raggi X soffici, chiamato ERIXS, che sarà in funzione dal 2014 sulla beamline ID32 dell'European Synchrotron Radiation Facility (ESRF) a Grenoble. Il gruppo ha una lunga esperienza nel campo, avendo già progettato gli spettrometri AXES, montato sulla beamline ID08 a ESRF, e SAXES, montato sulla beamline ADRESS al Synchrotron Light Source (SLS) di Villigen. Entrambi questi spettrometri hanno avuto un'influenza cruciale sul successo del RIXS, avendo fornito i risultati più importanti raggiunti negli ultimi 10 anni dal RIXS con raggi X soffici.

Lo spettrometro ERIXS su ID32 è stato progettato per migliorare la risoluzione energetica di 5 volte rispetto ad AXES su ID08, mentre per quanto riguarda il conteggio di fotoni è previsto un aumento di intensità del segnale di un fattore superiore a 3. Si tratta di prestazioni senza precedenti, che possono essere raggiunte solo attraverso la massima ottimizzazione di tutti i componenti della beamline e dello spettrometro. In tale contesto si inquadra il lavoro descritto in questa tesi, che riguarda una innovativa modalità di utilizzo del detector CCD già in uso su AXES. Per effettuare una spettroscopia RIXS l'energia dei fotoni diffusi dal campione viene determinata disperdendoli attraverso un reticolo diffrattivo e rilevando l'intensità in funzione dell'angolo di dispersione mediante un detector sensible alla posizione. Uno dei fattori cruciali per lo spettrometro è pertanto la risoluzione spaziale del detector.

I sensori di immagine più utilizzati per applicazioni con raggi X, grazie al loro basso rumore, alta efficienza e versatilità, sono i rilevatori che utilizzano i cosiddetti dispositivi ad accoppiamento di carica e prendono il nome, dall'inglese, di charge coupled device (CCD) detectors. Si è dimostrato che la risoluzione spaziale di tali sensori commerciali, per quanto rigarda la rilevazione di raggi X soffici, è rappresentata da una gaussiana larga circa 25 μm a metà altezza, indipendentemente dalla dimensione dei pixel. L'assorbimento di un fotone nello strato attivo alla superficie del detector porta all'eccitazione di un gran numero di elettroni in banda di conduzione, i quali generano una *nuvola* di carica libera all'interno del materiale attorno alla

posizione di impatto del fotone. Tale nuvola viene attratta dalle buche di potenziale generate dai pixel fisici fabbricati nel wafer di silicio e, durante la deriva, diffonde. Come conseguenza della diffusione, la nuvola di carica si espande e può arrivare a occupare diversi pixel vicini generando una *macchia* sulle immagini che limita la risoluzione spaziale del sensore. D'altra parte, su queste macchie si possono utilizzare tecniche di ricostruzione del centroide per determinare l'esatta posizione di impatto dei fotoni, raggiungendo in questo modo una risoluzione migliore anche della dimensione del pixel.

Questa tesi descrive lo sviluppo e le prime prove di un algoritmo che permette un significativo miglioramento della risoluzione spaziale delle immagini del detector, attraverso un calcolo del centro delle macchie generate da ogni singolo fotone. Questa tecnica prende il nome di ricostruzione del centroide a conteggio di singolo fotone. La determinazione della posizione di impatto del fotone è basata sul calcolo del *centro di massa* (center of mass – COM) del gruppo di pixel contenente la macchia, effettuato eseguendo una media delle posizioni dei pixel pesate sul segnale accumulato dentro a ciascuno di essi. Al fine di valutare le effettive prestazioni del codice sviluppato, come la risoluzione spaziale e la velocità di elaborazione, nonché studiare le possibili limitazioni causate della sovrapposizione di macchie adiacenti, è stato effettuato un test di risoluzione nei laboratori del Politecnico di Milano, utilizzando una sorgente X tradizionale. L'apparato sperimentale permette una misura molto diretta della risoluzione, analizzando sulle immagini acquisite dal CCD la nettezza dell'ombra del bordo tagliente di una lametta illuminata dalla lampada X. Il detector utilizzato per questi test è un CCD della Princeton Instrument (PI-SX 1300, dimensione dei pixel 20 μm), utilizzato a ESRF fino a pochi anni fa per lo spettrometro AXES. Oltre a tale prova sperimentale, il codice è stato sottoposto a ulteriori test su immagini "virtuali" ottenute attraverso simulazioni Monte Carlo del processo che porta alla generazione delle nuvole di carica. In questo modo le prestazioni del programma sono state sperimentate sotto condizioni completamente controllabili ed è stato possibile simulare indipendentemente gli effetti sui risultati finali dovuti alle dimensioni dei pixel, alla larghezza della nuvola di carica e al rumore di lettura. La risoluzione raggiunta è ottima in entrambi i test, essendo di circa 7 μm con i dati sperimentali e 2 μm nel caso ideale delle simulazioni. Il valore sperimentale è da considerarsi eccellente perché

raggiunge l'obbiettivo di 10 μm di risoluzione richiesti per garantire le prestazioni ottimali di ERIXS. Il limite teorico di 2 μm, sebbene ottenuto trascurando l'effetto del rumore di lettura, dimostra che sono ancora possibili ampi margini di miglioramento. La discrepanza dei risultati tra simulazioni e esperimenti può essere attribuita, almeno in parte, a limitazioni geometriche nel sistema ottico utilizzato per i test.

Nonostante i risultati incoraggianti sulla risoluzione, alcuni artefatti sono stati osservati nelle immagini finali a seguito dell'elaborazione, causati da possibili errori legati al calcolo del centro di massa. Tali errori possono verificarsi quando i pixel più esterni di una macchia sono esclusi dal calcolo, o quando il loro segnale è coperto dal rumore. Alcuni metodi per eliminare questi artefatti sono in studio durante la scrittura di questa tesi e fanno ben presagire per l'eliminazione completa del problema.

Un altro problema relativo all'uso del programma per applicazioni spettroscopiche con luce di sincrotrone nasce dalla richiesta di una bassa densità di fotoni sulle immagini da analizzare. Infatti, la ricostruzione del centroide viene eseguita correttamente solo se le macchie generate dai fotoni non si sovrappongono tra loro. Una bassa densità locale di fotoni accumulati durante ogni singola esposizione del CCD al flusso incidente implica una lettura molto più frequente del detector nella modalità a conteggio di singolo fotone, rispetto alla modalità tradizionale. Un test veloce eseguito a ESRF per valutare il tempo di esposizione in condizioni sperimentali tipiche indica che può essere necessario un tempo di esposizione minore di 40 secondi. Il tempo di lettura del CCD è attorno a questo stesso valore se tutta la superficie del detector è utilizzata per acquisire immagini nella modalità di lettura a basso rumore/bassa velocità, ma può essere ridotto a meno di 10 secondi selezionando una regione minore del sensore. Comunque, questa necessità di acquisire molte immagini con brevi tempi di esposizione per ogni spettro causa una perdita significativa del tempo di ciclo (*duty cycle*) e pertanto una perdita di efficienza, che rappresenta il più importante fattore limitante per l'uso dei metodi di ricostruzione del centroide con detector CCD. Per confronto, nella modalità di acquisizione tradizionale, il tempo di esposizione solitamente utilizzato va da 5 a 15 minuti e l'effetto del tempo di lettura sul tempo di ciclo è praticamente trascurabile.

Essenzialmente, il lavoro presentato in questa tesi è uno studio pionieristico della possibilità di utilizzare le tecniche di ricostruzione del centroide con raggi X soffici.

Simili metodi per il miglioramento della risoluzione sono infatti già ben noti per quanto riguarda fotoni di energie più alte, che producono una nuvola di carica più estesa, sulla quale è più semplice utilizzare gli algoritmi per la ricostruzione del centroide. Con questo lavoro, viene dimostrata la possibilità di raggiungere un importante miglioramento della risoluzione attraverso un'elaborazione via software delle immagini acquisite da un detector CCD tradizionale, di alta qualità, per raggi X soffici. L'utilizzo di un detector tradizionale invece di uno progettato appositamente per questo scopo è di importanza fondamentale per le applicazioni. Oltre al vantaggio del costo decisamente minore del dispositivo, la possibilità di usufruire dello stesso sensore per acquisire immagini da elaborare con l'algoritmo tradizionale o con quello a conteggio di singolo fotone può permettere di passare da una modalità all'altra semplicemente cambiando i parametri di acquisizione del CCD. L'unico, ma importante, prezzo da pagare per l'utilizzo di un detector tradizionale al posto di uno progettato per questo scopo è una perdita di *duty cycle* e pertanto una perdita di efficienza dell'apparato nel complesso: questa è una limitazione importantissima per il RIXS, una tecnica il cui principale problema ad oggi è costituito dalla bassa intensità del segnale. Va comunque detto che esistono dei metodi per ridurre questa perdita di efficienza, con opportune configurazioni dei parametri che influenzano il tempo di lettura del sensore; inoltre, grazie alla crescente velocità di lettura di questi dispositivi, si può ritenere che nel corso dei prossimi anni il problema venga eliminato quasi completamente. Il lavoro sull'ottimizzazione del codice per la ricostruzione del centroide è ancora molto intenso e ci si aspetta che il software possa essere terminato in tempo per essere utilizzato nei primi esperimenti di RIXS a ID32, previsti per gli ultimi mesi del 2014.

Abstract

Resonant Inelastic X-ray Scattering (RIXS) is a synchrotron based spectroscopic technique that in the last 15 years has been growing to become one of the most innovative and powerful tools for the study of the magnetic and electronic structure of solids and molecules. One of the most profitable applications of RIXS is connected to the study of magnetic and electronic properties of transition elements and rare earth compounds. RIXS offers in fact the unique possibility of studying energy- and momentum-resolved neutral elementary excitations, with bulk sensitivity and chemical selectivity.

Among others, one of the most original recent applications of RIXS has been the discovery of charge density modulations in high T_c superconducting cuprates, in particular underdoped YBCO. In this thesis I will present some recent results showing the presence of charge density waves (CDW) also in optimally doped Bi2212. This very important discovery can help to shade light on the nature of these charge orderings and of the pseudogap phase. The detection of this ordering was possible thanks to the momentum and energy resolution of RIXS, that allowed the study of a very small modulation of the elastic peak, by separating the elastic signal from the rest of the spectrum.

Being this technique so promising, in the last years the synchrotron facilities have designed and built several dedicated instruments, with increasing energy resolution and sample position control. Among these, the group of Politecnico di Milano lead by Prof. Giacomo Ghiringhelli and Prof. Lucio Braicovich has been contributing to the design and construction of a new high resolution RIXS spectrometer for soft x-rays, called ERIXS, that will be mounted on the new ID32 beamline at ESRF. The group has a well established experience in the field, having designed the spectrometers AXES,

mounted at ID08 beamline at ESRF and SAXES, mounted at ADRESS beamline at SLS. Both these spectrometers have had a crucial influence on the success of RIXS, having provided almost all the important RIXS results of the last 10 years in the soft x-ray range.

The ERIXS spectrometer at ID32 has been designed to improve the energy resolution by 5 times with respect to AXES at ID08, while increasing the overall count rate by a factor of 3. These are unprecedented performances that can be achieved only through an extreme optimization of all the components of the beam line and of the spectrometer. There comes the work described in this thesis, which deals with an innovative utilization of the CCD detector already in use on AXES. In this spectroscopy, the energy of scattered photons is determined by dispersing them with a diffraction grating and imaging their intensity distribution vs diffraction angle using a position sensitive detector. One of the crucial limiting factors is then the spatial resolution of the detector.

The most used image sensors for x-rays applications, thanks to their high efficiency, low noise and versatility, are the charge coupled device (CCD) detectors. In these commercially available devices, the spatial resolution has been reported at $\sim$ 25 μm FWHMindependently of the pixel size, for soft x-rays. When a photon is absorbed in the active layer at the surface of the detector a large number of electorn-hole pairs are generated, and an electron cloud diffuses in the material before being captured by the potential wells of physical pixels fabricated in the wafer. Depending on the pixel size the charge cloud is spread over several neighboring pixels, thus reducing the spatial resolution of the detector. On the other hand, these spots can allow the use of centroiding techniques to determine the exact position of impact of photons, achieving a resolution which is better than the pixel size.

This thesis describes the development and test of an algorithm that allows a significative enhancement in the detector resolution, using a single photon centroid reconstruction. The determination of the photon impact position is based on the calculation of the center of mass (COM) of a group of pixels containing the spot, i.e. it is performed an average of the pixels' positions using as weight the signal accumulated inside each pixel. In order to evaluate the actual performances of our code (effective spatial resolution, speed and limitations due to overlapping events), a resolution test

was carried out in the labs of Politecnico di Milano, using a traditional x-ray source. The experimental set-up allows a very direct measurement of the resolution, by analysing the sharpness of the shadow of a razor blade edge on acquired images. The detector used for these tests is a CCD of Princeton Instrument (PI-SX 1300, 20 μm pixel size), used at ESRF until some years ago for soft x-rays detection. In addition to the experimental test the software was used also on "virtual" images obtained by Monte Carlo generation of photon impact and of the relative charge cloud. In this way the ultimate performances of the code could be tested under controlled conditions and the effect of pixel size, cloud dimensions and readout noise on the final result could be simulated. The resolution achieved is excellent in both the tests, being around 7 μm on experimental data and 2 μm in the ideal case of simulations. The experimental value is excellent because it would fulfill the target of 10 μm resolution required for the optimal performances of ERIXS. The theoretical limit of 2 μm, although obtained by neglecting the effects of read-out noise, demonstrate that a large margin of improvement is available for the future. The discrepancy between simulations and measurements can be attributed, at least partly, to geometrical limitations in the optical system used for the tests.

Despite the encouraging results on resolution, some artifacts were observed on the images after the elaboration, due to possible errors related to the COM calculation. These can occur when some pixels of a spot are not considered for the reconstruction of a spot, or if their signal is overwhelmed by noise. Several methods to overcome these artifacts are under study while writing this thesis and they bode well for the elimination of the problem.

Another problem related to the use of the software for synchrotron spectroscopies arises from the requirement of a low photon density on the images to be analyses with the developed software. As a matter of fact, the centroid reconstruction can work only if the spots generated by the photons do not overlap each other. A low local density of photons accumulated during each single exposure of the CCD to the incoming beam implies a much more frequent reading of the CCD in the single photon detection mode than in the traditional one. A quick test performed at ESRF to evaluate the exposure time under typical experimental conditions indicates that an exposure time lower than 40 seconds is necessary. The readout time of the CCD is around this same value if the

whole detector area is used in the low noise / low speed read-out mode to acquire the image, but can be reduced to less than 10 seconds by selecting only a smaller region. However, this need of acquiring many images with short exposure time for every spectrum causes a significative loss in duty cycle and therefore a loss in efficiency, which is the most important limiting factor to the use of the centroid reconstruction methods on CCD detectors.

Ultimately, the work presented in this thesis is a trailblazing study of the possibility of the single photon counting centroid reconstruction in the soft x-rays range. As a matter of fact, these resolution enhancement methods are already well established for photons of higher energy, which produce a bigger charge cloud that simplify the use of centroid reconstruction algorithms. Here, it is demonstrated the possibility of achieving an important resolution enhancement through a software elaboration of images acquired by an high quality traditional CCD detector for soft x-rays. The possibility to use a traditional detector instead of one specifically designed for this application is of fundamental importance. Apart from the lower cost of the device, the possibility to use a single detector to acquire images to be elaborated with the traditional or with the single photon counting algorithm can allow to shift between the two methods just by changing the CCD acquisition parameters. The only but important price to pay for using a traditional CCD detector instead of those designed for this purpose is a loss of duty cycle and thus a loss of overall efficiency of the RIXS apparatus: this is a crucial limitation for a technique hampered until now mainly by the counting rate. Anyway this problem can be reduced by modifying the parameters that influence the readout time and it will be probably further canceled during next years thanks to the increasing reading speed of these devices. The software is expected to be ready to be used for the application in synchrotron spectroscopies by the first RIXS experiment of ID32, foreseen for the last months of 2014.

Chapter 1

RIXS Spectroscopy and Instrumentation

1.1 RIXS spectroscopy

Resonant Inelastic X-ray Scattering (RIXS) is a very powerful spectroscopic technique used to probe excitations [1] [2] in a wide range of materials as transition metal compounds [3] [4] or rare-earth systems [5], semiconductors and insulators [6], oxides [7] and materials of current interest such as high temperature superconductors [8] or catalysts [9]. Although the principle of RIXS has been known for at least 30 years, [10], its application has become viable and increasingly popular only in the past decade [5], thanks to the development of dedicated instrumentation and third generation synchrotron radiation facilities, which allowed a stunning improvement of photon flux and energy resolution.

In this introductive Section the scattering process is described and the excitations probed by this process are classified and briefly introduced, showing the capabilities of RIXS useful for the study of magnetic and electronic properties in solids. In particular it will be often made reference to the case of superconductive cuprates, which are the materials currently most studied by our group. An unconventional application of RIXS spectroscopy on superconductive cuprates will be shown in Chapter 2.

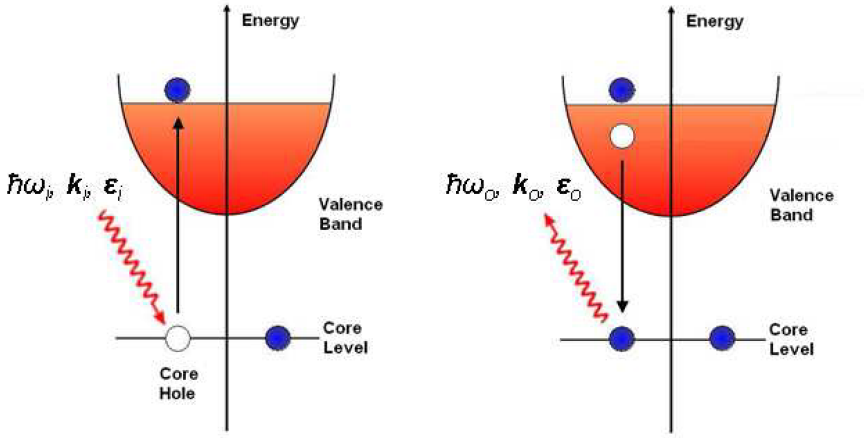

Figure 1.1: Scheme of the RIXS process: the incoming photon $\hbar\omega_i$ is absorbed and a core electron is promoted to an empty state above the Fermi level, creating an hole (left panel). Afterwards the system deexcites thanks to the recombination between the core hole and a valence electron and a photon of energy $\hbar\omega_o$ is emitted (right panel).

RIXS technique

RIXS is based upon a second order process that involves two steps, as shown in Figure 1.1. An incoming x-ray photon of energy $\hbar\omega_i$ hits the sample and excites a core electron, which is promoted to an empty state above the Fermi level. A core hole is thus created and the system is highly excited in a very unstable intermediate state, with a lifetime of ~ 1 fs. After this time the system decays into a final state emitting another x-ray photon of energy $\hbar\omega_o$ generated by the recombination of the core hole with a valence electron.

If $\hbar\omega_o = \hbar\omega_i$ no energy is transferred to the sample at the end of the process and thus an elastic scattering occurs, with no excitation of the system in its final state. Otherwise, it can also happen that $\hbar\omega_o < \hbar\omega_i$ and this leads to an excitation of the system of energy $\hbar\omega_i - \hbar\omega_o$. A RIXS spectrum is the plot of the number of emitted photons versus the "photon energy loss" $\hbar\omega_i - \hbar\omega_o$ and allows the study of the elementary excitations in the sample.

The described process has several characteristics that make RIXS an unique technique for the study of low energy excitations in condensed matter physics. First of all, being RIXS a *photon in-photon out* technique, no charge is added or removed in the scattering process, at variance to photoelectron spectroscopy, another technique broadly used for the study of electronic structure of solids and molecules. Therefore, the overall *neutrality*

of the system is preserved and this is fundamental to avoid possible unwanted changes in the total charge of the system. If that were not the case, added or removed charge would introduce a modification of energy levels and thus a further change in the energy of the outgoing photon, not related to the elementary excitation under study, should be considered.

Another feature of RIXS strictly related to the use of x-rays is the *bulk sensitivity*. For soft x-rays the penetration depth of photons is of some tens of nm and thus the incoming and outgoing photons can pass through several atomic layers, penetrating into the sample and probing the bulk of the material.

Bulk sensitivity does not mean that only thick and massive samples can be used, as it is (in an extreme case) for neutron spectroscopies. This is due to *element (or chemical) selectivity*, achieved thanks to the resonance with an absorption edge of a specific element. An absorption edge is a sharp increase in the x-ray absorption spectrum that occurs at photon energies that correspond to an electronic transition from a core level to the Fermi level. At these energies, the interaction of photons with the specific atoms reaches a maximum and therefore the resonance allows to excite selectively an element and study elementary excitations while "sitting" on that specific element. Since the chemical environment influences the shape and energy of the absorption edge, different oxidation states and coordination symmetries can be discriminated. When the incoming beam is tuned to an absorption edge of a specific element in the sample, the contribution to the spectrum due to other chemical elements becomes negligible and this allows to study buried interfaces, multilayers, capped samples and thin films covered by other materials. Moreover, the surface sensitivity can be also enhanced if necessary by working in grazing incidence conditions, because the depth of the sample probed by photons decreases with the sine of the angle of incidence.

Kramers-Heisenberg cross section

The theoretical description of second order processes provides a formula for the RIXS cross-section [11], that express the intensity of the radiation emitted by the sample as a function of the incoming and emitted photon energies. This dependence is expressed by

the Kramers-Heisenberg formula:

$$I(\hbar\omega_{in}, \hbar\omega_{out}) \propto \sum_f \left| \sum_i \frac{\langle f| T^e |i\rangle \langle i| T^a |g\rangle}{E_g + \hbar\omega_{in} - E_i + i\Gamma_i/2} \right|^2 \cdot \delta((E_g + \hbar\omega_{in}) - (E_f + \hbar\omega_{out})) \tag{1.1}$$

where g,i and f indicate the ground (initial), intermediate and final states respectively, and $\langle f| T^e |i\rangle$ and $\langle i| T^a |g\rangle$ are the matrix elements of radiative transitions relative to the absorbed and emitted photons. In the region of soft x-rays, which is the one of interest for this thesis, $\overrightarrow{k} \cdot \overrightarrow{r} \approx 2\pi r/\lambda \ll 1$ with $r \sim 1$ Åand so T^a and T^e can be approximated by dipole operators, neglecting the electric possibility of quadrupole transitions. However, thanks to the presence of two different and consecutive dipole transitions, excitations forbidden by the dipole selection rules can be achieved, as those within a d valence cell in transition metals compounds.

The two matrix element product is divided by a factor which becomes very small in the case of resonance, increasing in this way the process cross section. It is interesting to note that the presence of the imaginary term $i\Gamma_n$, due to the finite linewidth of each intermediate state $\langle i|$, forbids a division by zero. The δ-function assures the respect of the law of conservation of energy, stating that the difference in photon energies equals the excitation energy of the system.

Finally, two sums over the intermediate and final states are present, because in a generic RIXS process there could be several degenerated states. In particular, the intermediate states, which are not observed directly, need to be summed coherently, taking into account the relative phases before being squared. On the other hand, final states are actually observed, and thus the sum is incoherent and does not generate interference effects.

RIXS for the study of elementary excitations

The excitations probed by RIXS are related to the charge, spin, and orbital degrees of freedom of the studied system, and also to its lattice dynamics.

In order to fully characterize the excitations resulting from the scattering process one has to consider the conservation laws for energy and momentum of the whole system, including both photon and scatterer, before and after the scattering process. Given that

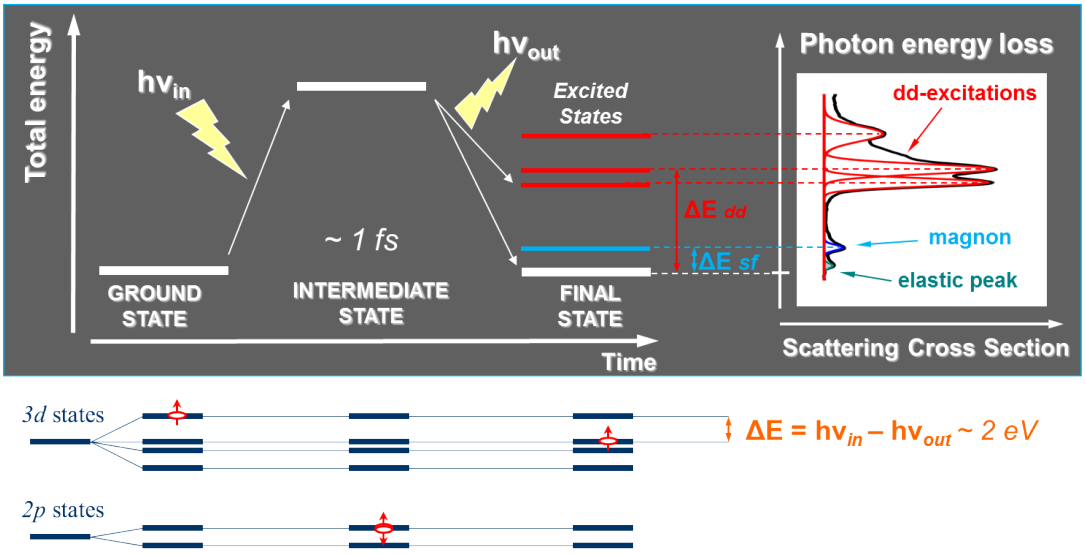

Figure 1.2: Energy scheme of the three stages of a Cu L_3 RIXS process and a typical RIXS spectrum of a cuprate.

the system lies in the ground state before the interaction with x-rays, one can obtain the energy and the momentum of the resulting excitation occurred in the sample by imposing that:

$$\begin{aligned} \hbar\omega_i &= \hbar\omega_o + E^{exc} \\ \hbar\vec{k}_i &= \hbar\vec{k}_o + \hbar\vec{q}^{exc} \end{aligned} \tag{1.2}$$

where $\hbar\omega_i$ ($\hbar\omega_o$) is the energy of the ingoin (outgoing) photon and $\hbar\vec{k}_i$ ($\hbar\vec{k}_o$) is the corresponding momentum. A third conservation law applies to the angular momentum of the whole system and the polarization state of the ingoing (ϵ_i) and outgoing (ϵ_o) photons.

In experiments, the parameters describing the ingoing photons are imposed, while the outgoing photon characteristics are measured. The spectrometer allows to determine the photon energy (thanks to the dispersion by the grating) and the momentum (thanks to the geometry), while the polarization is usually not measured.

Excitations accessible in cuprates at Cu L_3 edge

Figure 1.2 shows the steps of a RIXS process performed at Cu L_3 edge. As depicted in figure, in layered cuprates the Cu d states are split by the symmetry

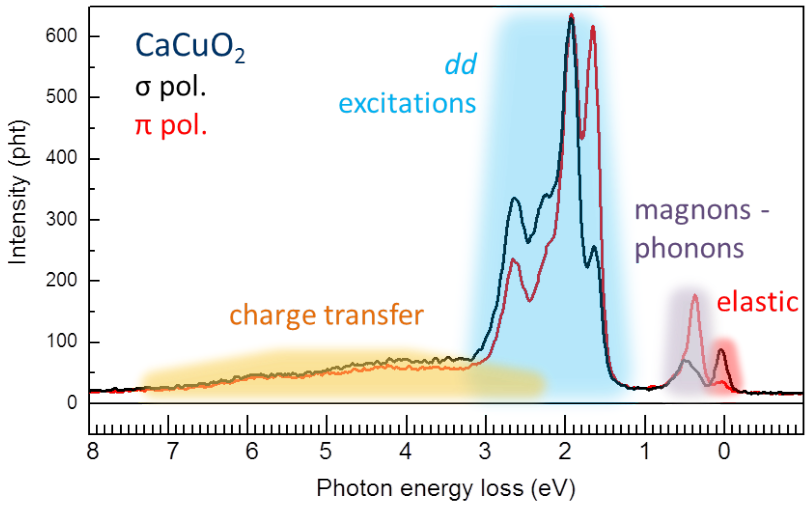

Figure 1.3: RIXS spectrum of $CaCuO_2$, with vertical (black) and horizontal (red) polarizations of the incident beam. All the spectral features are highlighted with colors. Red: elastic peak (usually very small); purple: low energy excitations (magnetic excitations and phonons); blue: *dd* excitations; orange: charge transfer.

breaking due to the presence of ligand atoms between CuO_2 layers. Moreover, copper ions in the CuO_2 layers of cuprates are usually in a $3d^9$ configuration and this makes the description of the process easier to be illustrated in terms of the unique hole.

The process starts when an x-ray photon is absorbed and excites the hole from the valence d states to the core $2p_{3/2}$ level. After a short time ($\sim 1\ fs$) the system decays by emitting another photon and the hole moves back to the d states. If the final d state occupied by the hole is the same of the initial one the process is elastic and this leads to a peak to zero energy loss in spectrum. Otherwise, it can happen that a different d state is occupied at the end of the process and this leads to the so called *dd* excitations, which are found at about 2 eV of energy loss in the spectrum. In principle this is a transition not allowed by dipole (since $\Delta l = 0$), however with two dipole-allowed transitions having $\Delta l = -1$ (d-to-p) and $\Delta l = +1$ (p-to-d) it becomes possible. These *dd* excitations provide the strongest contribution to the RIXS spectrum of cuprates (and thus the highest peaks), but several other excitations of different nature are present and need to be recognized for a thorough interpretation.

The most studied are the magnetic ones, because of their possible connection with the

superconductive properties of cuprates. An antiferromagnetic order is present in CuO_2 planes in their ground state and a magnon is a wave-like collective excitation of the spin lattice, that could arise thanks to the strong spin-orbit interaction in the $2p$ core hole present in the intermediate state. Magnons are quasi-particles of about 100 meV energy and thus the corresponding peak is found on the RIXS spectrum right after the elastic peak.
Other possible excitations accessible by the RIXS spectroscopy are charge transfer excitations, i.e. an electron transfer from a copper ion to its ligands, and phonons, which are collective lattice excitations. Both these excitations are found at energies approximatively similar to those of a magnon. A typical RIXS spectrum of a cuprate material is depicted in Figure 1.3, where the different possible excitations are highlighted.

1.2 Instrumentation for sof x-rays at ESRF: AXES at ID08

RIXS spectroscopy, involving a second order process, is extremely *photon-hungry* and requires the peculiar properties of third generation synchrotron light, together with a dedicated instrumentation. This Section is an introduction to synchrotron radiation characteristics and instrumentations. The European Synchrotron Radiation Facility features will be briefly discussed and then the layout of ID08 beamline will be presented. This beamline houses AXES (which stands for Advanced X-ray Emission Spectrometer), a RIXS spectrometer used for the experiments presented in next chapter, whose characteristics will be briefly described. This spectrometer has been a leading instrument in the field of soft x-ray emission spectroscopy since 1994, when it was designed and then built in Milan by the group led by prof. L. Braicovich. In 2006 an evolution of AXES, called SAXES was built and installed at the beam line ADRESS of the Swiss Light Source(SLS) in Villigen. During the next year, AXES will be substituted by ERIXS that will work at ESRF in the new ID32 beamline dedicated to high resolution resonant inelastic soft x-ray spectroscopy, that is currently being build and that will allow important improvements in terms of resolution and photon flux. The high resolution that is expected to be achieved with this new instrumentation will be probably limited by the detector characteristics. and this is the

main reason that pushed to the development of a single photon counting algorithm, in order to allow a detector resolution enhancement. This software constitutes the main topic of this thesis and it will be discussed in Chapter 4.

Introduction to synchrotron radiation and ESRF

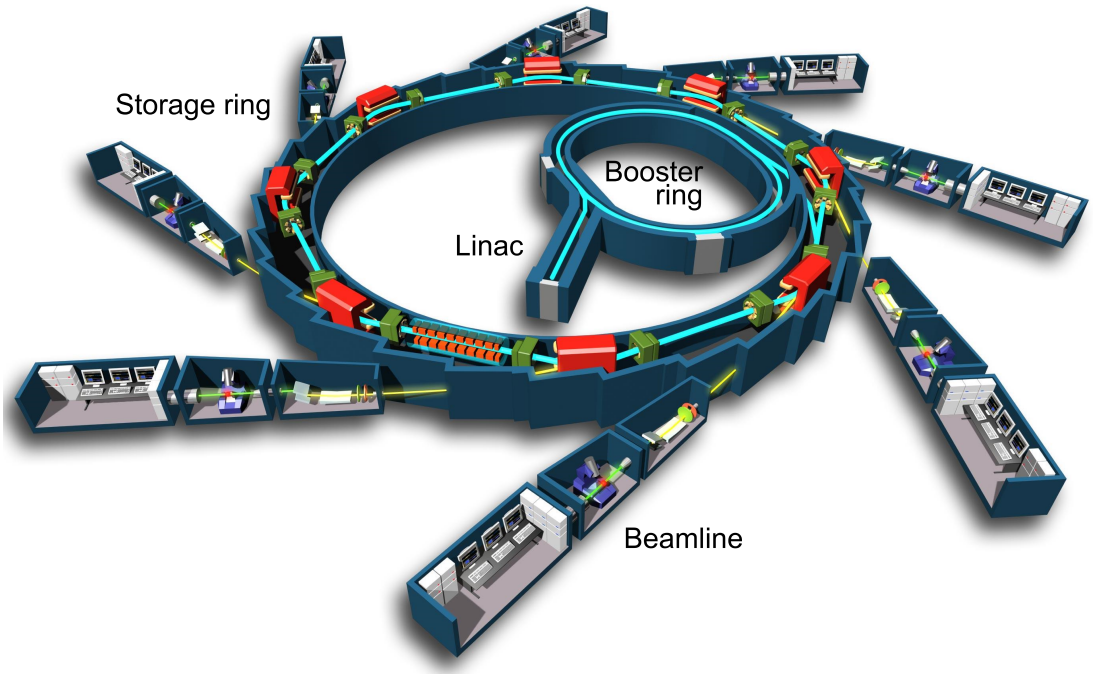

Figure 1.4: Typical schematic picture of a modern storage ring [12].

A synchrotron radiation source provides high collimated and intense light beams in a continuum spectral range from infrared up to hard x-rays. The structure of a typical third generation radiation facility is sketched in Figure 1.6 . Electrons are produced by an electron gun and accelerated by a linear accelerator, named *linac*, which is located inside the actual storage ring. The electrons are then inserted in the booster ring, where they are further accelerated via magnetic force. The magnetic fields need to be simultaneously increased with the gain of the electron beam energy, due to the increment of the relativistic mass, and this is the reason for the name "synchrotron". In the last step the electrons enter in the storage ring, where they keep circulating at relativistic velocity emitting the radiation used by the several beamlines connected to it.

The curved trajectory is imposed to the electrons using magnetic field forces. Bending

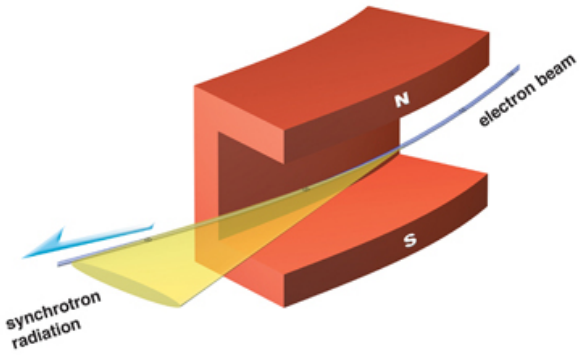

Figure 1.5: Schematic picture of radiation emission from a bending magnet.

magnets or dipole magnets are used to curve the beam and thus to produce radiation tangential to the electrons orbit. The second generation synchrotrons used these bending magnets to provide the x-ray photons to beamlines, which are the laboratories connected to the storage ring. The emitted radiation, due to relativistic effects, is directed tangential to the electron motion and has a very small divergence along vertical direction, being confined within a small angle (usually less than 1 mrad) defined as $\theta \sim \frac{1}{\gamma}$ where γ is the Lorentz factor. Along the horizontal axis the beam divergence is bigger, being defined by the angle between vectors tangential to the electron trajectory before and after passing inside the magnet [13] [14] [15]. Between two bending magnets, several quadrupole and sestupole magnets are used to focus the beam and correct the chromatic aberrations. These aberrations are due to errors in the focusing of the electrons characterized by a slightly different energy than the desired one.

In order to avoid perturbations of the electrons trajectory inside the ring, the entire machine is kept in ultra high vacuum ($10^{-}9$ to $10^{-}11$ mbar). A radio frequency (RF) system in the storage ring is used to supply electrons with the energy they lose (in the form of radiation) as a consequence of their centripetal acceleration.

Third generation machines differ from previous ones for the presence of insertion devices between bending magnets, that allow the production of radiation with higher brilliance, directionality and monochromaticity. Insertion devices consist of a periodic structure of magnetic dipoles, placed at specific distances, that produce a magnetic field that varies sinusoidally along the device's axis. Electrons passing through such a field undergo sinusoidal motion in the horizontal plane and this causes the emission of

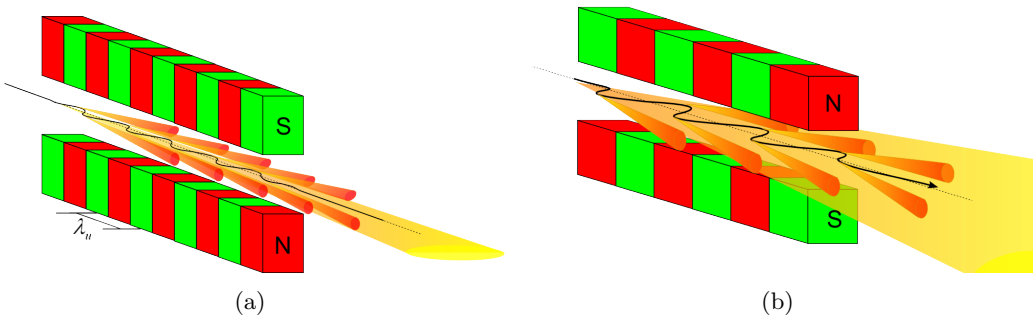

Figure 1.6: Schematic picture of radiation emission from an undulator (a) and a wiggler (b) insertion devices.

photons. There are two kind of insertion devices. In *wigglers* electron trajectory oscillations have angular deviation higher than $\frac{1}{\gamma}$ and this leads to negligible interference effect between light beams emitted along the device, resulting in an emission of radiation similar to the one of a bending magnet, but with higher brilliance and intensity. On the other hand, *undulators* are characterized by an electron trajectory confined within the angular aperture of the emitted radiation. This causes the radiation emitted in different points of the device to be coherent and interference effects become relevant. Resulting radiation spectrum is constituted by a series of discrete peaks of high intensity, whose energy can be modified by varying the magnetic field intensity. The radiation emitted by one of these devices is typically in the horizontal plane.

ESRF has a storage ring of 844 meters circumference that serves 41 beamlines placed tangentially to it. The electron beam, of 6 GeV energy, is guided by 64 bending magnets and is focused by 320 quadrupoles and 224 sextupoles. All storage ring components are arranged in 16 superimposed cells with the same magnet distribution. The current in the ring can reach 200 mA and has an average life up to 100 hours. In order to guarantee a constant and high flux of photons, every 12 hours the ring is refilled with new electrons. The number of bunches can vary between 1 and 992, depending on the operating mode.

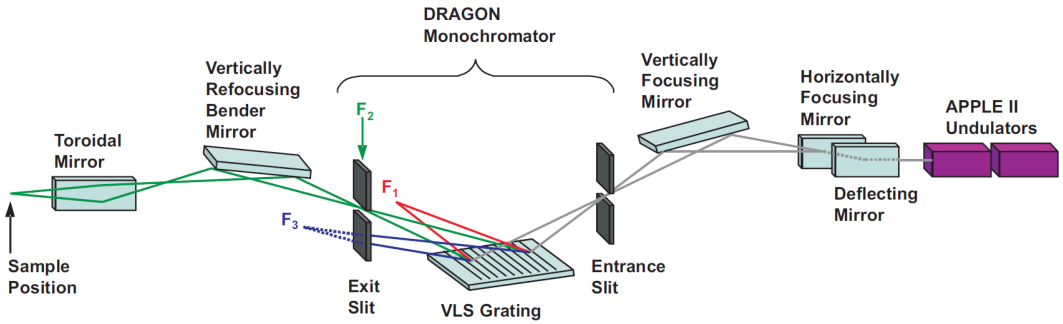

Figure 1.7: Sketch of the optical layout of the ID08 beam line of ESRF. Note how the Dragon monochromator disperses and focuses different energies at different positions, i.e. F1, F2 and F3, imposing the use of a movable exit slit and, as a consequence, of a bendable mirror (bender) in the refocusing system, in order to allow a wide range of working energies [16].

Beamline ID08 at ESRF

ID08 is an intense source of polarized soft x-rays with an high brilliance that is principally used to probe magnetism in a diverse range of systems with x-ray magneto-optical techniques and to study the electronic structure of materials using x-ray and photoelectron emission techniques. The photon energy is tuneable in the range $0.3 - 1.6$ keV making it ideal for studying the magnetic and electronic properties of transition metals and rare earths; in particular the most interesting energies in this range corresponds to the K edges of O and N, the $L_{2,3}$ edges of $3d$ transition-elements compounds and the $M_{4,5}$ edges of rare earth compounds. The principal techniques available at ID08 are x-ray absorption spectroscopy (XAS) and x-ray magnetic circular dichroism (XMCD), spin polarized and angle resolved x-ray photoelectron spectroscopy (SPXPS and ARXPS, respectively), soft x-ray resonant magnetic scattering (SXRMS) and finally x-ray emission spectroscopy (XES). The possibility of studying x-rays emission allows in particular RIXS experiments, such as those described in this thesis.
A sketch of the optical layout of ID08 beamline is displayed in Figure 1.7. The source of the beam is constituted by two APPLE II undulators [17] (Figure 1.8) that provide 100% controllable polarization, both linear and circular, of the emitted radiation, thanks to 4 moveable permanent magnet arrays. X-rays enter in the beamline by the primary slit, placed at 27 meters from the source, that reduces beam size to $2.5 \times 2mm^2$ and its divergence to $40\mu rad$. Along beam path three mirrors are placed, which perform a focusing and a first filtering of the beam. The deflecting mirror is flat

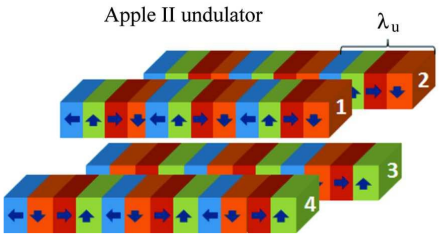

Figure 1.8: Schematic view of an APPLE II undulator for the generation of arbitrarily polarized radiation. By changing relative positions of the 4 series of magnets any kind of helical electron motion (with concomitant emission of elliptically polarized radiation) can be obtained.

and deflects the beam in the horizontal direction of 4° and removes from it photons with energy higher than 1600 eV, for which the mirror reflectivity is very low. The horizontally focusing mirror compensates the deflection due to the previous mirror and focuses the beam on the monochromator exit slits, while the vertically focusing mirror focuses the beam along the other direction on the monochromator entrance slit.

The so called Dragon monochromator is composed by an entrance slit, a single dispersive optical element (grating) and an exit slit. The entrance slit defines the position and the size of the source seen by the grating, which disperses photons with different energies along the vertical direction, as represented in Figure 1.7. The distance between the granting and the entrance slit is fixed, as well as the incident angle of the beam. Several different gratings can be used, depending on the working energy of the experiment, but the most used configuration involves a spherically shaped grating with a radius of curvature of 57.3 m and a groove density of 1200 lines/mm. After the grating, the exit slit selects the energy beam range by spatially filtering the desired photons. Therefore slit aperture defines the energy resolution of the beamline and must be chosen as a trade-off between resolution and photon flux. Since the exit arm changes with the energy of the photons to be selected, as can be seen in Figure 1.7, the exit slit position has to be changed accordingly in order to match the focusing distance for a given photon energy. At the L_3 edge of Cu (∼930 eV), the energy resolution $\Delta E/E$ of the Dragon monochromator is about 2×10^{-4}, with apertures of the entrance and exit slits of 10 μm.

To carry out a RIXS experiment a further refocusing of the x-ray beam on the sample

is necessary, because the light spot on the sample is the source of AXES spectrometer and its spatial extension influences the energy resolution of the measurements. Therefore a refocusing system based on a bendable spherical mirror and a toroidal mirror is placed after the monochromator. The horizontal spot size on the sample is around ~ 50 μm, while the vertical one can reach ~ 5 μm FWHM.
The whole beamline is kept in ultra high vacuum conditions (UHV, 10^{-10} mbar) by ionic pumps. High vacuum (10^{-6} mbar) is necessary due to soft x-rays, that otherwise would be absorbed from air molecules. In addition to this, the requirement of UHV comes from the need to protect the beamline optical elements which otherwise could be damaged by the interaction with high energy photons and carbon atoms present in air.

AXES spectrometer

After the described path, the beam hits the sample, and, for a RIXS experiment, photons emitted by the sample are analysed by a spectrometer. AXES, which stands for Advanced X-ray Emission Spectrometer, is the spectrometer mounted in ID08 since 1995, entirely designed and built in Milan by group leaded by prof. L. Braicovich and prof. G. Ghiringhelli. Figure 1.9 shows the scheme of how the spectrometer works: part of the radiation emitted by the sample enters the spectrometer through an input slit and hits at grazing incidence a concave diffraction grating, that spatially separates different energy components of the beam and focus them onto a CCD detector. The entrance and the exit arms are long 0.6 and 1.6 m respectively, for a total length of the instrument of about 2.2 m. The scattering angle, defined as the angle between wave

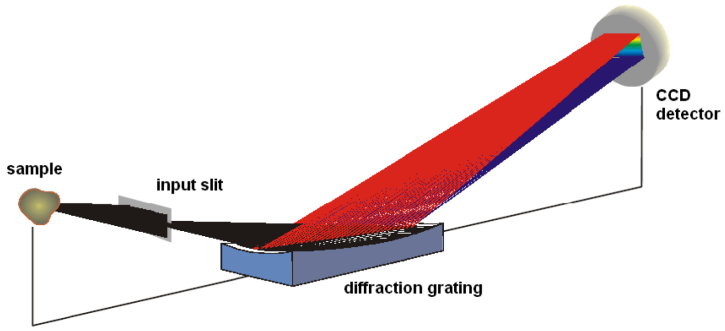

Figure 1.9: Sketch of the optical layout of the AXES spectrometer.

vector $\overrightarrow{k}_{in}$ of incoming photons and wave vector $\overrightarrow{k}_{out}$ of outcoming ones, is fixed at 130°.

The entrance slit, placed at $10mm$ from the sample, was initially used to limit the vertical size of the source of the spectrometer, which is the light spot on the sample, to values from 10 to 50μm. This is useful in order to have a small beam that hits a small portion of the grating, otherwise beams with different energy undergoing different trajectories could hit the CCD surface in the same position, causing a loss in resolution. However, thanks to some upgrades in the beamline, the light spot on the sample is now only $\sim 5\mu$m and so it is possible to work in a slit-less condition, as it is routinely done.

The grating is the only optical element in the spectrometer. This simple scheme was adopted in order to have an easy-to-use instrument and, above all, minimize all high order optical aberration thanks to a variable line spacing. The average groove density is 2400 lines/mm and it varies along the grating and this allows to minimize linewidth broadening. These parallel lines, oriented horizontally and perpendicular to photon direction, disperse radiation along vertical direction, deflecting at higher angles low energy photons, which thus will hit the detector in its upper region, while higher energy photons hit the detector surface in its lower region.

The grating is concave with a fixed radius of curvature, in order to focus all different energy components onto the CCD. The image acquired with the detector is thus constituted by isoenergetic lines that are approximately horizontal and parallel among each other and their relative vertical positions correspond directly to their energy. Therefore the CCD positioning is crucial to select the desired photon energy range and thus the spectral window in study. The CCD surface should also be positioned on the grating focal plane, to avoid energy resolution losses.

Another problem connected with the grating that can cause resolution losses is coma aberration. This effect is proportional to the square of the grating length used to focus the beam. To limit this area some masks could be placed before the grating reducing the lateral size of the illuminated region; this causes a loss in signal intensity and hence a trade off choice between intensity and resolution is again needed.

The spatial resolution of the CCD detector determines the virtual exit slit of the spectrometer. As it will be widely discussed hereinafter, in Chapters 3 and 4, the

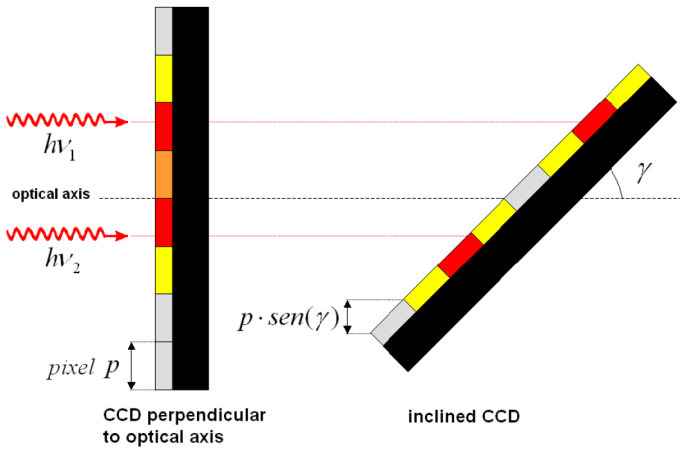

Figure 1.10: Sketch of the improvement in the effective spatial resolution for an inclined CCD. The gain in spatial resolution is equal sen(γ), with γ angle between the detector surface and the optical axis of the spectrometer.

effective spatial resolution of modern CCD detectors is around 25μm, irrespective of the pixel size, as a consequence of spots generated by xray photons hitting the detector, that involves some neighbouring pixels. One simple way to gain in terms of spatial resolution is to use the CCD inclined at a certain angle. As it is depicted in Figure 1.10, two spots due to two photons hitting the CCD at different heights would overlap in case of detector perpendicular to the optical axis. In case of grazing incidence the same photon spots would be spatially separated. In AXES the detector is inclined by a 15° angle, and this reduces spatial resolution to around $6 - 7\mu$m. As a consequence of the inclination the CCD surface is no more on the plane perpendicular to the optical axis on which the image is focused, and a defocusing problem could arise. However, this effect is fully compensated by the gain in spatial resolution.

Samples are usually attached on a copper sample holder with silver paint, double-sided metallic adhesive tape or conductive glue; the holder is then connected to a manipulator. It is necessary to have a conductive system in order to supply electrons to samples which lose charges when hit by x-rays due to photoemission. On the sample holder many samples can be mounted and this is useful to carry out different experiments without the need to open the vacuum chamber. The manipulator allows samples to be moved in the three spatial directions, which is useful in order to put the sample in the crossing between the beamline and spectrometer axis. Moreover, samples

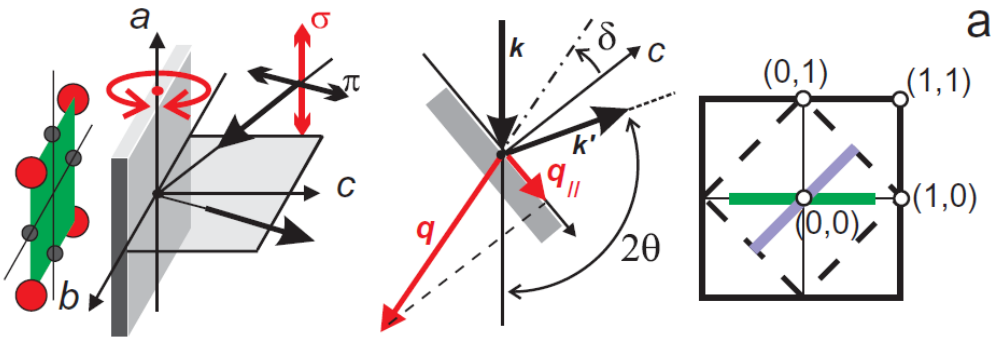

Figure 1.11: Sketch of the typical experimental layout for RIXS measurements on cuprates and 2D Brillouin zone for cuprates.

can rotate around a vertical axis, perpendicular to the scattering plane, allowing to vary the incident angle of the beam on samples and thus the projection on the sample surface of the transferred momentum. The experimental layout of a RIXS measurement on a layered cuprate is shown in Figure 1.12 [18]. The incoming beam hits the sample surface (parallel to the ab plane) at incident angle θ_i and outgoing beam is collected at the angle θ_o. The scattering angle 2θ is fixed at 130°, whereas the incident angle can be changed, thanks to the rotation of the sample holder. Together they define δ, the angle between the sample c-axis and the transferred momentum $\vec{q}$ (red arrow). Althought the scattering angle and the photon momentum are fixed, by changing δ $\vec{q}_{\parallel}$ can be modified, allowing to measure dispersing feature along a chosen direction of the 2D Brillouine zone of bidimensional samples. The direction is chosen when samples are mounted by orienting the a and b axes with respect to the scattering plane.

The resolving power of a spectrometer such as the one described above depends on different experimental parameters. First of all the finite source size brings to a spatial uncertainty on the beam path into the monochromator, contributes to the energy resolution of final spectrum. Another contribution to combined resolution is given by the already discussed spatial resolution of the detector. However this is enhanced by using it at grazing incident and its contribution is thus negligible for AXES because smaller than other ones. Of course the last and most important element that influences the spectrometer resolution is the grating, with aberrations introduced by approximations in the shape and by errors in the actual realization of the optical element (as slope error). Coma aberrations are controlled with a mask that can be

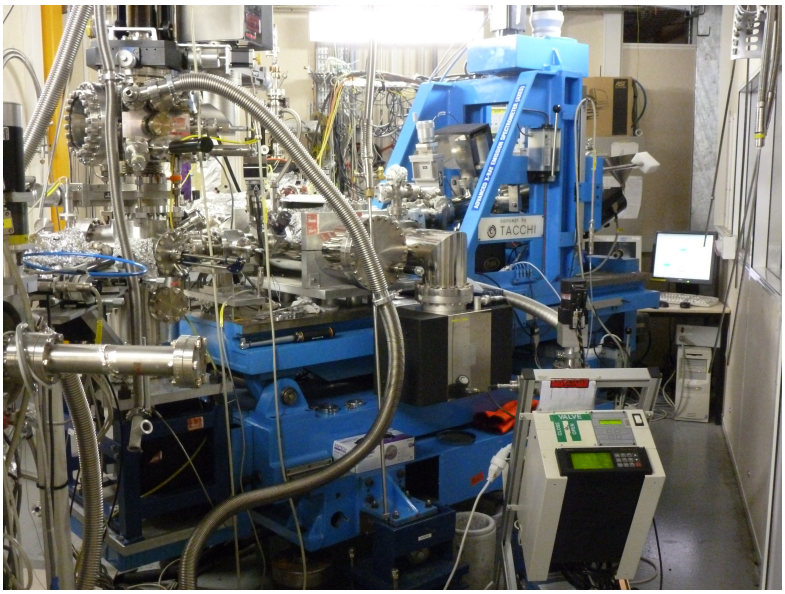

Figure 1.12: Picture of the AXES spectrometer.

used to control the length of the *footprint* on the grating surface.

To consider the total resolution limit of the system for a RIXS experiment one has to consider also the contribution coming from the beamline, i.e. the linewidth of the monochromator. The actual combined resolving power of beamline and spectrometer is in fact given by the quadratic sum of all the listed contributions. The resolving power of AXES is comparable to that of the Dragon monochromator (at 930 eV) and this results in a combined energy resolution of ~ 235 meV (measured as the FWHM of the elastic peak of polycrystalline graphite) at the Cu L_3 edge, i.e. a resolving power $\Delta E/E = 2.5 \times 10^{-4}$.

The new ID32 beamline and ERIXS

As part of an upgrade program of ESRF the new soft x-ray beamline ID32 was designed and it is being build while writing this thesis. The beamline will be completed during 2014 and it will substitute ID08, that was closed in the fall of 2013.

The new beamline will have two main permanent instruments: a dichroism end-station (XMCD) and an end-station for very high resolution soft x-ray RIXS. There will also be a third experimental hutch for other soft x-ray experiments.

The high resolution expected by the RIXS branch will be affected by the detector spatial resolution and this is the main reason that led to many studies to enhance the

detectors resolution. One of these studies is the main subject of this thesis and consists in an algorithm, described in Chapter 4, that allows an enhancement of the resolution of the images acquired by the detector, at least in some experimental conditions.

The layout of the new beam line is not described here for brevity and convenience, and only the main performances are listed below. The total length of the beamline is 100 meters, of which 70 m for the monochromator that supply the end hutches with the beam. The photon flux on the sample should be around $2 \cdot 10^{11}$ $photons/sec$ in a bandwith of 20 meV. The resolving power is expected to be $\Delta E/E = 58000$ at 1 keV when the high resolution grating is used, or half of this value in the normal mode.

. The optical design was made by Prof. Giacomo Ghiringhelli, whereas the mechanical design and the full cost of the construction and operations is covered by the ESRF.

Chapter 2

Charge Density Waves in Superconducting Layered Cuprates

This Chapter presents one of the RIXS experiments in which I participated during my thesis period. The aim is primarily to briefly the powerfulness of the RIXS spectroscopy study the properties of strongly correlated materials, without pretending to be complete on the theory and the results.

The experiment described in this Chapter concerns the study of charge density waves in a family of superconducting layered cuprates. The peculiarity of this experiment is that it involves an unconventional use of the RIXS spectroscopy. As a matter of fact the study of the charge density waves, which consist in a modulation of the charge density on CuO_2 planes, should be realized using diffraction, that does not require the acquisition of the whole energy loss spectrum. However, the elastic features that need to be detected are very small compared to the whole integrated inelastic spectrum and thus they are very difficult to detect without a separation of the spectral components, as normal Resonant X-ray Scattering (RXS) does. Therefore RIXS spectroscopy has demonstrated to be useful also to study the order arising in materials, thanks to the increasing angular control of the sample position (and therefore possible $\overrightarrow{q}_{\parallel}$ resolution) of modern spectrometers.

The first Section of the Chapter consists in a short introduction to high-T_c cuprates

superconductors. Then the charge density waves problem is briefly presented together with some experimental results.

2.1 High-T_c superconducting cuprates

Since their discovery in late 1986 cuprates superconductors have attracted a lot of attention due to the many potential technological applications allowed by their high critical temperature. However most part of the large variety of phenomena occurring in these systems has still to be understood and the mechanism behind high-T_c superconductivity (HTS) remains substantially unknown.

The structure of a typical cuprate superconductor is depicted in Figure 2.1. The heart of cuprates is constituted by the CuO_2 planes in which Cu_2^+ ions are in a $3d^9$ electronic configuration, i.e. nine of the ten available d orbitals are filled. The typical structures involve adding along the direction perpendicular to planes one apical oxigen to form a pyramid or two apical oxigens to form an octahedron. The presence of these ligands generates a so-called ligand (or crystal) field that lowers the spherical symmetry of the copper ion and removes the initial degeneracy of the d orbitals. The result is that the nine-electrons configuration has one unpaired electron and one hole in the $d_{x^2-y^2}$ orbital, which points toward the in-plane oxygens. For this reason, and for the sake of simplicity, the electronic states of cuprates are often described by reasoning in terms of the single $3d^9$ hole, as it was done in Section 1.1 to describe the RIXS process in cuprates. The different families of cuprates differ one from the other for the particular composition and structure of the layers between two CuO_2 planes.

In undoped cuprates, the insulating parent compounds of the high T_c superconductors, the Cu_2^+ spin 1/2 ions in the CuO_2 planes are ordered antiferromagnetically via super-exchange interaction, i.e. the exchange mediated by oxygen. When dopant atoms are inserted in the cuprates structure, they take the place of other atoms present in the layers between two CuO_2 planes, changing the total number of valence electrons in the material. These layers are usually named “charge reservoir” or “blocking” layers because they allow to control, through chemistry, the number of electrons in the available electronic states in the CuO_2. Upon doping, the long-range spin order is destroyed and the superconducting phase appears. However magnetic order and in

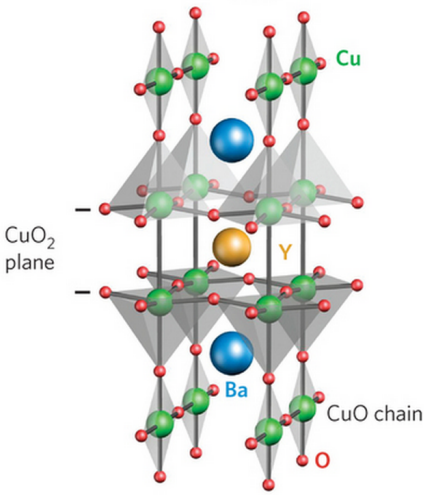

Figure 2.1: The YBCO unit cell.

particular magnetic fluctuations are thought to play an extremely important role for superconductivity, because they are the main candidates to be the "glue" behind the pairing mechanism for high-T_c superconductors instead of phonons.

Fig. 2.2 shows the phase diagram of electron and hole-doped high-T_c superconductors. Upon adding either holes or electrons in the CuO_2 planes, cuprates originally insulating eventually become superconducting and T_c increases to reach a maximum, at a doping defined as optimal, before decreasing at higher doping concentrations, for which the system behaves as a low conductivity metal.

Apart from superconductivity, the phase diagram results very rich and complex. In particular the region of the phase diagram above the superconducting dome is known as the pseudogap phase, since it is characterized by the presence of a pronounced minimum in the density of states near to the Fermi energy. The pseudogap exists above T_c in the underdoped regime, becomes smaller with hole doping, and disappears in the overdoped regime. The pseudogap phase has been under intense study since it exhibits many unusual properties and ordering phenomena; one of these being the arising of charge density waves, discussed in the next Section.

Any successful theory for the description of superconducting cuprates should require a detailed understanding of the whole phase diagram and of all the phenomena arising in cuprates. For this reason it is of paramount importance to study all the dependencies of these features and all the regions of the phase diagram experimentally, in order to

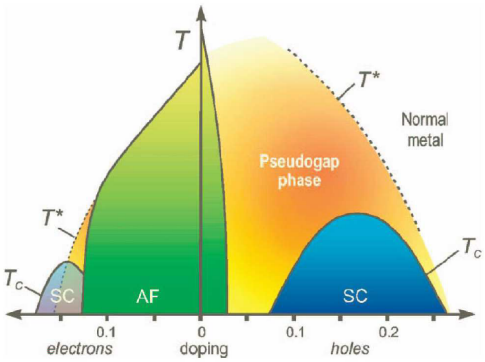

Figure 2.2: Schematic doping phase diagram of electron and hole-doped high- T_c superconductors showing, in particular, the superconducting (SC) and antiferromagnetic (AF) phases. Figure reproduced from Ref. [19].

provide to the theorist complete data for the development of new theories.

2.2 Charge density waves in layered cuprates

A charge density wave (CDW) is a periodic modulation of the electronic charge density that does not occupy fixed positions but can fluctuate relative to the ions lattice. CDWs existence was first predicted in the 1930s by Rudolf Peierls and are now well known to be present in a wide family of quasi-1-D or quasi-2-D layered metallic crystal [20] [21]. In 2012 for the first time, evidence for incipient CDW phases were reported for layered cuprate high-temperature superconductors such as YBCO[22] [23] [24]. It has to be stressed that RIXS gave a decisive contribution to these discovery. [25]

The study of the CDWs in layered cuprates is set in a wider context of research about ordering phenomena taking place in these materials. As a matter of fact, two ordering parameters other than superconductivity have been widely studied: uniform antiferromagnetism in undoped insulating cuprates, mentioned above, and uniaxially modulated antiferromagnetism combined with a static charge order [26] [27] in doped cuprates of the so-called "214" family (which composition is $La_{2-x-y}(Sr,Ba)_x(Nd,Eu)_yCuO_4$). The latter is known as "stripe order", with a charge modulation of period around $4a$, where lattice unit $a = 3.8$ to 3.9 Å is the distance between neighboring Cu atoms in the CuO_2 planes. The discovery of stripes, occurring at a doping around $p = 1/8$ was very important because of their possible link with the

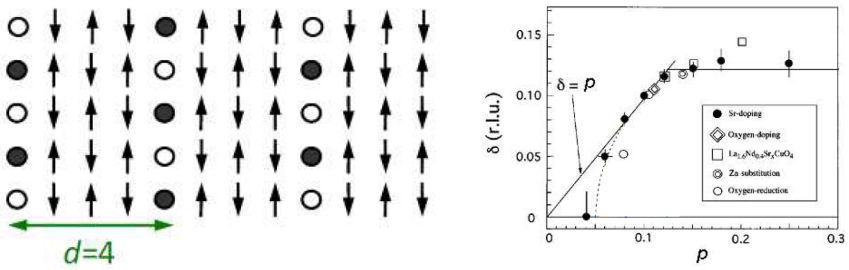

(a) Schematic representation of charge stripes (circles) and magnetic ordering in a "214" cuprate. Filled and empty circles represent two different sites in the charge superlattice.

(b) Doping dependence of the parameter δ of the spin fluctuations from different experiments on 214 cuprates. Reported by [31]

Figure 2.3: Charge stripes in "214" cuprates.

anomalous suppression of superconductivity at this very same doping [26][27][28][29][30][31]. Theorists have worked for long time on the causes of stripe ordering in the "214" systems. The model that better fits the experimental results was developed by J. Lorenzanza and G. Seibold [32][33]. This model predicted an evolution of the density of stripes with doping until they get so close to be separated by 4 lattice parameters. Further doping results in higher filling of the stripes with charge, instead of stripes with shorter period (Figure 2.3(a)). The situation predicted by the theory of the charge ordering with a $d = 4a$ periodicity is depicted in Figure 2.3(a) . It can be seen that there is a spin periodicity that is twice that of the charge modulation.

This spin periodicity was actually detected by diffraction experiments sensitive to spin ordering [28][29][30][31], such as inelastic neutron scattering (INS). As a matter of fact, instead of finding the peak due to bidimensional antiferromagnetic order at $\overrightarrow{q}^{AF} = (\pi, \pi)$, which is typical of the undoped cuprates, peaks were detected at a distance δ from (π, π). These were interpreted as a signature of a uniaxial magnetic order in the CuO_2 planes. This value δ seemed to evolve with doping in an excellent agreement with the theoretical model. The results are summarized in the famous "Yamada plot" [31], reported in Figure 2.3(b).

In the last decade x-ray scattering experiment confirmed these results. Photons are scattered by the charge of electrons and couple to spin only indirectly and thus are sensitive to charge modulation instead of spin ordering. As a consequence, they were found peaks around Γ at a wave vector that is twice that of INS measurements, given

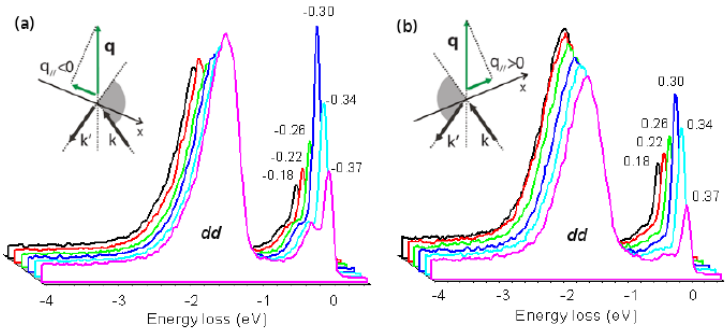

Figure 2.4: Cu L_3 energy-resolved RIXS spectra of underdoped $Nd_1.2Ba_1.8Cu_3O_7$, $T_c = 65$ K,$T = 15$ K, σ polarization for $q_{\|} < 0$ (a) and $q_{\|} > 0$ (b), showing that the quasi-elastic component has a maximum intensity around $q_{\|} = \pm 0.31$ rlu. The effect is less visible for $q_{\|} > 0$ for geometrical reasons (see 2.2).

the above cited factor two in the periodicities of charge and spin. Unfortunately, x-rays can work only in the neighbourhood of the Γ point in the reciprocal space, due to the limited momentum transferred by photons, and neutron can work only around (π, π), because of technical limits in the intensity of signal, and thus there are not comparable data. However, all the evidences were in excellent agreement with the model, which was thus accepted by the research community as a good description for the stripes in the "214" family.

Although the overall phenomenology of stripes in "214" cuprates is quite well known, it must be stressed that a still lasting debate has evolved about the questions of whether this stripe order is a generic feature of the cuprates, and whether stripe fluctuations are essential or counterproductive for superconductivity, and a unified answer is still missing.

In this connection physicists looked for similar evidences in other compounds, and in particular in the "123" cuprates ($RBa_2Cu_3O_{6+x}$ with R = Y or another rare earth element).In this family of cuprates the phase diagram around $p = 1/8$ does not present a suppression of superconductivity, as it is for example in $LaBa_2CuO_4$ of the "214" family, but it is still present a downward deviation of the curve dividing the so-called pseudogap phase to the superconductive one. At this doping level, a (quasi-)elastic peak was detected with an incommensurate periodicity corresponding to $q_{\|} = 0.31$ reciprocal lattice units (see Figure 2.4) [25]. This value is different from the $q_{\|} = 0.25$ rlu found in "214" family and, more important, it is different from what predicted by the above mentioned model. This was an unexpected result, that

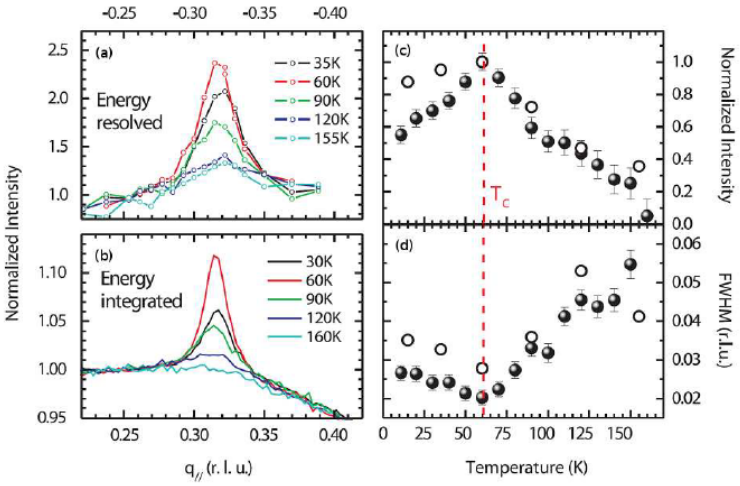

Figure 2.5: (a) and (b) comparison of the measurements of the modulation of the elastic peak obtained by isolating the elastic contribution of an energy resolved spectrum and by the means of a conventional diffractometer for soft x-rays on $YBa_2Cu_3O_{6.6}$. Note that while on the modulation of the amplitude of the elastic peak is around 100% (a), using RXS to measure it the detected effect is just of 10% (b). (c) and (d) T-dependence of the CDW intensity and full width at half maximum (FWHM) derived from the energy resolved (open circles) and the energy-integrated data (solid circles) for σ polarization.

propelled the whole research community to intensify the efforts to throw light on charge orderings in layered cuprates. The nature of the charge ordering in "123" cuprates had to be different from the one of "214" family because many INS experiments results [34][35][36] were in contrast with the possibility of a spin ordering. This, however, did not impose any limitation in principle to the existence of charge ordering. Moreover, further analysis on spectra suggested that the peak at $q_{\|} = 0.31$ rlu was not perfectly elastic, suggesting a possible movement or fluctuation of the charge ordering under analysis.

Therefore, the (quasi-)elastic peak at $q_{\|} = 0.31$ rlu was interpreted as the first direct proof of the presence of CDW in layered cuprates, arising between the pseudogap and the superconductive phase. In particular, CDW were observed in the pseudogap phase, increasing gradually while approaching T_c and decreasing in the superconductive phase. In addition to this, the corresponding peak in the reciprocal space, starting with a FWHM$\sim$ 0.02 rlu, becomes wider decreasing the temperature below T_c (see Figure 2.5 (c) and (d)), and this could indicate a shorter correlation length related to the charge ordering. Therefore, the decreasing in the superconductive region of the phase diagram was considered to be a proof of the competing behaviour between CDW and superconductivity. Moreover, a flatter temperature dependence of CDWs at

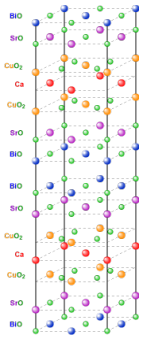

Figure 2.6: BSCCO2212 unit cell.

temperatures below T_c was observed in presence of magnetic fields [37], that seem to stabilize the CDW signal. On the other hand, magnetic fields are known to lower the T_c and thus to be competing with superconductivity. This opposite dependance of CDW and superconductivity versus applied magnetic fields further strengthen the hypothesis of a competition between the two phenomena. However this statement is not yet universally accepted, because of the lack of a complete study of the CDW dependence on temperature and doping in cuprates.

Apart from the relationship between charge modulation and superconductivity, CDW have always been observed in the pseudogap region of the phase diagram, suggesting an intimate connection between the pseudogap and charge ordering phenomena. All the experimental studies mentioned above provide evidences of the presence of distinct electronic symmetries in the pseudogap phase, but the nature of this relationship has not been fully understood yet. As stated before, charge modulations were observed only in underdoped cuprates thus far, around $p = 1/8$ hole doping, i.e. at a doping level lower than the one at which the highest T_c is reached. In the particular presented case of YBCO, the CDW signal was observed to be constant at dopings $0.09 \leq p \leq 0.13$ while out of this range it seemed to disappear, or to be smaller then the experimental uncertainties. However, the pseudogap still exists also in the optimally-doped cuprates (optimally doping is around $p = 0.16$ for YBCO), as it is depicted in Figure 2.2; hence, in order to confirm a connection between the CDWs and the pseudogap, this region of the phase diagram needs to be further investigated. It is therefore clear that a complete mapping of the presence of the CDWs on the phase diagram is of primary importance to understand the physics underlying high-T_c superconductors.

Evidence of charge density waves in optimally doped Bi2212

Experimental

In the above described context the experiment I am going to present intends to proof the presence of CDWs in an unexplored region of the phase diagram of cuprates, that is the one around the optimal doping. The particular compound in study in this Chapter is the bismuth strontium calcium copper oxide, having the general formula $Bi_2Sr_2Ca_{n-1}Cu_nO_{2n+4+x}$, where n can be 1,2,or 3 and x indicates the dopant concentration. Here we used an optimally doped sample ($T_c = 98\ K$) with n=2, usually referred as BSCCO2212 (pronounced "bisko") or Bi2212. Its unit cell is depicted in Figure 2.6. Measurements were performed at three temperatures (20, 50 and 96 K) in order to study the temperature dependance of the CDW peak. The experiment was performed by angle resolved RIXS, focusing on the quasi-elastic signal of the spectra which is sensitive to charge modulation [25]. The RIXS spectroscopy, being sensible to charge, demonstrated to be very useful to observe these charge orderings. Moreover, being based on a very fast elementary process(only 1 fs passes between the excitation and the deexcitation of the core hole), it is useful to observe these phenomena independently from their fluctuations, provided that their wavelength does not change with their movement.

In principle the charge orderings , giving a modulation of the intensity of the elastic peak, could be studied by diffraction techniques as RXS, that is resonant diffraction. Despite this, RXS measurements are energy integrated, while RIXS allows to discriminate between the elastic (or quasi-elastic) signal, coming from charge density fluctuation, and the dominant inelastic contribution. As a consequence, RIXS measurements have a sensitivity on the modulations of the elastic signal which is roughly one order of magnitude higher than that of conventional RXS experiments.

The experiment was performed at the ID08 beamline of the ESRF, using the AXES spectrometer. The incident photon energy was set to 931 eV, at the maximum of the resonant absorption L_3 peak of Cu^{+2} ($2p_{3/2}$-$3d$ transition). The resonance greatly enhances the sensitivity of the scattering signal to the valence electron system, differently from non-resonant x-ray scattering, in which the ordering of the charges could be monitored only indirectly by the associated lattice distortion. The total

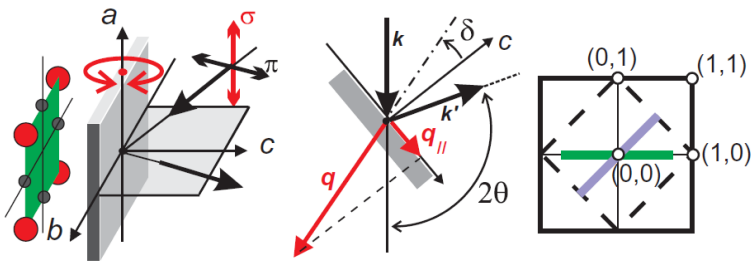

Figure 2.7: Sketch of the typical experimental layout for RIXS measurements on cuprates and 2D Brillouin zone for cuprates. The incident photon polarization can be parallel (π) or perpendicular (σ) to the scattering plane.

combined energy resolution is about ~ 0.26 eV.

The scattering geometry was already presented in Section 1.2, while describing the AXES spectrometer. Figure 2.7 recalls the general scheme for this experiment. The scattering angle is fixed at 130 degrees and the in-plane momentum transfer along the Cu-O bond direction is scanned by rotating the sample (δ in Figure 2.7). The two possible linear polarizations of incoming light are shown, σ being directed along the b direction and always parallel to the sample surface, while π lies in the perpendicular direction. The spectra that will be shown in the next Subsection were acquired using σ polarization for incoming light and with positive $q_{\parallel}$ transferred. This is the most efficient configuration for the study of charge orderings, that involves the study of the elastic peak in the non-spin flip channel. In order to understand this statement it is worth to do some further considerations about the scattering geometry.

In Figure 2.8(a) and (b) the two possibilities of incoming light with σ or π polarization are depicted for positive $q_{\parallel}$, that, in the geometry of AXES, involves an approximatively normal incidence and grazing emission. In the first case, both incoming and outgoing photons have the electric field that lie in the ab plane, leading to a good overlap with the $d_{x^2-y^2}$ orbital. On the contrary, for π polarization, the electric field of the outgoing photon partially points outward the sample surface, having a smaller in-plane component and resulting in a lower overlap with the $d_{x^2-y^2}$ orbital. Therefore the π *in* π *out* channel has a smaller cross section compared to the $\sigma - \sigma$ one. More in general, it can be stated that the emitted beam, at positive $q_{\parallel}$, is dominated by the σ polarization.

As a matter of fact, for the sake of completeness, it has to be stressed that with incoming σ polarization we can obtain both σ and π polarizations of emitted photons

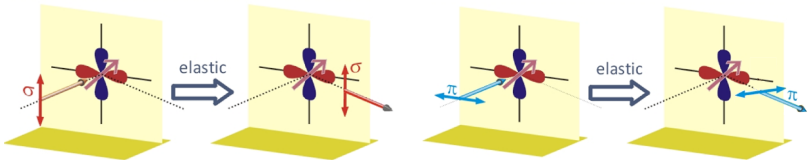

(a) Non-spin flip channel for σ incident polarization and positive $q_{\parallel}$

(b) Non-spin flip channel for π incident polarization and positive $q_{\parallel}$

Figure 2.8: Non spin flip channels for σ and π incident polarization for positive $q_{\parallel}$.

and viceversa. The polarization of incoming and emitted photons can differ because the scattering process could lead, for example, to the excitation of a magnon, which involves a change of the total angular momentum of the sample of ± 1. The conservation of the total angular momentum of the system imposes a change of the spin (and of the polarization) of the photon, resulting in crossed incoming and outgoing polarizations. With incoming σ polarization, the crossed channel is weaker than the other one, because of the smaller cross section that characterizes the π polarized outgoing photons. This is very useful for our purpose, because the scattering from charge ordering does not involve spin flips and thus the π polarized photons would not bring information useful for our experiment.

The situation of negative $q_{\parallel}$ can be imagined as the time-reversal of the presented one, with the incoming beam grazing to the sample surface and the emitted photon normal to it. This configuration leads to a high cross section for σ polarized incoming photons, while the π polarized beam undergoes a minor interaction with the Cu $d_{x^2-y^2}$ orbital. Emitted photons have the electric vector parallel to the ab plane for both polarizations. This causes an equal cross section for both the crossed (spin flip) and non crossed (non spin flip) channels of the same incoming polarization. The best configuration for the presented experiment is the one that enhances the non spin flip channel compared to the other one and, of course, has the highest cross section. For what stated before, the best configuration that fulfils these conditions is defined by positive in plane momentum transfer and σ incoming light.

With the described experimental setup, several spectra at different $q_{\parallel}$ around the "historical" value of 0.25 rlu were acquired at the three different temperatures. To be more precise, the spectra at 20 K and 96 K were acquired during the same experiment, while the ones at 50 K were measured in a subsequent moment.

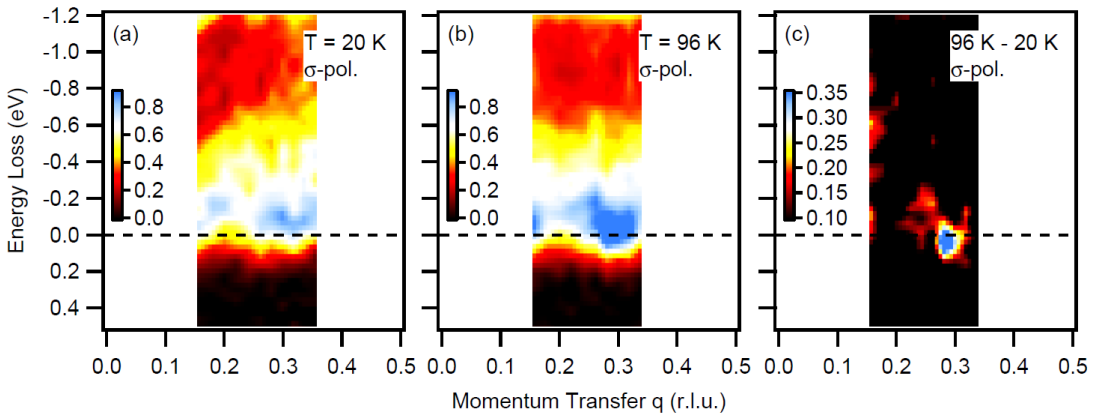

Figure 2.9: Temperature dependence of the RIXS spectra across T_c. (a) and (b) RIXS intensity map taken with σ polarization at $T \sim 20\ K$ ($\ll T_c$) and $2T \sim 96\ K$ ($\sim T_c$), respectively. (c) Color map for $96\ K\ -\ 20\ K$ showing strong temperature dependence at $q_{\|} \sim 0.28$ rlu.

Results

All the spectra shown in this Subsection are normalized to their total intensity, integrated from -3.5 to 1.0 eV. Figure 2.9 (a) and (b) show the color intensity maps of the RIXS spectra at $T \sim 20\ K$ ($\ll T_c$) and $T \sim 96\ K$ ($\sim T_c$), respectively. A region with stronger intensity is evident at both temperatures around $q_{\|} \sim 0.28$ rlu, at energies close to the elastic one (i.e. 0 eV energy loss). In order to examine the difference between $T \ll T_c$ and $T \sim T_c$, Figure 2.9 (c) shows the difference between the two maps at $96\ K$ and $20\ K$. This difference map shows clearly a strong intensity at the elastic energy located at $q_{\|} \sim 0.28$ rlu. This indicates that the strongest temperature dependence of the low energy RIXS spectra in the reciprocal space region in analysis is set around $q_{\|} \sim 0.28$ rlu and consists in a strong decreasing of the elastic contribution by lowering the temperature, starting from T_c and moving towards the superconductive region of the phase diagram.

To further analyse this temperature dependance, Figure 2.10 (a) shows the evolution of the RIXS spectra with $q_{\|}$, at $T \sim T_c$ (red line) and $T \ll T_c$ (blue line). The difference between the spectra at the two temperatures is highlighted by the shade. The strong temperature dependance is once again clear near the elastic at $q_{\|} \sim 0.28$ rlu.

Panels (b) and (c) show respectively the q dependence for the elastic and inelastic part of the spectrum, at the three different temperatures under analysis. The elastic (and quasi-elastic) contribution was isolated from the rest of the signal by integrating

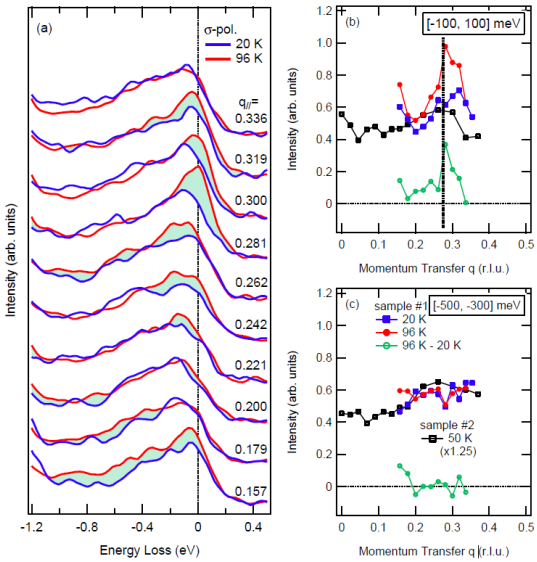

Figure 2.10: (a) RIXS spectra at 96 K (red) and 20 K (blue) at different q ∥. (b) Temperature dependence of the intensity integrated from −0.1 to +0.1 eV for the quasi-elastic signal. (c) Temperature dependence of the intensity integrated from −0.4 to −0.2 eV for the low energy inelastic signal.

the intensity between 0 ± 0.1 eV, while for the inelastic part it was considered an integral between -0.3 ± 0.1 eV. In Panel (b) the elastic signal for $T \sim T_c$ show a clear peak around $q_{\|} \sim 0.28$ rlu, whose FWHMwas estimated to be higher than 0.05 rlu. The peak becomes significantly weaker and broader upon decreasing the temperature below T_c. The evidence of the temperature dependence of this part of the spectrum is confirmed by the difference between the spectra at $T = 96\ K$ and $T = 20\ K$, represented by the green line with open circles in Figure 2.10(b). This line shows a peak, implying that the effect leading to the enhancement of the elastic at $q_{\|} \sim 0.28$ rlu is stronger at $T \sim T_c$ that at lower temperatures. Moreover, this effect involves only the elastic part, as it can be seen by the comparison with Figure 2.10(c), were the same plot is drawn for the (low energy) inelastic part of the spectrum. In this panel the intensity at 50 K was multiplied by a factor of 1.25 in order to make it comparable with the other data. It must be reminded that the spectra at 50 K were acquired during another experiment and in the two cases the intensity ratio between the inelastic and the elastic signal was slightly different. This could be due to some well known causes, as a slightly different alignment of the sample with the spectrometer, different measuring position on the sample surface or different surface cleanliness.

The discussed modulation of the elastic peak at $q_{\|} \sim 0.28$ rlu, has a very similar

behaviour of those found in the "123" family, and thus it was interpreted as a quasi-static incommensurate CDW. It was classified as quasi-static because the related peaks seem to occur at slightly higher energy compared to the elastic, even if the resolution is not sufficient to estimate this discrepancy. This charge modulation seems to disappear by decreasing the temperature below T_c, entering in the superconductive region of the phase diagram, and this suggests a competition between the two order parameters. Moreover, this is the very first time that a charge modulation is detected in optimally-doped compounds, suggesting that it can occur in a wider doping range and not only around $p \approx 0.125$ as observed thus far.

However the FWHM~ 0.05 rlu of the peak in the reciprocal space is significantly larger than those found for the YBCO, of the "123" family, which was ~ 0.02, and LBCO, of the "214" family, which was ~ 0.005. The broader peak suggests that CDW in Bi2212 have a shorter correlation length; further analysis would be necessary in order to understand if this is due to the optimal doping of the sample (compared to the lower doping of the other two cases) or just to the different chemical composition.

Conclusions

The evidence of a modulation of the elastic part of the RIXS spectrum of optimally-doped Bi2212, that shows a peak at $q_{\parallel} \sim 0.28$ rlu, suggests the presence of an incommensurate charge ordering, that can be interpreted as a CDW.

This charge ordering seems to be suppressed by superconductivity below T_c, being consistent with previous detection of CDW. CDW were revealed only in underdoped cuprates thus far, but they were supposed to be in intimate relationship with the pseudogap, that still exists in the optimal doping region of the phase diagram at temperatures around T_c. The presented experiment provides the first evidence of the presence of CDWs in optimally-doped cuprates, reinforcing the idea of the correlation between the CDWs and the pseudogap.

Further systematic study is required to understand the particular values of $q_{\parallel}$ at which the peak occurs in the q space for different materials. Furthermore, a deeper analysis of the FWHM of these peaks could be useful in order to understand the values and the evolution in the phase diagram of the correlation length of these charge modulations.

In the end, it must be stressed again the importance of the use of RIXS in order to detect the modulation of the quasi-elastic signal in Bi2212, that results to be a very weak effect compared to the total intensity of the spectrum. In fact, for the presented experiment, the ratio of the elastic peak modulation to the total integrated intensity was estimated as less than 10%. The RIXS energy resolution allowed to separate the elastic contribution by the rest of the spectrum, making it possible to detect the small peak. Otherwise, with conventional elastic scattering measurement which does not have energy resolution, the tiny quasi-elastic signal may be buried under the large inelastic signal.

Chapter 3

CCD Detectors For Soft X Rays

A CCD image sensor is the detector that allows data acquisition in RIXS spectroscopies. After the diffraction grating, photons with different energies hit the CCD in different positions and after software elaboration on acquired images the spectrum is obtained. Therefore the CCD detector spatial resolution is directly linked to the spectra energy resolution and this makes the CCD detector a critical component to study in order to obtain high resolution spectra.
In this Chapter the general structure and technology of a CCD detector is briefly discussed, together with its functioning for image acquisition. Specific problems connected to detectors used for soft x-rays are then discussed and, finally, the detector currently in use at ESRF and the detector under test at Politecnico di Milano are described.

3.1 CCD detectors technology

An image sensor is a device that converts an optical image into an electronic signal and CCD detectors are, among all, certainly the most widely used sensors for scientific applications. A CCD image sensor is constituted by a matrix of elements, called pixels, that are generally realized using MOS capacitors, which can accumulate a charge proportional to the incoming flux of photons. The spatial division of the incoming flux of photons among pixels allows the spatial sensitivity.
The name CCD, i.e. charge coupled device, is due to the technique used to move

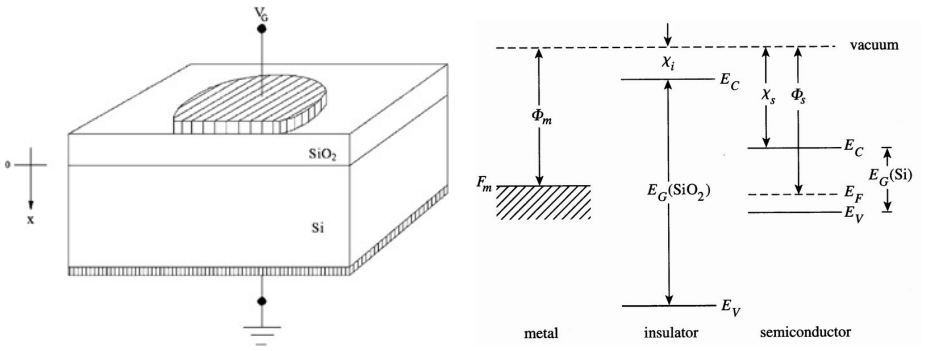

(a) A typical MOS capacitor structure (b) Band diagram of materials constituting a MOS capacitor

Figure 3.1: MOS structure and band diagrams of its constituent.

charge from pixels to a device that performs the conversion into a digital value. This is achieved by "shifting" the signals between stages within the device one at a time. CCDs move charge between capacitive bins in the device, in this case pixels, with the shift allowing for the transfer of charge between bins.

Mos capacitor

In Figure 3.1 (a) the general structure of a MOS capacitor is represented. Over a p-doped silicon substrate, an oxide layer, which works as insulator, and a metallic layer, called gate are grown. A voltage can be applied between the gate and the bulk, in order to change the MOS electric properties and therefore its functioning.

In order to completely understand the behaviour of a MOS capacitor, it is useful to start from the band diagram of the three materials alone and isolated the one from the other (Figure 3.1 (b)). In metal layer, the electronic states below Fermi level are completely occupied, while the states above this level can be considered empty. This situation, to be more precise, occurs only at 0 K temperature, otherwise the transition between the occupied states and the empty ones is less sharp, with a transition region wide $\sim 4k_BT$ in which the states are only partially occupied. The minimum energy needed to remove an electron from the metal is a fundamental property of the material, called work function and defined as $\Phi_m = E_{vacuum} - F_m$.

Both insulating and semiconducting layers present, at 0 K, a valence band completely occupied and an empty conduction band. The Fermi level E_F, for these materials, lays inside the band gap, which is a range of energies forbidden for the electron states. Gap

width is defined as $E_G = E_C - E_V$, where E_C and E_V are, respectively, the lowest energy in the conduction band and the highest energy in the valence band. As for metals, temperature makes the distribution of electrons among the permitted levels less sharp, and thus at $T \neq 0\ K$ some electrons can occupy the conduction band and leave some holes in the valence band. If the material is doped, i.e. a small percentage of different atoms are put inside Silicon, its electronic properties can change. These dopant atoms are called donors, if they add an electron in the conduction band (having a valence electron more than Si atoms and lower electronegativity), or acceptors, if they remove an electron from the valence band (having less valence electrons than Si and higher electronegativity). By introducing these atoms in the silicon substrate its number of electrons or holes is varied, and thus, the Fermi level, which is the value that determines the population of electrons and holes in bands at equilibrium, changes. It is useful to mention two additional parameters in order to completely explain the band diagrams. Electron affinity $\chi = E_{vacuum} - E_C$ is the energy needed to emit an electron from the conduction band; it depends on chemistry and it is almost insensitive to the doping, thus it could be considered as a constant of the material. Furthermore, a work function can be defined for the semiconductor, as $\Phi_s = E_{vacuum} - E_F$; however this is not a constant value for the material because E_F is not fixed once the material is known. In the most part of CCD detectors the semiconducting substrate is p-doped, and thus holes are the majority carrier, which means that they are in an higher percentage compared to not doped (intrinsic) material, while there are less electrons, called minority carrier. In a p-doped material, E_F is closer to the valence band than to the conduction band.

To draw the band diagram of a MOS capacitor the *electron affinity rule* or *Anderson's rule* must be applied, in order to determine how the energy bands align at the interfaces between different materials. At the insulator-semiconductor heterojunction the difference $\Delta E_C \doteq E_C(SiO_2) - E_C(Si) = \chi_s - \chi_i$ is kept constant, while at the metal-insulator interface the quantity that should not vary is ${\Phi'}_m \doteq E_C(SiO_2) - F_m = \Phi_m - \chi_i$, called *modified work function* . Another condition that has to be respected is that, at equilibrium and with no applied voltage ($V_G = 0$), Fermi level should be constant and the same inside the whole structure. These three conditions lead in general (for $\Phi_m \neq \Phi_s$) to a band bending inside semiconductor and

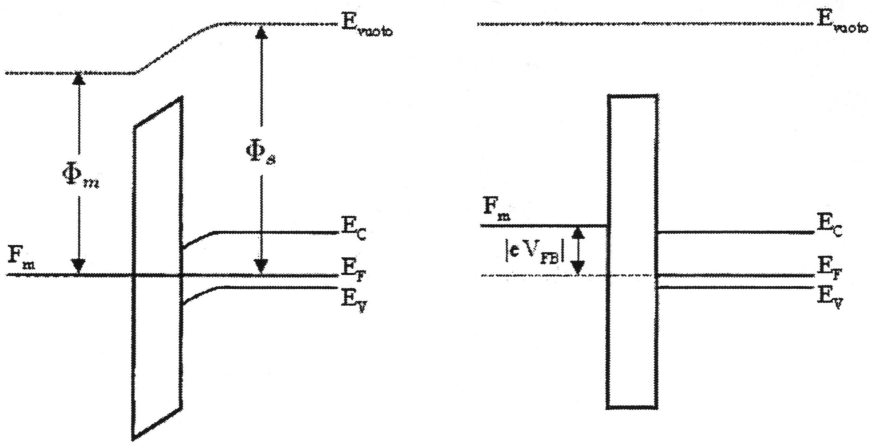

(a) Band diagram with $V_G = 0$ and $\Phi_m < \Phi_s$.

(b) Band diagram with $V_G = V_{FB}$

Figure 3.2: Band diagrams of MOS capacitor with no voltage applied to the gate and in the flat band condition.

insulator, as depicted in Figure 3.2 (a).

MOS regimes at equilibrium

At thermal equilibrium, no steady state current flowing inside the structure is possible, because oxide resistance is very high and does not allow carrier to pass from the gate to the substrate (and viceversa). Since no electron can pass through the insulator, in a steady state there cannot be net flows of carriers in the structure, for example within the substrate, because they would lead to an accumulation or a depletion of charge and thus to a modification of the state, which contradicts the idea of equilibrium. To avoid net carrier flows, Fermi level should be the same within the whole structure, otherwise an imbalance of the carriers concentration inside each energy level would arise along the device. This condition is the one that defines the equilibrium for a MOS capacitor, even when a voltage is applied to the gate and the band diagram is modified.

If a non zero voltage is applied to the gate, a shift of Fermi level of $-eV_G$, where $-e$ is the electron charge, is obtaned. For a specific value of V_G the so called flat band condition is reached and the bands inside semiconductor become flat (Figure 3.2 (b)).

This happens when

$$V_G = \frac{\Phi_m - \Phi_s}{e} \doteq V_{FB} \tag{3.1}$$

In flat band condition, carrier concentration is uniform in the semiconducting substrate and has the same value of the material when isolated. Moreover, remembering that electric field is given by

$$\varepsilon = \frac{1}{e}\frac{dE_C}{dx} \tag{3.2}$$

it is clear that, with flat bands, no electric field is present inside the three layers. By keeping this situation as reference it can studied what happens varying V_G relative to V_{FB}. Let us considered from now on $V_{FB} = 0$ for simplicity.

In Figure 3.3 the band diagram of MOS capacitor in accumulation regime is depicted, i.e. with $V_G < V_{FB}$. Near the junction with the insulator, semiconductor bands bend upwards and the valence band gets closer to Fermi level, that stays still. Therefore near the interface there is a significant increasing in the holes concentration in respect to the bulk value, given by the equation:

$$p = \int_{val.\ band} N(E)\left[1 - \frac{1}{1 + e^{(E-E_F)/kT)}}\right] dE = N_V e^{-(E-E_F)/k_B T)} \tag{3.3}$$

where p is the hole concentration, N(E) is the density of states, k_B is the Boltzmann constant and N_V a number resulting from the integral calculation, that depends on material and temperature. The dependance of the hole concentration on distance between the valence band and Fermi level is very strong, being given by an exponential function in Eq. 3.3. The high holes concentration leads to an accumulation of positive charges Q_p at the oxide interface; this situation is similar to a metallic capacitor, but here charges are present also inside the semiconductor, for few μm before the interface. For the neutrality condition, on the metal surface there is the same amount of charge, but with opposite sign: $Q_G = Q_p$. Inside the insulator an electric field is present that points towards the metal layer, as depicted in Figure 3.3 (b), and penetrates partially into the semiconductor.

Let us now consider the situation in Figure 3.3 (c), where $V_G > V_{FB}$. This is the so called depletion regime, characterized by the semiconductor bands bent downwards at the equilibrium. When the band bending reaches and exceeds some $k_B T$, the holes

population, following Eq. 3.3, becomes negligible in comparison with that of the acceptor ions and thus a so called depletion layer arises, where the concentration of the carriers is almost zero. The total charge in this region, due to fixed ions, is $Q_d = -eN_aW$, where N_A is the acceptor concentration, that is equal to the hole concentration inside the bulk, and W is the depletion layer width. On the metal surface, for neutrality, the corresponding opposite charge $Q_G = -Q_d$ will be present. As in accumulation regime, an electric field arises inside the insulator and penetrates into the semiconductor, but here it points in the opposite direction.

By increasing V_G, the depletion layer width and the band bending increase. The electrons concentration, that is negligible in a p-doped semiconductor bulk, increases exponentially with the band bending following the equation:

$$n = \int_{cond.\ band} N(E) \left[1 - \frac{1}{1 + e^{(E-E_F)/kT)}}\right] dE = N_C e^{-(E-E_F)/k_BT)} \tag{3.4}$$

where n is the electron concentration and N_C is a number depending on material and temperature. An interesting case is given when $n(interface) = p(bulk) = N_A$, that is the concentration of electrons near the interface becomes the same as the concentration of holes inside the bulk; this situation is referred as inversion regime, because the minority and majority carriers are inverted between interface and bulk. The gate voltage at which this occurs is named threshold voltage V_T. The electron concentration is no more negligible for charge balance, thus, total charge accumulated on the gate will be $Q_G = -Q_d - Q_n$, where Q_n is the charge due to the electron accumulation at the interface. If V_G exceeds the threshold voltage, the conduction band keeps approaching the Fermi level, without crossing it, and the electron number at the interface keeps increasing, while the depletion region width stays almost constant, because the whole necessary potential jump, the electric field and shielding charge inside the semiconductor are provided by the high amount of charge accumulated at the semiconductor-insulator interface.

Before approaching the out-of-equilibrium situation, a last point should be underlined. Equations 3.3 and 3.5 describe respectively the equilibrium concentration of holes and

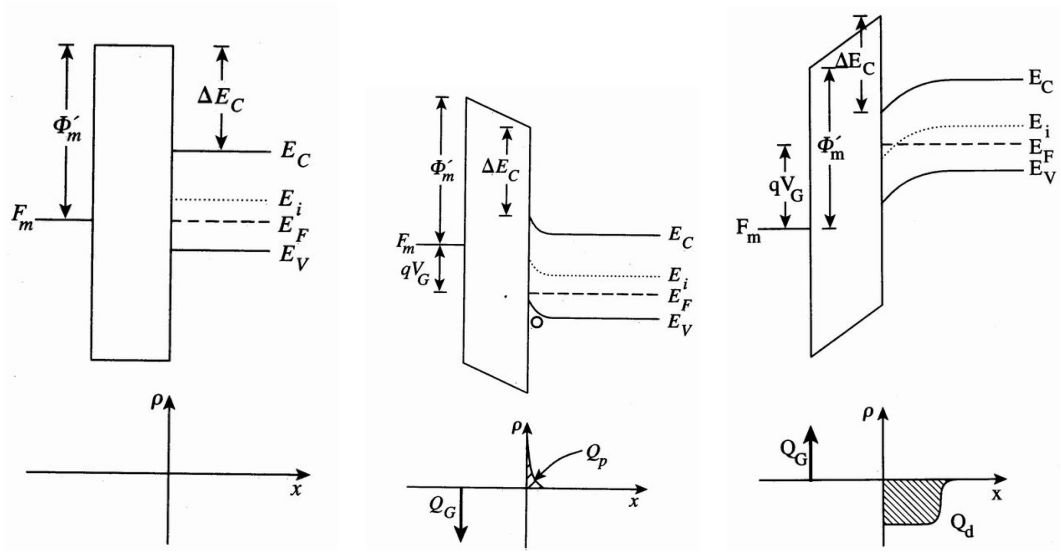

(a) Flat band condition ($V_G = V_{FB} = 0$).

(b) Accumulation regime ($V_G < 0$).

(c) Depletion regime ($V_G > 0$).

Figure 3.3: Band diagrams of MOS capacitor at equilibrium for different V_G values and charge density as function of x position.

electrons in a semiconductor. By multiplying the two equations we get:

$$np = N_C N_V e^{-E_G/k_B T} \tag{3.5}$$

Thus at equilibrium the value np is a constant and depends only on material and temperature. A situation with a value of np different from the equilibrium one, will tend to reach this value after a transitory. This result is known as mass action law and has a general value, deriving from statistical physics considerations.

Out of equilibrium functioning and charge photogeneration

To be used as a light sensor a MOS capacitor should be put in an out of equilibrium condition. When a semiconductor is out of equilibrium, the population of electrons inside the conduction band and holes in the valence band are no more defined by Fermi level E_F. However, the carriers thermalize very quickly within the bands, arranging themselves with a Fermi-like distribution inside each band. Therefore two quasi-Fermi levels can be defined, one for the electrons in the conduction band F_n and one for the

holes in the valence band F_p. Carrier flows inside silicon are then given by:

$$J_n = -\mu_n n \frac{dF_n}{dx} \tag{3.6}$$

$$J_p = -\mu_p p \frac{dF_p}{dx} \tag{3.7}$$

where J is the current density and $\mu$is the carrier mobility. At equilibrium, following what stated before,

$$\frac{dF_n}{dx} = \frac{dF_p}{dx} = 0 \tag{3.8}$$

and, provided that at infinite distance from the interface its perturbation effect is lost, it should be $F_n = F_p$. Thus at equilibrium $F_n = F_p = E_F$, as considered thus far. In an out of equilibrium condition, as the one useful for photon detection, this equation is no more true and F_n and F_p values need to be separated.

Starting from the accumulation regime at $t < 0$ and changing suddenly the gate voltage at time $t = 0$, up to a value $V_G > V_T$, at time $t = 0^+$ the so called deep depletion regime is reached. After a certain time the equilibrium would be reached and the situation would be the one described as inversion regime, but before this to happen a very peculiar situation arises. The electron concentration in the semiconductor conduction band near the oxide interface is very low at $t = 0^+$, because an instant before, in accumulation regime, they were not present and, however, they are minority carriers in p-doped semiconductors. The exceeding holes previously accumulated in the valence band are suddenly pushed far from the interface by the electric field, keeping F_p value constant in the material. Therefore the product np is lower than what expected by the mass action law. Due to the lack of electrons in the conduction band, in the depletion layer F_n is closer to the valence band, and reaches F_p only after many diffusion lengths. The electric field in the semiconductor is not shielded by the electrons at the interface, as it happens in the inversion regime, and thus it penetrates more into the substrate. Thus the conduction and valence band are both very steep near the interface and the depletion layer is thicker compared to the inversion regime. In order to reach the equilibrium state it is thus necessary that the electron concentration near the interface increases, so that F_n reaches F_p and the band bending, together with the depletion layer width, decreases.

This increase of the electron concentration can happen through two processes: charge diffusion towards depletion layer from the bulk, and their subsequent derive driven by the electric field, or electron-hole pairs generation near the interface. When a pair is generated inside the depletion layer, the electrons are pushed towards the interface by the field, while holes move in the opposite direction; so these pairs cannot recombine and the electron accumulation near the interface is thus possible. The electron-hole pairs generation can be accomplished by thermal excitation or photogeneration.

The thermal process is driven by a balance between the generation rate G and the recombination rate R. G is related to the thermal energy available to excite an electron in conduction band and so it depends on temperature; R depends not only on temperature, but also on the number of carriers n and p, because the probability of electron-hole recombination depends on the carrier concentration. Therefore $G = f_i(T)$ and $R = np \cdot f_2(T)$. At the equilibrium the carrier number remains steady, and thus a dynamic equilibrium between the number of pairs generated and recombined per unit time is reached, $G = R$. In the out of equilibrium situation above described, the np product near the interface is lower than the equilibrium one and this leads to a recombination rate higher than the generation one.

The second process that could lead to equilibrium is the pair photogeneration in the depletion layer. This mechanism is the one that allows the use of CCD detectors as image sensors. A photon incident on the substrate, with energy $h\nu$ higher than the Silicon E_G, can be absorbed and excite an electron in the conduction band. If I_0 is the light intensity incident on the substrate, the photon flux is $\phi_0 = I_0/h\nu$, and its value varies along the material due to absorption, with a dependance

$$\phi(x) = \phi_0 e^{\alpha x} \tag{3.9}$$

where α is the absorption coefficient, that depends on material and wavelength. The photogenerated electrons that can reach the oxide interface are those generated in the depletion layer, that drift towards the interface thanks to the field, and those generated within a diffusion length after the depletion layer. These electrons can diffuse before recombining until they feel the field of the depletion layer. The active width thus is given by $W + L_n$, with L_n being the electron diffusion length in the substrate. For high

λ, that is from near infrared to visible light range, it is $\alpha << 1/(W + L_n)$ and thus only a portion of the photons is absorbed in the active region. The charge Q_n accumulated at the interface is given by

$$\frac{dQ_n}{dt} = -e\phi_0\alpha(W + L_n) \tag{3.10}$$

For very short λ, in x-rays range, it is $\alpha >> 1/(W + L_n)$ and so the entire photon flux would be absorbed to generate Q_n giving

$$\frac{dQ_n}{dt} = -e\phi_0 \tag{3.11}$$

However, it has to be considered that in usual CCD detectors, the photon flux has to pass through the gate and the oxide layer before reaching the substrate. Due to the high absorption coefficient of x-rays in materials, the presence of these two layers does not allow x-rays to reach the active region of the substrate, stopping them before. Therefore, sensors used for x-rays detection present a different implementation, that will be discussed in Section 3.2.

Anyway, the photons absorbed in the active layer lead to a charge accumulated under each MOS capacitor which is proportional to the incoming photon flux. This is the signal that constitutes the image, after the analog to digital conversion. In order to have charge accumulation only due to photogeneration, the electron diffusion from the bulk to the interface and the thermal generation should contribute negligibly during the exposure time to the radiation. This is accomplished by using a very high quality Silicon crystal, with no defects, and by keeping everything at low temperature. While exposing the CCD detectors pixels to radiation, the MOS capacitor accumulates the charge generated by the photons absorbed in the active layer, integrating the incoming photon energy during the exposure time. The maximum charge accumulation is limited by the equilibrium electron concentration. If this value is reached, the sensor is saturated.

Charge transfer between MOS capacitors and detector structure

The charge accumulated under each pixel need to be measured in order to conclude the image acquisition. An analog to digital converter is placed at the end of a serial

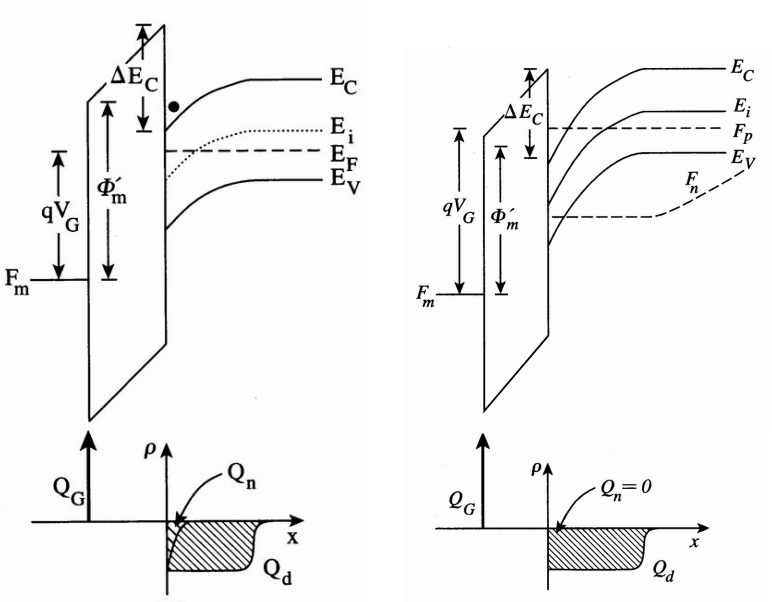

(a) Equilibrium (inversion regime).

(b) out of equilibrium (deep depletion condition).

Figure 3.4: Equilibrium and out of equilibrium band diagrams of MOS capacitor for $V_G > 0$ (and $V_{FB} = 0$) values and charge density as function of x position.

register connected to the pixel matrix and, by moving charge between pixels, every signal reaches the converter and then is elaborated. The mechanism used to move the charge between adjacent MOS capacitors, and that gives its name to the CCD detectors, is called charge coupling. A schematization of the process is depicted in Figure 3.5

At first the photogenerated charge is accumulated under the first gate G_1, at which a voltage $V_{G_1} > V_T$ is applied. The second gate G_2 is biased with a voltage $V_{FB} < V_{G_2} < V_T$ and therefore it is in depletion regime, with no electron at the interface. In Figure 3.5 the depletion regions, or, to be more precise, regions where the energetic bands are significantly bent, are coloured in yellow. Due to the higher voltage applied, a wider depletion layer is present under activated pixels and it can bee seen that these regions partially overlap between adjacent pixels. However, in Figure 3.5 (a), electrons under the first capacitor cannot pass in the adjacent one because of the potential difference, that creates a potential well under the pixel with an higher voltage applied. By increasing V_{G_2} up to V_{G_1}, potential wells under the first two pixels become of the same depth and the charge divides under them equally (Figure 3.5 (b)). If now V_{G_1} is lowered down, the whole charge moves under the second pixel, pushed by the field that arises between the

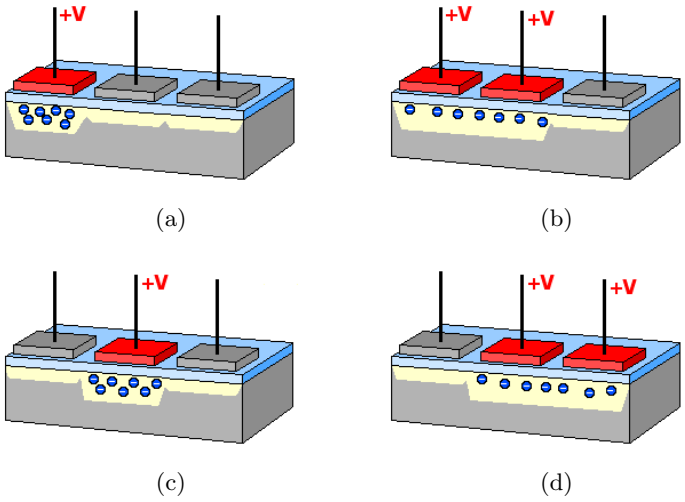

Figure 3.5: Charge coupling transfer mechanism.

two capacitors. The situation at the end of the process is described in Figure 3.5 (c). Then the charge transfer can continue by repeating described steps between the second and the third MOS (Figure 3.5 (d)).

This is the basic process that allows the charge to move from the pixels to the converter. At first each MOS of the bottom row transfers its charge into an array of MOS capacitors, that works as a serial register, and all other rows are shifted one step downward. Then each capacitor in the array transfers its content to its neighbour and the last one dumps its charge into a charge amplifier, which converts the charge into a voltage. Then the output value is sampled and stored in memory. By repeating this process, the controlling circuit converts the entire content of the array into a digital signal. Then all rows are shifted another step down, and the process continues until all pixels signals are digitalized (Figure 3.6). In many CCD detectors the described process usually does not involve directly MOS capacitors used for light integration, but is accomplished by a second matrix constituted by vertical serial registers in which the charge is moved as soon as the exposure to radiation is finished. Some other precautions are useful in order to avoid the mixing of charges of adjacent pixels during signal shifting, but they will not be discussed here, being beyond the introductive scope of this Chapter.

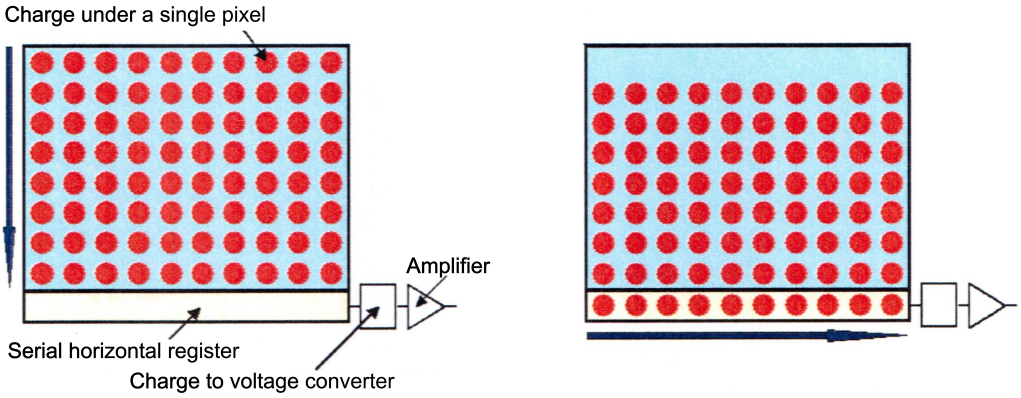

(a) Vertical shift of the charge of each pixel. The charge in the last row is put in the serial register.

(b) Horizontal shift of the charge in the serial register and sequential reading of signals.

Figure 3.6: Charge reading process in a CCD detector.

3.2 Use of CCD for soft x-rays

In the previous Sections the functioning of a generic CCD detector was described. CCDs used for soft x-rays detection share this general structure, but due to some peculiar features of x-rays photons, some specificity is required. This Section will discuss the general structure and problematic of CCD for x-rays and in the end the characteristics of detectors analysed and used for the experiments described in this thesis are then listed.

Thinned back illuminated devices

In CCD image sensors for infrared or visible light detection photons usually come from the gate side and before reaching the active layer in the substrate, must pass through the gate and the oxide layers. Due to the low absorption of these low energy photons inside the $\sim$ 10 nm total thickness of these layers, this is not a problem and almost all photons reach the substrate and can be detected. This is not the case of soft x-rays, which have a very high value of α, and whose photon flux would be severely attenuated before reaching the depletion layer.

A simple solution consists in covering the exposed surface of the detector, i.e. the gate one, with phosphores or other materials that can absorb x-rays and convert them into visible photons, after deexcitation. Another expedient to overcome the absorption

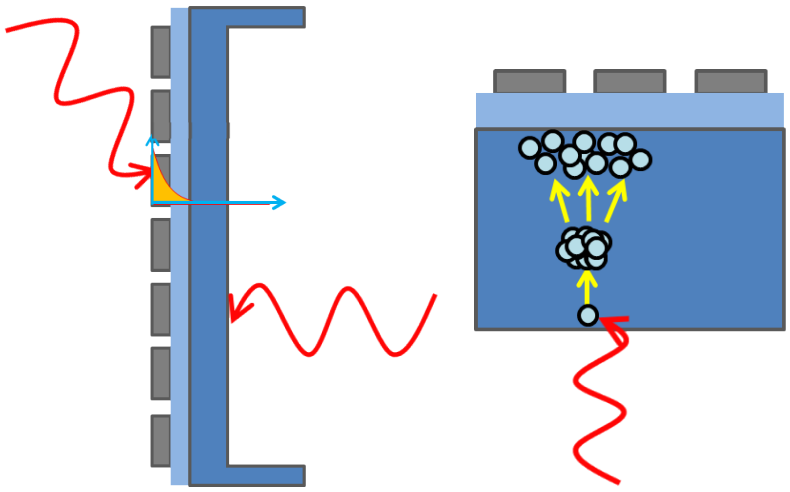

(a) X-ray photons incident on gate side would be abosorbed before the substrate. Thus thinned back illuminated devices are necessary for soft x-rays.

(b) A photon hitting the detector generates a charge cloud that spreads while drifting towards the interface.

Figure 3.7: Thinned back illuminated CCD and charge cloud generation.

problem consists in the use of the so called thinned back illuminated CCDs. This kind of CCD is the most currently used for scientific applications because it guarantees a better efficiency and a complete charge collection [38]. In back illuminated devices the light comes from the substrate side, exciting the electrons directly in Silicon. In order to be accumulated under MOS capacitors, photogenerated electrons have to be produced within the active region of width $W + L_n$ near the interface. Substrate thickness is usually much higher than this value, and thus in normal detectors all the charge would be produced in the bulk and then lost. To avoid this, the substrate is thinned by etching down to $10 - 25$ μm, which is the width of the depletion region in deep depletion regime and thus all photons are absorbed into the active region.

Charge cloud distribution

The effective spatial resolution of CCD detectors was found to be rather independent from pixels size, with pixels with side smaller than 20 μm, when used to detect x-rays. Every photon detected produces a spot on the image that involves several neighbouring pixels and this spot dimension is what limits resolution [39][40].

The process leading to spots generation is depicted in Figure 3.7. An x-ray photon

is absorbed in the substrate and excites an electron, generating an electron-hole pair. The photogenerated electron acquires the whole energy of the incoming photon, which is around hundred times the Silicon energy gap, and then it thermalizes by undergoing several scattering events with nuclei and other electrons. This leads to an avalance process leading to a charge cloud of electrons in the conduction band; the process stops when excited electrons occupy the lower energy levels in the conduction band, and thus cannot loose energy until they recombine.

When generated, the charge cloud is usually smaller than pixel size, being a sphere of diameter given by [38]

$$D = 0.0171(E(keV))^{1.75} \tag{3.12}$$

Therefore, for all photons of our interest, clouds occupy just a fraction of micron as soon as they are produced but, before being accumulated under MOS capacitors, they should drift from photons point of impact to the oxide interface, and during this time electrons diffuse and clouds expand. Clouds expansion is, in general, dependent on electric field that causes drift and on distance that electrons have to go through before reaching the interface.

After expansion, the charge cloud can occupy an area bigger than the single pixel and thus could be split among several neighbouring capacitors, causing a spot in images that limits the resolution. The number of pixels involved depends on the cloud final size and on the position of its center: if it is centered along a pixel edge, it is more likely a splitting among an higher number of pixels, while if cloud's center corresponds to the center of a pixel, the whole charge can be accumulated under one single pixel.

Some studies on the mean cloud size and shape were already carried out by our group [39] showing that in plane charge cloud distribution at the oxide interface is well represented by a gaussian with 25 μm FWHM.

3.3 CCD detectors under test

The CCD detector used in AXES (and that will be used in ERIXS) and the one used for tests at Politecnico di Milano share the same common structure and operating mode, that will be here described. The most important differences will be underlined

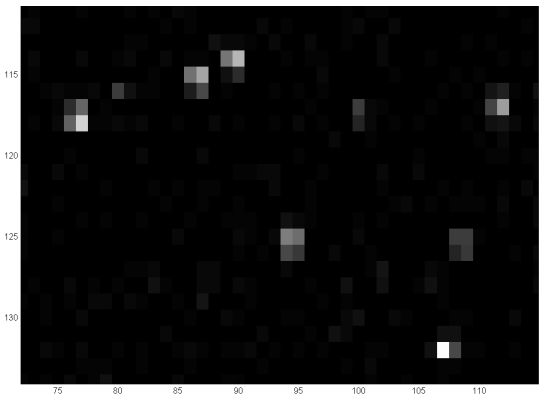

Figure 3.8: Spots generated by photons hitting the CCD.

where needed.

Both of them are produced by Roper Scientific: the former is a Princeton PI-SX 2048 with 20 μm pixel size and 2048 x 2048 pixels corresponding to a total area of 27.6 x 27.6 mm^2 and the second one is a Princeton PI-SX 1300, with 13.5 μm pixel arranged in a matrix of 1300 x 1340, with a total area of 26.0 x 26.8 mm^2. The quantum efficiency of these detectors is higher than 65% in the whole range of interest, between 500 and 1500 eV for the described beamlines, and reaches its maximum at Copper L_3 edge, around 930eV, with a $QE = 85\%$.

In order to reduce as much as possible the electron accumulation under pixels due to thermal generation or diffusion from the bulk, which can generate noise and saturate pixels, both detectors are cooled down. The 13.5 μm pixel size one is cooled down to around $-100°$ Celsius using liquid Nitrogen, while the other one uses Pelter cells and reaches temperatures of $-60°$ Celsius. These temperatures allow to have very low and negligible dark current in both detectors, around 0.003 $electron/s$ rms per pixel for the first detector and 0.043 $electron/s$ rms for the second one. [39]

After the exposure to radiation, the signal of each pixel is converted in a voltage proportional to the charge. An offset is then added to the signal to bring the A/D output to a non-zero value, typically 50-100 counts. This offset value ensures that all the true variation in the signal can really be seen and not lost below the A/D "0" value. Furthermore, this offset helps dealing with dark current, because a portion of the background is ignored during conversion. [41]. After an amplification of the signal

the 16 bit A/D converter allows digitalization. Two different acquisition modes are possible in both CCD cameras, which differ for the elaboration frequency of the A/D converter. The low noise mode converts pixel signal at 100 kHz frequency for both CCDs, while the high frequency works at 2 MHz in PI-SX 1300 and at 1 MHz in PI-SX 2048. All data discussed in this thesis were acquired in the low noise mode, because in our application the reduction of readout noise is very critical. This noise is introduced by electronics while reading and is thus independent by exposure time, being around 4.0 *electrons* rms per pixel for each image acquired. Total noise present in an image is given by root sum squared of the two rms contribution of the dark current and the readout noise.

Another useful operation mode for CCDs considered in this thesis is the hardware binning, that adds data from rectangular groups of adjacent pixels together to form a single pixel, called super pixel. An $m \times n$ binning is accomplished by repeating m times vertical shift of rows inside horizontal serial register, before starting to read register contents, and then by repeating n times horizontal shifts in the register before starting the conversion. An advantage of using the binning is an improvement of signal to noise ratio, because readout noise is introduced only once for all the $m \times n$ pixels. The hardware binning also reduces readout time roughly of an $m \times n$ factor and this is the main reason of its wide use when acquiring images at ESRF for a traditional image elaboration (see Section 4.1). In general grouping pixels can cause a loss of spatial resolution, but this is not the case of ESRF application. As the matter of facts, the only direction on images which is critical for resolution is the one along photon energy dispersion, i.e. vertical direction, while an integration is performed along (quasi) horizontal lines to obtain the spectrum, and thus a binning in this direction is possible without a loss in resolution, with a number of pixels binned that depends on isoenergetic lines inclination. Usually a 1×4 binning is applied and the acquisition time is thus reduced approximately by a factor of 4. Contrary to this application, when single photon counting algorithm is used, binning is forbidden, because by summing signals from adjacent pixels, the information of charge cloud split along horizontal direction gets lost and the number of overlapping spots increases, causing problems also in the determination of vertical position of centroids.

Chapter 4

Single Photon Counting Algorithm

X-rays photons coming from the sample are dispersed in energy by the diffraction grating and hit the CCD surface, leading to charge accumulation under each pixel. After the AD conversion of each pixel's signal, a matrix of numbers is produced, that represents the raw image. Due to the energy dispersion of photons and the focalization on the CCD, the image acquired with the detector is constituted by isoenergetic lines lying approximately in the horizontal direction. These images need to be elaborated via software to obtain the actual spectrum.

In this Chapter two possible algorithms to extract the spectrum from an image are discussed. First of all the most important features of the algorithm currently in use in the beamline, the so called traditional algorithm, are illustrated. Then the idea behind single photon counting algorithms, as the one developed by me during my thesis, is discussed. These algorithms could allow a significant enhancement in spatial resolution of CCD images, and therefore in the energy resolution of spectra. The detailed scheme of the developed algorithm is then presented, together with some supporting functions, which are useful to understand how the algorithm operates on images and to optimize some software parameters.

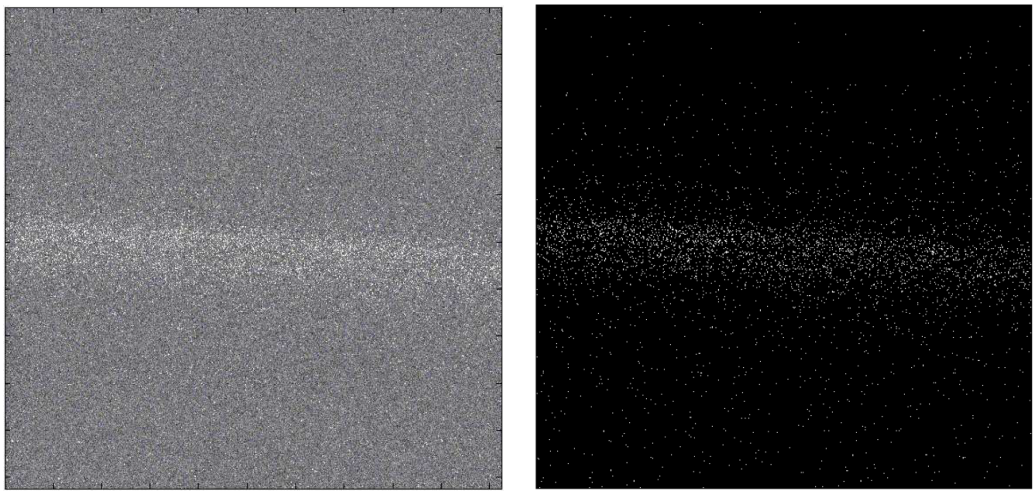

(a) A typical image acquired in a RIXS experiment (raw data).

(b) The image after filtering by traditional algorithm.

Figure 4.1: The effect of filtering on a typical image acquired in a RIXS experiments.

4.1 Traditional algorithm

The traditional algorithm used in ID08 beamline allows an elaboration of spectra from images in a very simple and quick way. No operation on images is carried out apart from band-pass filtering and this allows to employ the software in any experimental condition, without limitation on photon flux, as it happens for single photon counting algorithms, and without the risk of modifying spectra shape. The optical properties of AXES are such that the spatial resolution obtained via a single photon counting algorithm would not bring a significant gain in overall energy resolution of the spectra. At the same time the loss in duty cycle due to the slow read-out mode of the CCD (see next paragraphs) would have reduce the already low counting rate of RIXS experiments at ID08. These are the main reasons behind the the success of the traditional algorithm, that was still in use until the last experiment on AXES and will be installed also in the new ID32 beamline. Due to the importance of this algorithm, and to better understand the improvement produced by single photon counting algorithms on spectra elaboration, traditional algorithm is here extensively described.

Image filtering

The first step of the traditional algorithm consists in image filtering. This is necessary in order to cancel the offset introduced by the analog to digital converter while reading, the readout noise on empty pixels and some very high intensity signals which could be ascribed to cosmic rays. At the end of this process the matrix of numbers representing pixels signals should be made up only of those values, expressed in *Analog to Digital Units* (ADU), due to soft x rays photon hitting the CCD surface.
Offset subtraction is carried out by calculating the mean value of pixels' signals in a dark region of the image and then subtracting this value from the intensity of each pixel of the image. After subtracting this mean value, signal inside pixels that are not involved in the accumulation of charge clouds due to photons is not exactly zero, and this is caused by noise. In order to cancel background noise the traditional algorithm uses a *low threshold* (LT) on pixels: all pixels with a signal lower than this threshold are set to zero value.
There are also pixels with an intensity accumulated which is too high to be ascribed to soft x-ray photons. Usually this signal is caused by cosmic rays and needs to be cancelled to avoid an undesired glitch in spectra. This filtering is again done using thresholds. The *high threshold* (HT) forces to zero the content of all pixels with a signal higher than a number defined by the user. Specific attention should be paid to this value: if too low, it risks to cancel the signal of pixels in regions where an high density of x-ray photons is present, modifying the resulting spectrum shape by reducing the peaks height; if too high, it becomes less effective. Another aspect that must be taken into account is that a threshold, even ignoring the discussed problems, does never completely cancel the intensity due to a cosmic ray. Indeed high energy cosmic rays generate very extended charge clouds constituted by an enormous amount of electrons. These charge clouds are accumulated under several adjacent pixels, with a decreasing intensity moving outwards from the center of the spot. Thus, signal stored in lateral pixels of a cosmic ray spot could be comparable to signal due to a soft x-ray photon. HT should be higher than typical x-ray photons signal intensities, in order to avoid canceling events from spectra, but this involves leaving in the image some pixels filled by cosmic rays spots tails. This effect is shown in Figure 4.2. Both high and low thresholds are defined in

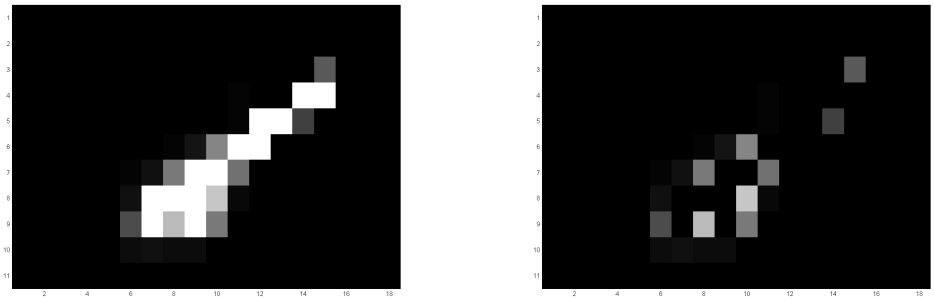

(a) Before filtering. (b) After filtering by traditional algorithm.

Figure 4.2: A cosmic ray spot before and after filtering with traditional algorithm.

units of photons and then converted by the software in ADU, in order to have a better understanding of what the threshold values mean.

Spectrum elaboration with interpolation and channels doubling

The matrix of numbers that represents the image needs to be elaborated via software to obtain the spectrum, that is the intensity of photon flux hitting the CCD versus their energy. This is done essentially by summing pixels signals along an isoenergetic line. These lines are slightly inclined compared to pixel rows, first of all for the impossibility to have a micrometric control of the angle with whom the CCD is mounted with respect to the grating. Moreover, thanks to inclination, each isoenergetic line involves more pixel rows and this can be useful to average possible efficiency variations among different pixel lines, which could cause baseline oscillation often seen in these kind of detectors. The parameter controlling the inclination of the line along which the integration should be done is called *slope*. A simple way to perform the integration is to vertically shift the pixel positions by the value $\Delta_i = -slope \cdot i$, where i is the pixel's column index. As a matter of fact, due to optical aberrations, isoenergetic lines are slightly parabolic shaped, and the correct formula should be $\Delta_i = -slope \cdot i + smile \cdot i^2$, but this is not relevant for our discussion.
Pixels' shifting leads to a new matrix in which the isoenergetic lines are horizontal, and sum along lines could be simply done by rows. However this is possible only if the shift Δ_i is an integer number, because we cannot shift pixels positions in the matrix by a fractional value. So, in real cases, this value should be approximated with an integer,

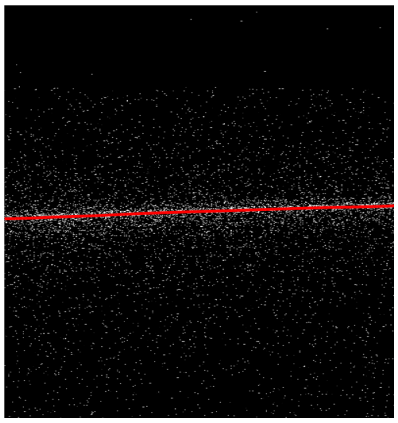

Figure 4.3: Typical image acquired in a RIXS experiment and the isoenergetic line along which it has to be integrated to obtain the spectrum (red).

leading to a maximum error of $\pm 0.5 pixel$, which means a loss of around 50 meV in energy resolution (see the Section 4.1 for details about the conversion). However the contribution of this error is not the limiting factor for the overall resolution of the beamline (around 250 meV for ID08, the beamline at ESRF in which this algorithm was used) and neither for the spatial resolution of the detector, which is limited by photon spot size, which is bigger than one pixel.

A finer way to calculate the spectrum from an image involves *interpolation between adjacent pixels* and *channel doubling*. Both these solutions permit to improve the spectrum definition, the first one by smoothing the spectrum by means of an average between neighboring pixels and the second by doubling the points with whom the spectrum is plotted. The spatial resolution cannot be enhanced much anyway, because, even without the limit of the charge clouds size, it is intrinsically limited by the discretization of pixels, unless we do an elaboration on every single spot as done in single photon counting algorithms.

Interpolation between adjacent pixels avoids the strong approximation to an integer of the vertical shift that has to be applied to each pixel. As we can see in Figure 4.4 (c), if the exact (fractional) shift Δ_i is applied to pixels, shifted pixels fall across cells of the new matrix. Each cell of the new matrix contains part of the pixel whose center was lying over the isoenergetic line and part of the pixel whose center was lying under it. The content of the new matrix cells is thus calculated with a weighted sum of the two pixels falling inside the cell, the weights being proportional to the portion of the

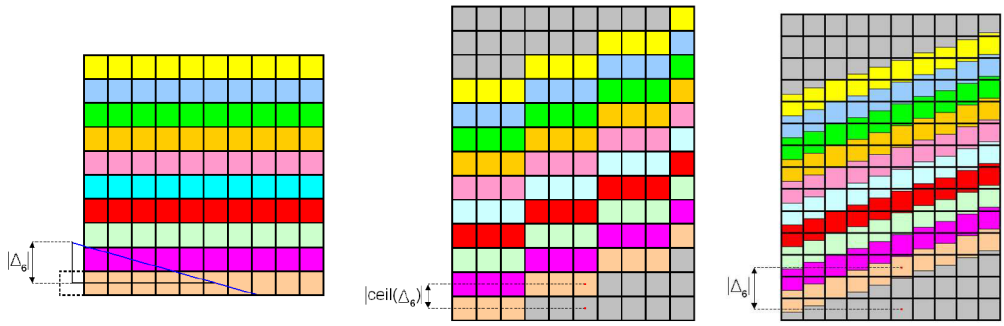

(a) Starting matrix. The blue inclined line indicates the isoenergetic line.

(b) Matrix after the vertical shift of the columns, without interpolation between adjacent pixels.

(c) Matrix after the vertical shift of the columns, with interpolation.

Figure 4.4: Example of the vertical shift (with and without interpolation) of the matrix in order to make isoenergetic lines horizontal. Figure reproduced from Ref. [42].

area of pixels overlapping the cell. After this calculation, the new matrix is summed along rows to obtain the spectrum.

Using this method, the calculation of a single spectrum point involves, in addition to pixels cut by the isoenergetic line, some pixels lying over and some under them, depending on the position of the isoenergetic line inside the pixel that it cuts. This leads to an average among the channels $n-1$, n and $n+1$ to calculate the value of the n-th point, resulting in a smoothing.

The channel doubling is based on the same strategy of interpolation to elaborate the spectrum, but the matrix generated after shifting the pixels has twice the number of cells in the vertical direction, and each cell has half the height. Thus, each pixel of the original image, after shifting, partially overlays 3 cells of the new matrix. The contents of these cells are again calculated with a weighted sum of the pixels falling over them after the shift. This, by actually doubling the points, provides a better definition of the spectrum line, if noise baseline oscillations are not overwhelming.

Energy calibration

The integration along isoenergetic lines provides a two-column matrix, where the intensity of the second column is indexed over the half-pixel step scale of the first column. The last step to obtain an intensity-versus-energy spectrum is to convert pixels' indexes in energies. This process is named *calibration*.

First of all, zero energy loss position is defined using an elastic peak given by a sample that should not exhibit energy losses. A common material used for this purpose is carbon tape, which is already present on the sample holder because it is used to stick samples on the holder. Then the incoming photon energy is varied leading to a variation of elastic peaks position on the CCD detector. By plotting the photon energy versus elastic peak position a straight line is obtained, whose slope gives the conversion coefficient between pixels' indexes and energy losses.
Usual values for calibration in ID08 experiments are around $50 meV/pixel$.

Conversion from counts to photons

Another conversion, not really necessary but very useful to get a better physical comprehension of the intensities represented on the spectra, is the one from ADU to the number of photons incident on an isoenergetic line. An ADU corresponds, in the low noise acquisition method, to approximately 2.5 electrons. The mean energy to excite an electron and generate an electron-hole pair is traditionally fixed to 3.6 eV. Thus a single photon of 930 eV energy could excite about $930/3.6 \simeq 260$ electrons in the conduction band, that is $260/2.5 = 104$ counts in ADU per photon. Therefore the conversion from counts to photons is simply carried out by dividing the number of counts by 104, for our usual electron energies.

4.2 Single photon counting algorithm

The software I have personally developed allows an enhancement of resolution thanks to the reconstruction of the center of each spot, that represents the most likely position of impact of the photon. To avoid errors and spectrum shape alteration, every spot should be isolated and should not overlap with other spots. In order to have a low density of photons on the images but a good statistics on the spectra, many images need to be acquired and analysed individually to find the spots centers. Only after this stage the spots centers can be considered together to elaborate the final spectrum. The algorithm, programmed in MATLAB, starts from the extraction of the single images chosen by the user, analyses them using several parameters and at the end presents and saves the spectrum, together with a good deal of statistical information about spots

and their centers; which is very useful to calibrate parameters and to understand if the software is working as expected.

Centroid reconstruction

The spatial resolution of CCD detectors for x-rays, and therefore the energy resolution of our spectra, is limited by the charge clouds' spot size, which is around 24μm FWHM, usually bigger than the pixel size (as already widely discussed in Section 3.2). The fundamental idea behind single photon counting algorithm that allows to overcome this limit is based on the centroid reconstruction of spots. This can be done because the charge cloud produced by a photon hitting the detector is usually split among some neighboring pixels, each pixel accumulating a charge proportional to its vicinity to the photon's impact position. This situation allows an analysis that uses independently the signals of different pixels belonging to the same spot to reconstruct the exact position of impact of the photon.
Several different algorithms for the centroid reconstruction for soft x-rays photons are currently under study, some of them involving bidimensional fittings [43]. However the calculation of the barycenter (*Center Of Mass - COM*) of spots is the overall most used, the simplest and fastest in terms of computational time, which is very critical when many thousands of spots need to be analysed at the same time. However, this calculation does not guarantee the exact reconstruction of the center of spots, because it can introduce some systematic errors. These errors are anyway expected to be smaller than other errors, caused, for example, by noise, and thus negligible, as it will be shown exhaustively in Chapter 6.

Main algorithm

The main algorithm is the essential part of the software that, starting from raw images acquired by the CCD, elaborates them and provides the spectra. Here the most important steps are presented and discussed.

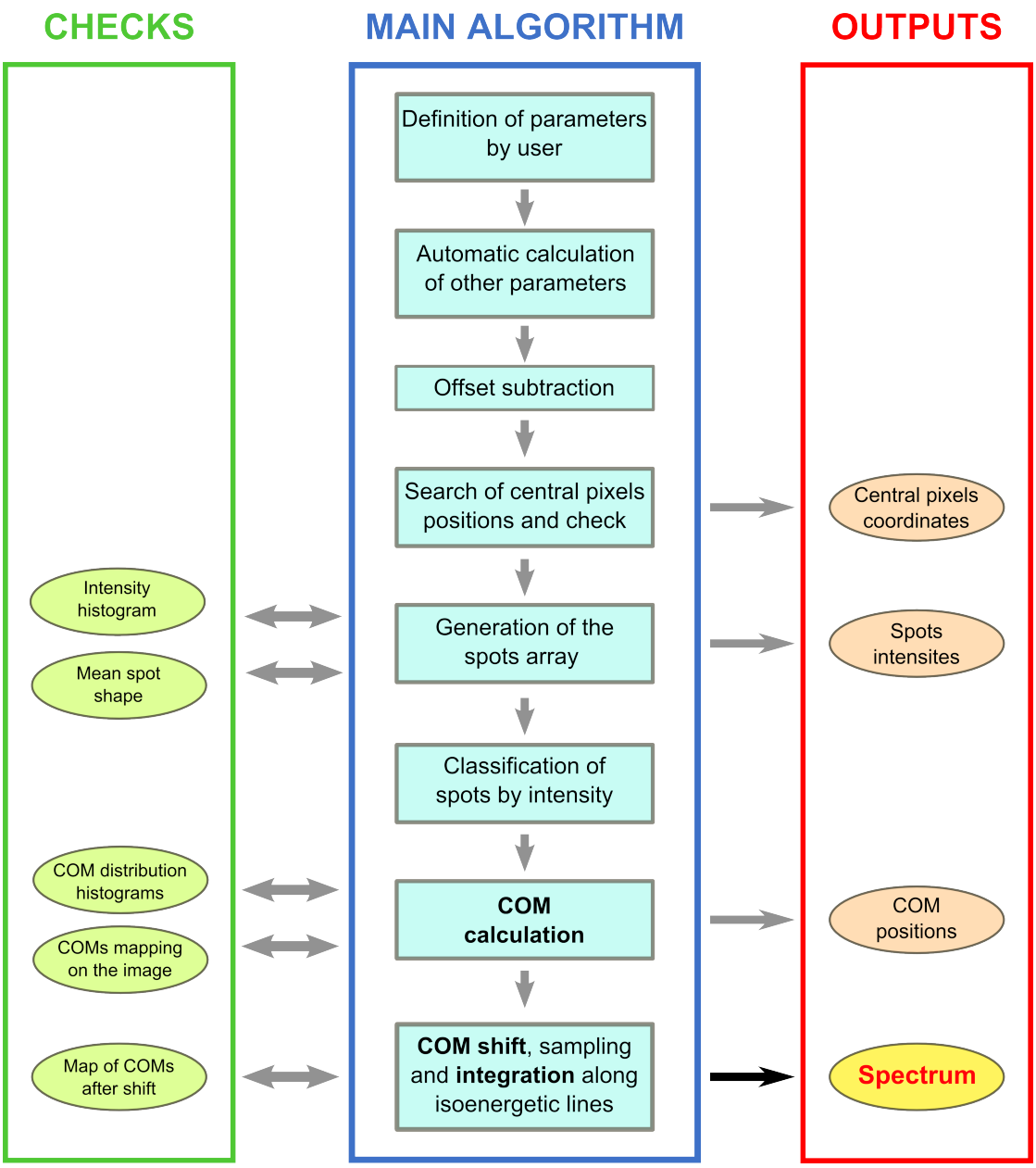

Figure 4.5: Flowchart of the algorithm main operations.

Parameters choice and offset subtraction

As the software is started, images to be analysed are extracted by their file and arranged in a MATLAB matrix. If more than one image is selected, the software stacks them into a three dimensional array, where each layer is occupied by an image.
Before starting the image elaboration, some values need to be introduced by the user in order to set several different parameters. These are not fixed to standard values because

some of them still need to be optimized; moreover some other parameters can vary from image to image, even during the same experiment. The importance and usefulness of these parameters will be clear in the next paragraphs. Here the most important parameters are summarized in a short list, in the same order of appearance as in the algorithm.

First of all a region of interest (ROI) can be activated, so that the analysis will be restricted to the selected part of the image. This is useful to reduce further on the computing time when only a part of the image is significant, as it usually happens in synchrotron experiments, where the required spectrum lies in a narrow horizontal slice. The subsequent choice concerns the selection of the offset to be subtracted to the whole image. This offset is introduced by the AD converter while reading and could vary with time. Therefore it needs to be updated for every image acquired. The version of the software in use at present calculates the offset as a mean on pixels values in a region of image free of photon, which is selected by the user. Otherwise the user can ignore this calculation and insert a value by keyboard. The offset subtraction is very critical for a center of mass calculation, as shown in Figure 4.6. Thus, much attention should be

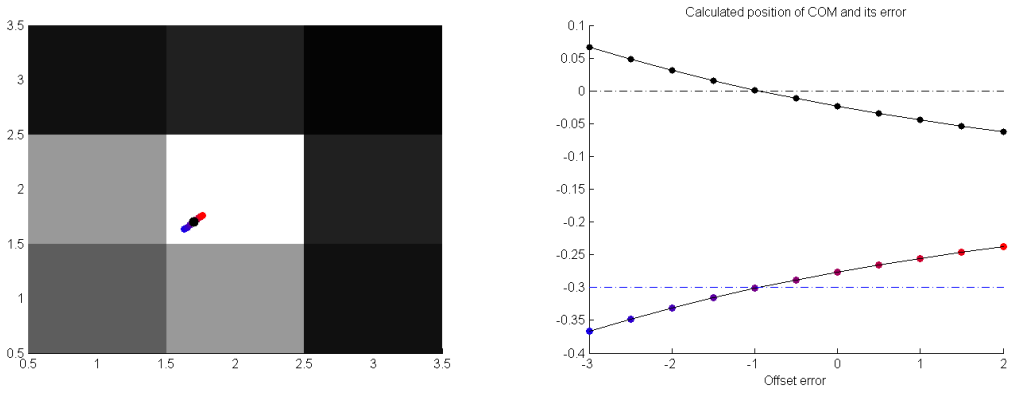

Figure 4.6: (a) COM calculated position varying the error on offset from -3 (blue dot) to 2 (red). The actual centroid position is (-0.3,-0.3), indicated by the black dot (b) COM calculation positions relative to central pixel (points from blue to red) and corresponding error (black). Due to the systematic error caused by COM calculation, the exact position reconstruction is not obtained with zero error on offset. In this case, an offset error of -1, can compensate the systematic error on centroid reconstruction.

paid on the offset value and some other algorithms to subtract offset are possible, as the subtraction of a dark image acquired immediately after the image in analysis.

After the offset subtraction the user should select the size (in pixels) of the area to

consider for each spot and its shape, choosing between a circle or a square. Besides, some threshold values need to be chosen. The first two values, namely high and low central pixel thresholds (HCPT and LCPT), are used by the software to identify which pixels in the image could be central pixels of spots. Too high intensities could indicate a multiple event or a cosmic ray, while signals lower than a small fraction of photon could never be stored in the central pixel of a spot. In fact the central pixel of a spot should be the nearest to the photon impact position, and so it should accumulate a big fraction of the charge cloud. Therefore, pixels with intensities falling out of this two thresholds range are not considered as candidates to be central pixels. Other two thresholds, that is high spot intesity threshold (HSIT) and low spot intesity threshold (LSIT), allow a selection of the spots with the expected intensity. The spots having a too high intensity, which could indicate the presence of a multiple event, or too low, that could indicate a wrong reconstruction of the spot, are elaborated separately. Spots outside these thresholds are separated from the others and analysed apart from spots with medium intensity. All these thresholds have to be expressed in electrons, since the software converts the matrix from counts to electrons to get a better physical understanding of the values.

The last parameters to set are the already mentioned slope and smile, necessary to indicate the shape of the isoenergetic lines, and the number of *subpixels*. The COM positions after calculation are expressed as real numbers and need to be divided among discrete channels to proceed with spectrum elaboration. Subpixels parameter represents the number of subcells in which each pixel is divided along the two directions. This finer grid, to be filled with tags indicating where the COM, and thus photons, are found, is basically what allows the resolution enhancement. The number of subpixels should be chosen as a compromise between the energy resolution and the intensity for each point: having an higher number of subpixels could enhance the resolution and the definition of the spectrum, but it causes an increasing in statistical noise, because the same number of photons are split into an higher number of channels.

Parameter	Task	Value definition
ROI	Region of the image to analyse	User
Offset	Offset subtraction	Calculation on a dark region
Spot size and shape	Generation of the *spot array*	User
Central pixel thresholds (HCPT/LCPT)	Selection of the candidates to be central px	User, according to spot intens. histogram
Intensity thresholds (HSIT/LSIT)	Spots separation by intensity	User, according to spot intens. histogram
Slope & Smile	Determination of the isoenergetic lines	User, verifying on images
Subpixel number	Determination of the number of channels	User, depending on statistics and resolution

Table 4.1: Table of most important software parameters.

Identification and reconstruction of spots

The identification of central pixels of spots is accomplished using the MATLAB function "find" with HCPT and LCPT, which returns and stores the coordinates of the pixels with values included between the two thresholds.
At this stage a crucial part of the software, that permits to quicken the computational time in comparison with previous softwares developed for single photon counting [42], has to be underlined. Instead of keeping images in the form of matrices and scanning them every time we need to find a spot, a three dimensional array is built, containing all spots. The contents of the central pixel and its neighbours are moved in the array spot by spot. Each layer of the array is made up by a square of $N \times N$ pixels, where N is an odd integer number and the identified central pixels occupy the central position of each square. This is represented in Figure 4.7. The actual position in the image of each spot does not get lost thanks to the already stored coordinates of central pixels. This simple idea of building an array, as already mentioned before, grants a substantial save in computational time, for the remaining part of the algorithm. As a matter of fact, from this point on, only built-in MATLAB functions for matrices and arrays are used, and this allows to avoid the use of loops, which are known to be very slow in MATLAB.

Throughout the array filling some checks are carried out on possible spots, in order to

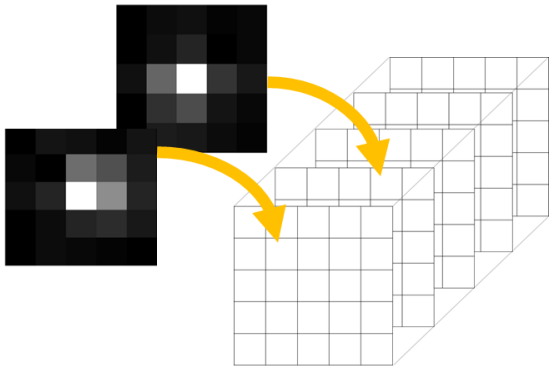

Figure 4.7: Representation of the array containing spots produced by the algorithm during spot identification.

discard preventively possible errors on spot selection and reconstruction. In particular, possibilities of errors rise from the use of thresholds to select the candidates to be central pixels of spots: this method is not sufficient to guarantee that only the most intense pixel of each spot is considered. For example, a possible problem could be due to the nearest neighbouring pixels, which can accumulate a signal comparable with the one of the central pixel. This is likely to occur when the photon falls near the edge of the pixel. If the central pixel and one of its neighbours are both considered as spot centers, two photons would be assigned to that position, causing a modification of the real image. Furthermore, the spots reconstructed around lateral pixels would lead to a wrong centroid calculation, causing a loss of resolution too.

Another cause of fault could generate by the presence of cosmic rays. As a matter of fact, lateral pixels of a cosmic ray spot could store the same charge of the central pixels of our x-ray spots and therefore they would not be canceled by the HCPT. This would lead to assign a photon to every lateral pixel of a cosmic ray. To overcome both these problems a check is carried out on the pixels around the candidates to be the central one. This test involves a comparison among the intensities of the central pixel and every pixel of the $N \times N$ square surrounding it. Candidate pixels that have an intensity lower that their neighbours are discarded and not considered to fill the array. As a matter of fact, the lower intensity stored in these pixels suggests that they are lateral pixels of an

x-ray or a cosmic ray spot, while the one among the neighbours that stores the highest intensity is the central one[1].

The dimension of the square of pixels surrounding each central pixel in the array was kept intentionally independent from the selected spot size, that can be smaller. Thus this test on the relative intensity of the central pixel compared with the neighbours could be carried out on a square bigger than the spot size. This can be useful in some very particular situations, as when two spots partially overlap, but it demonstrated to be of great help when experimental and software parameters have to be set.[2].

Starting from the described array, containing $N \times N$ spots from all images under analysis, another array is generated. In the new array, let us call it *spot array*, only those pixels useful for the analysis on spots are put, i.e. the pixels included in selected spot shape and size. Starting from the spot array and the central pixel positions, the exact position of the center of each spot on the images can be calculated; then these photons positions can be used to elaborate the spectrum.

Center of mass calculation

Centroid reconstruction is accomplished with a center of mass (COM) calculation, which guarantees short computational time and robustness of results. As it will be discussed later, this method could generate some systematic errors, but usually these errors are small compared to the gain in resolution.

COM calculation is accomplished in parallel for all the spots of the spot array. This is maybe the most important benefit for the main algorithm of using the spot array instead of scrolling the image every time to find spots (Figure 4.8). Once COM row and column positions relative to spots' central pixel are known, they are added to the central pixels coordinates, to obtain the exact COM coordinates on the image, expressed as real numbers.

[1] Using this method to filter out cosmic rays, we get rid of the entire spot due to an event, discarding not only the most intense pixels, but also the lateral ones. On the contrary, the traditional algorithm keeps inside the image those pixels, due to a cosmic ray spot, that accumulate an intensity lower than the higher threshold.

[2] Examples of its applications are the check the offset subtraction and the evaluation of the photon density on images. If the spots are far one from the other and if the offset subtraction is correct, the total intensities calculated on an $N \times N$ square of the array and on the smaller area of a spot should be the same. If this is not true, it means that the wider $N \times N$ area includes more than a single spot, indicating a critical density of photon on the image, or that the pixels left out from the spot area contribute to the total intensity with a non zero signal, indicating a wrong offset subtraction

At the end of this stage all information needed about the spots is known and, before going on with the elaboration, it is stored in a resuming matrix. This matrix is returned as output when the software ends calculations, in case of further analysis on this data need to be carried out.

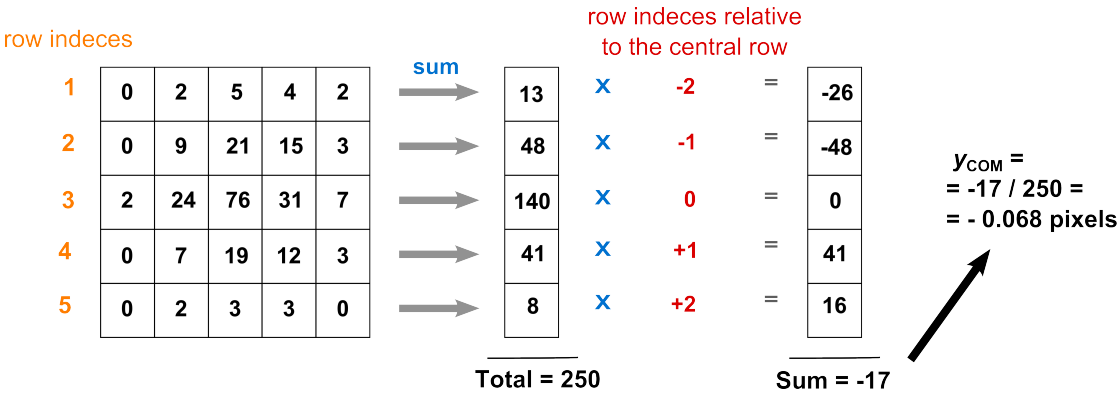

Figure 4.8: Calculation for the vertical position of the COM of a spot. At first the matrix corresponding to a spot is summed along the rows and the results of the sums are put in a column vector. Each row sum is then multiplied by its distance (in pixels) to the central row. All the values in the vector are then summed and the result is divided by the total intensity of the spot. This allows the calculation of COM position relative to the central pixel along the column direction. The same calculation is then carried out by summing columns, to obtain the COM's position along the other direction

Spectrum elaboration

The spectrum elaboration is the last step of the main algorithm. In the traditional algorithm this is accomplished by integrating the filtered image along the isoenergetic lines. In the single photon counting algorithm a sum along isoenergetic lines has still to be done, although the information on which the algorithm works is no more the pixel intensities, but the COM positions: where a COM is found, it means that a photon fell in that point. Contrary to what one can imagine, this makes the integration simpler.
Once the COM coordinates x and y along horizontal and vertical are known, COMs can be shifted vertically in order to make isoenergetic lines horizontal. This involves modifying the y coordinates of the COMs falling along an isoenergetic line, in order to make them equal. To perform this, at every y coordinate of the COMs is subtracted the value of the isoenergetic line in the corresponding x position. This allows to carry out a vertical translation of each COM, according to the isoenergetic line shape.
Before the very last step that produces the final spectrum, spots are divided in three groups depending on their intensity. The COM coordinates of spots with different

intensities (classified as low, medium and high) are put in three different vectors. Then the spectrum is calculated for each one of these groups and for all spots together. The final calculation to obtain the spectrum is the sum of the number of photons falling along horizontal isoenergetic lines. This is accomplished using "hist" function on vertical coordinates of COMs, with bins defined using the selected subpixels value and remembering that vertical image size is slightly different than the original one, due to the COM shift.

The traditional spectrum is also calculated, to have a direct comparison between the two results. After the spectrum elaboration the software saves all useful variables, as the spot matrix, the spectra and the spot array. In addition to the main algorithm it can execute some supporting functions which are not necessary to the spectrum elaboration but could be interesting for an analysis about the spot reconstruction functioning.

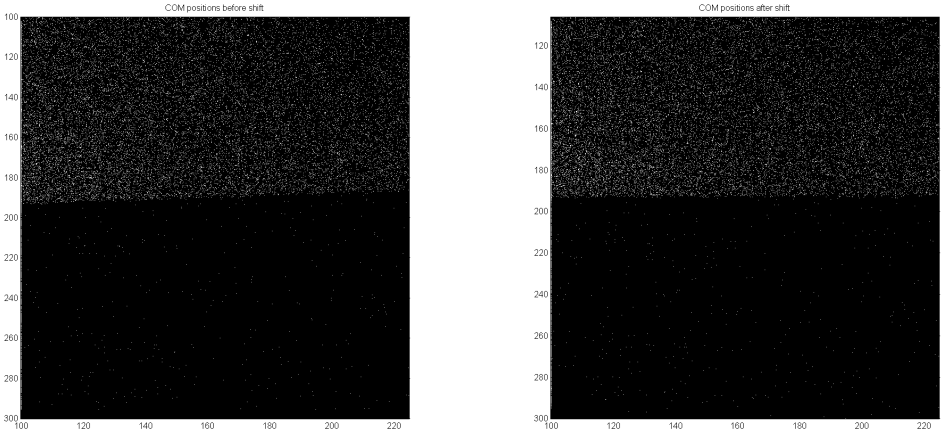

(a) COM positions before shifting. (b) COM positions after shifting.

Figure 4.9: Images representing the COM positions (white dots) before and after the vertical shift. These images are not RIXS spectra, but represent the shadow of a razor blade and were acquired during the resolution tests (see next Chapter for details).

4.3 Supporting functions

Together with the main algorithm, many supporting functions have been developed, that proved to be very useful to understand the algorithm functioning and to set some

parameters. The most important and useful of these functions will be summarized in the subsequent pages.

Spot intensity histogram

The spot intensity histogram represents the number of spots in function of their total intensity. In the ideal case of monochromatic photons and perfect spot reconstruction this "spectrum" should show a single peak corresponding to the spot intensity due to a single photon. This function is useful to understand if spot reconstruction is accomplished in a correct manner, i.e. if all and only pixels corresponding to a spot are considered for the reconstruction, and also to study how many double events are still considered in the final image elaboration. In Figure 4.10 an example is shown, resulting from an analysis on images acquired at ESRF during tests. A very narrow and high single peak is present around 260 electrons of spot intensity, corresponding to 930 eV photons.

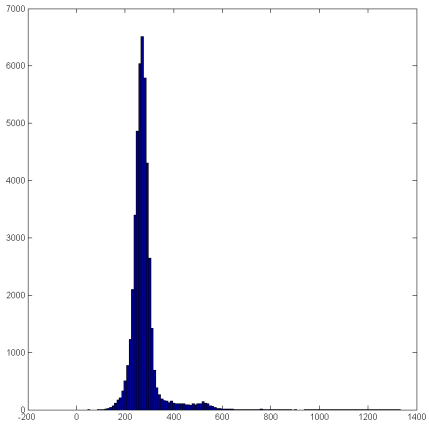

Figure 4.10: Spot intensity histogram for the ESRF test. The horizontal axis is in electrons.

Below this peak there are no spots, indicating that spot reconstruction is complete and that spots only partially reconstructed or reconstructed around lateral pixels are missing. On the other side of the spectrum, there is another very low peak at twice the intensity of the single photon event. This is due to some double events occurring on images. There also can be present some events falling between the two peaks, indicating

reconstructed spots constituted by more than one photon but less than two. This could be caused by two photons falling near one another but not inside the same single-spot area. A lateral fraction of the charge cloud of a photon could be attributed also to the other spot, increasing the actual number of total electrons inside the spot area compared to what expected by a single photon.

Histogram of the distribution of COMs relative to the spots central pixels

The so called *COM relative distribution histogram* indicates the distribution of COMs positions inside the spots' central pixels. In the ideal case this histogram is expected to be flat, because photons can in principle hit the detector with the same probability in every position of a pixel. As it will be discussed later, this histogram was never totally flat during our analysis. This could primarily be ascribed to a systematic error due to the barycenter calculation, that tends to shift calculated COM towards the center of the pixel. COM position histogram are produced independently for low, medium and high intensity spots and along the two directions (vertical and horizontal).

The COM histogram of medium intensity spots, which are those used for the final

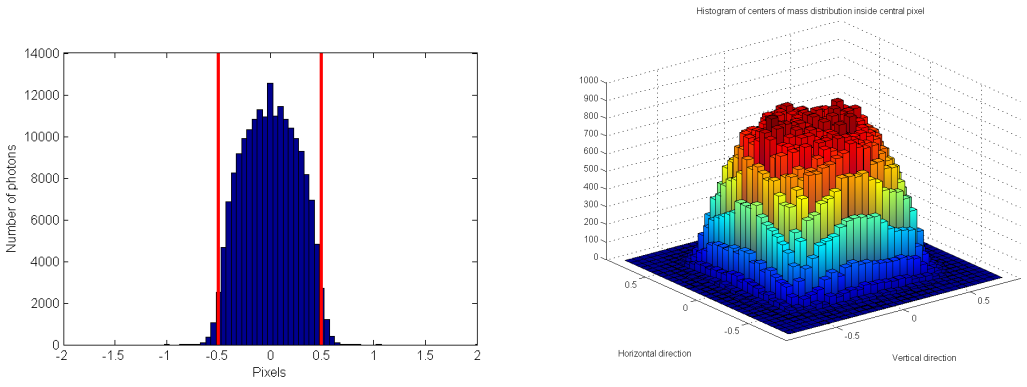

(a) (b)

Figure 4.11: Typical histogram of center of mass distribution within central pixel projected along one direction (a) and in the two directions (b). Central pixel edges are delimited between -0.5 and +0.5.

spectrum, usually shows a broad peak in the center and falls down rapidly near the pixel edges. This shape is the main problem that causes some oscillations on the spectrum line. These effects will be widely discussed later and the importance of the

COM histogram to study and correct all these systematic errors will become clear.
COM histograms provides much information also about the offset subtraction, because, as shown above in Figure 4.6, the offset has a dramatic effect on the calculated COM position. These histograms are also shown in 3D, along vertical and horizontal direction at the same time, and this is useful to study the correlation between vertical and horizontal directions and the depletion effect arising on pixel corners (Figure 4.11).

Spots mapping

The software can draw symbols indicating COM positions on extracted image. It can also be shown which pixels were candidates to be central pixels of spots and which of them have been used for a spot reconstruction. This function, even though it was very useful while programming to take a direct check on spot reconstruction and COM calculation, is no more much informative in the final version of the software. However it was left in the software because it could become useful to test some future possible changes in the algorithm.

Mean spot shape analysis

The last analysis the software performs to get as much information as possible about spots is a study of the mean spot shape. This analysis was very useful to compare our results with data of the literature [39] and, at a later stage, to decide what shape the charge clouds have. This shape was then used to produce some simulated images to test our software under completely controllable experimental parameters.
To study the real mean spot shape it is not sufficient to carry out an average of the spot array along its third dimension, because spots in the array are not perfectly aligned, having their calculated COMs dispersed inside their central pixel and not at the center of the spot square. Therefore this average would lead to a wider spot shape. Furthermore, the resulting shape would be influenced by the pixel discretization, that involves a calculation based on only few points. The resulting shape function would be represented by a stepped line, in particular when spot FWHM is expected to be comparable with pixel size, as it is in this case (Figure 4.13, left side).
To overcome both these problems, each pixel of the spots inside the array is firstly

divided into a denser grid. This operation allows us to shift cells of this grid in order to put the one containing the calculated COM in the center of the spot square, as shown in Figure 4.12. Each spot is shifted by a different number of grid cells and hence, when the spots' average is made, the resulting gaussian-like shape is no more defined in steps, because initial spot pixel edges are no more superimposed (Figure 4.13, right side).

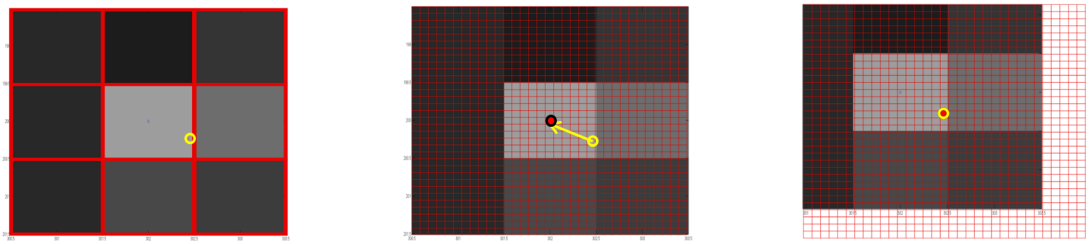

Figure 4.12: Procedure used to recenter spots in the array in order to determine the mean spots' profile. (a) A spot before recentering, with calculated COM indicated by a yellow circle. (b) Division of each pixel of a spot in a denser grid and shift to center. (c) Spot after shifting.

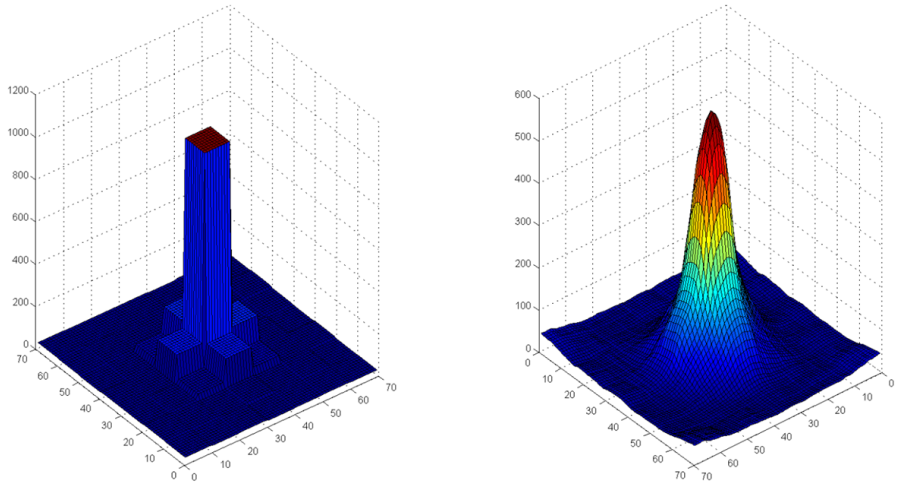

Figure 4.13: Sum of all spots of the 3D array before shifting and after shifting. In plane axes units are tenth of pixel.

To determine the function that better describes the shape, a 2-dimensional gaussian fit was performed, resulting in a standard deviation of around $0.55 - 0.65 pixels$, that, with 20 μm pixels, means $11 - 13$ μm. This means that the FWHM of the charge cloud is around $25 - 30 \mu m$, in good agreement with preceding studies [39]. Once this shape is known, one can think of fitting each spot with the bidimensional gaussian, in order to

have a finer method to find spots COM, that considers correlation between the horizontal and vertical directions. The knowledge of this averaged spot shape was useful also to produce some simulated images, that will be treated in Chapter 6.

Chapter 5

Resolution Test Experiments

In order to evaluate the resolution achievable with the single photon counting algorithm presented in the previous chapter, some tests have been carried out. An experimental set up for similar resolution tests on CCD for x-rays was already available in our group's lab in Politecnico di Milano and I contributed to restore and adapt it to our purpose. The results of these tests proved an excellent resolution enhancement obtained using this software, even if some work has still to be done in order to prevent the arising of artifacts on the elaborated spectra. The aim of this Chapter is to describe the experimental set up, the analysis methods and finally discuss the results of these experiments.
A very quick test was also performed in ID08 at ESRF during a beamtime and it will be briefly discussed in the end of this Chapter.

5.1 Experimental set up

The experimental set up for resolution tests in Politecnico di Milano is very simple and allows a direct measuring of resolution.
The x-ray photons are produced by a traditional x-ray lamp, with a copper anode. The copper anode was chosen because the photon energy of interest for RIXS spectroscopies on cuprates is around 930 eV, that is the Cu L_3 edge. Such a source does not provide a monochromatic beam, in particular, in addition to x photons, a big amount of visible light is produced. In order to stop these low energy photons a tiny aluminium foil is put

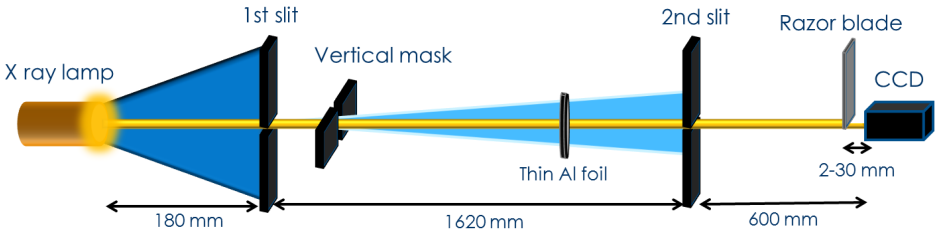

Figure 5.1: Sketch of the experimental set up in Politecnico di Milano, top view.

on the beam path.

The source size on the lamp is about 2 millimeters and thus the resulting beam has a large size and an high divergence that need to be reduced to carry out the resolution tests. Two horizontal slits, both controllable using micrometric screws, are present on the beam path and allow a reduction of the horizontal divergence. Moreover, in order to reduce the beam size also along the vertical direction, a mask with a fixed slit is used. The vertical divergence is not interesting for the present tests, because the resolution is evaluated along a single direction, the horizontal one. This "one dimension" resolution test was designed in order to recall the use of the CCD detector for spectroscopic applications, where an integration along isoenergetic lines is performed before obtaining the spectrum. The collimated beam hits a razor blade on its cutting edge and half of the beam is thus stopped by the blade, while the other part reaches the CCD, drawing the shadow of the razor blade on acquired images. The evaluation of the achieved resolution is carried out by analysing the sharpness of the shadow of the blade edge on images.
Two turbomolecular pumps, one on the lamp side and another on the detector side, guaranteed a vacuum of 10^{-8} mbar.

Diffraction effects

In order to adapt the experimental setup to our purpose I designed a vacuum chamber hosting a x y z manipulator for the razor blade mounted on a top position and the CCD detector at one end. In addition to this, I designed a blade holder connected to the manipulator that allows to control the blade position at a distance between 2 and 30 mm from the CCD surface.

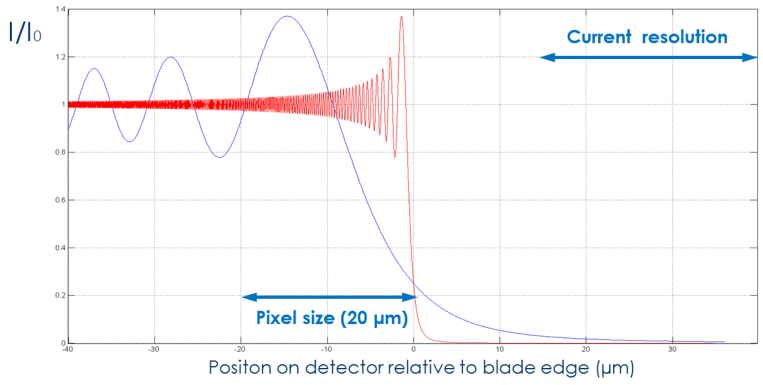

Figure 5.2: Expected intensity profile on the detector due to diffraction effects with a blade-CCD distance of 20 cm (blue line) and 2 mm (red line).

The importance of putting the blade so close to the detector is due to the diffraction effects. Some simulations were performed by Greta Dellea, a PhD student of our group in Milan to evaluate the incidence of the diffraction on these resolution tests. The results of simulations are shown in Figure 5.2, where the expected intensity profile on the CCD surface in the direction perpendicular to the blade is plotted for two different blade-CCD distances. The experimental set up previously in use imposed a blade-CCD distance of around 200 mm and this caused a severe loss of the edge sharpness in images, resulting in a very soft step of 20 μm width (blue line in figure). In addition to this, some broad oscillations were present, the first of which having a period of about 14 μm. These two effects limited the maximum achievable resolution and thus it was necessary to cancel diffraction effects before testing the single photon counting algorithm, that was expected to resolve a fraction of pixel. By putting the blade at 2 mm from the CCD surface, the blade edge shadow becomes sharper (red line), with a step transition from light to darkness of around 2 μm width and very fast oscillations of 1.2 μm period, which would be averaged by the CCD's 20 μm pixel size.

Using this experimental set up many images under several different experimental parameters were acquired. The aim was to test not only the functioning of the single photon counting software, but also its limits when the photon flux is too high. Other tests have been performed varying the slits opening and the blade position, in order to study the importance of the beam divergence for the experiment results. In following Sections the most important test, that demonstrates the resolution enhancement

achieved, will be discussed. Other test results will be not shown because the data analysis is still ongoing and some other measurements need to be carried out.

5.2 Images acquisition and parameters definition

Once the software and the experimental set up were ready, a long work was needed to find the best experimental and software parameters to carry out the analysis. A brief discussion about parameters is thus useful for a full comprehension of the experiment and to have some control values to repeat it in future.

Acquisition parameters

The first value to decide before starting the acquisition is the photon density on each image. Having a low photon density is critical in order to avoid the overlap of spots, that causes a wrong reconstruction of these spots and leads to errors in the barycenters' calculation. In order to find out the best photon density some simulations were performed by our group. The probability to have an isolated spot in function of total number of spots is plotted in Figure 5.3. The calculation was based on a 2D Poisson statistic [44]. Basing on these simulations, it was decided to acquire images with a number of photons in the selected ROI lower than 100. In this situation, less than 5% of spots should overlap.

In order to obtain this extremely low photon density on the images, two experiment parameters could be varied: the flux of photons hitting the detector and the CCD exposure time. The photon flux is determined first of all by the value of the parameters that control the x-ray lamp. The voltage was kept fixed at 3 kV during the experiment even if the interesting photon energies were around 930 eV (Cu L_3 edge), because it is well known that a voltage higher than twice the required photon energy is needed to obtain an high percentage of desired photons compared to the total bremsstrahlung radiation. The current flowing inside the filament was kept around 3 A and periodically adjusted to keep constant the emission current at 1.55 mA. The photon flux on CCD was controlled also by the slits, whose aperture were both kept at 40 μm: the more the slits are closed, the less photons pass through them, resulting in a better collimation and a lower photon flux.

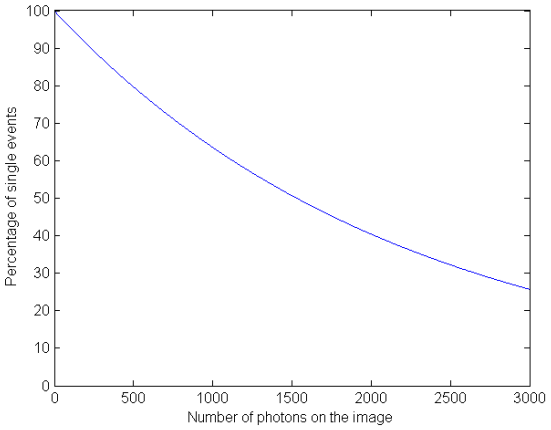

Figure 5.3: Analysis of the percentage of single events versus the total number of photons on a 100×225 pixels image. The spots shape used in the calculus, for simplicity, was a circle with the same area of a square of 3×3 pixels, which is the most used spot size in our analysis.

The other parameter defining the photon density on images is the CCD exposure time for each image. This time needs to be small in order to have a low photon density, but it cannot be too small because it would result in a loss of duty cycle. As a matter of fact, the CCD readout time is around 40 seconds if the whole detector area is used, while the exposure time required to have few photons on each image could be lower than this value. A low duty cycle does not only cause a loss in efficiency, but could lead also to other problems, as an image modification[1].

Therefore the readout time needs to be shorten and this can be done by reducing the region of the image read by the CCD. Due to an imperfect alignment of different elements of the experimental set up, during experiments the illuminated region of the CCD was already limited to an area of 400×300 pixels. Therefore the acquisition was reduced to this area, resulting in a readout time shorter than ten seconds. The exposure time was then set to 20 seconds, achieving a sufficient duty cycle.

During acquisitions the detector temperature was kept at $-60°$ Celsius thanks to its own Peltier cells; at this temperature the dark current was expected to be less than 0.005 electrons per pixel per second. The CCD was used in the low noise mode, characterized by a digitalization frequency of 100 kHz and a readout noise of 3 electrons rms. The

[1] If, for example, the readout time was higher than the exposure time, the major part of photons would hit the detector while reading the image. While carrying out the reading, the CCD shifts the matrix representing the image relative to the pixels matrix, as discussed in Section 3.1. Photons hitting the CCD when the image is shifted would thus be assigned to a wrong position on the acquired image, causing a modification of the actual image

CCD was mounted rotated by 90° because the interesting direction for our resolution tests was the vertical one for the CCD, but the experimental set up allows to perform resolution tests only along horizontal direction in the laboratory space. Thus, images acquired by the CCD are rotated of 90° compared to real space positions.
The blade-CCD distance was set to 6 mm and in order to avoid vibrations of the blade the turbomolecular pump near the detector was turn off during measurements. However the vacuum never exceeded 10^{-7} mbar during the whole experiment.
With this experimental parameters, 18 hours of acquisition were performed, resulting in 18 groups of 180 images of 20 seconds each.

Software parameters

In Figure 5.4 (a) the sum of a set of 180 images is shown, together with the contour of the analysed ROI and the line along which the integration to obtain the intensity profile was performed. The blade shadow is in the lower part of the image, while the upper part is illuminated by x-rays. The illuminated region is not uniform, primarily because of inhomogeneities in the lamp. Therefore, the ROI selected to be analysed is smaller than the image size, in order to perform the analysis only where it is useful for the resolution test. The sum of 180 images reveals many detector defects, not visible on the single images (Figure 5.4 (b)). These defects were expected to be found on images, because some oscillations of the baseline were already observed during experiments at ESRF with this detector in the past years.

The most important software parameters to set for the analysis were the thresholds. The lower threshold on the spot central pixel (LCPT) was set to 30 counts, that is 75 electrons. This is a quite low value compared to the usual central pixels intensities, but it was chosen in order to be sure to consider all possible spots on images. The only possible problem arising from a low LCPT could be a longer computational time, because the mentioned test needs to be carried out on an higher number of pixels.
On the other hand, the higher threshold (HCPT) has a big influence on the software outputs. The charge cloud usually splits among neighbouring pixels and therefore the central pixel in general accumulates only a small fraction of the total intensity. Anyway, it can occur that some clouds are accumulated almost exclusively under a

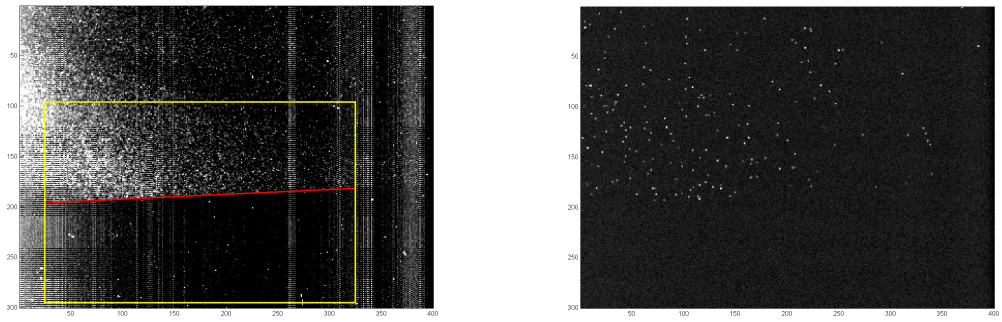

Figure 5.4: a) Sum of 180 images of 20 seconds each. Analysed ROI is contoured with a yellow rectangle and the red line indicates the slope for the integration. b) One single image of 20 seconds.

single pixel, generating the so called *single events*. The COM calculation on these *single events* is impossible, because there is no intensity in the lateral pixels, and thus they need to be discarded to avoid artifacts. This can be done by using an HCPT lower than the total spot intensity: in this way, *single events*, having the whole spot intensity inside the pixel, exceed the HCPT and are not considered by the software. Therefore HCPT was set to 85 counts, that is 212.5 electrons, while the expected spot intensity is 260 electrons for 930 eV photons.

The spot intensity thresholds were set to 80 counts for LSIT and 160 counts for HSIT (that is respectively 200 and 400 electrons). This wide range was chosen because of the non-monochromaticity of the beam coming from the lamp. Narrower thresholds would have lead to discard the majority of photons coming from the lamp, which have energies that differ from 930 eV. The spot size is supposed not to vary much inside this range, so this value should not affect the analysis.

In order to set the parameters related to spot shape and size some attempts were made. The optimal results was obtained with squares of 3×3 pixels for each spot, i.e. only the central pixels and their nearest neighbours were considered. Wider spots did not seem to guarantee a better COM calculation, with 20 μm pixels, because the signal inside the second neighbours is zero or overwhelmed by noise. These ideas were then confirmed by simulations (see chapter: 6).

The determination of slope was tricky, because on a 20 seconds-image the number of photons was too low to see the exact blade edge inclination, while the sum of many images was severely affected by noise, as it is evident in Figure 5.4. The final value was

set to -0.048 and the resulting line is shown Figure 5.4 (a). It must be stressed that an error of 2% on slope can involve an error of a quarter of pixel on final resolution, considering a ROI wide 225 pixels. The achieved resolution was expected to be comparable with a quarter of pixel; thus much attention must be paid to the slope value in these experiments.

The final parameter to set was the number of subpixels used to divide each pixel. In order to have a good image definition 11 subpixels were chosen; an odd number was preferred in order to have a channel corresponding to center of the pixel.

After the acquisition and elaboration of images, the 18 profiles obtained by the 18 groups of images were aligned by eye and then summed together. An alignment by software, maximizing the correlation between different profiles, was attempted but it didn't provide credible alignment because the contribution of noise and oscillations were overwhelming.

5.3 Results

In Figure 5.5 experimental results are shown. The black dotted line is the result of the single photon counting algorithm and the blue line with circles is the profile obtained with the traditional algorithm. The traditional algorithm profile was rescaled by a factor of 7 in order to plot the two curves together. The theoretical scale factor is given by the ratio between the number of points per pixels used by the two algorithms, i.e. $11/2 = 5.5$. In fact, the number of points per pixel defines the number of channels in which photons are divided, and thus the mean intensity accumulated in each channel.

The discrepancy between the theoretical value and the real one suggests that some events are discarded by the single photon counting algorithm. These events are the above mentioned single events, the multiple events and the spots with intensity out of the selected range.

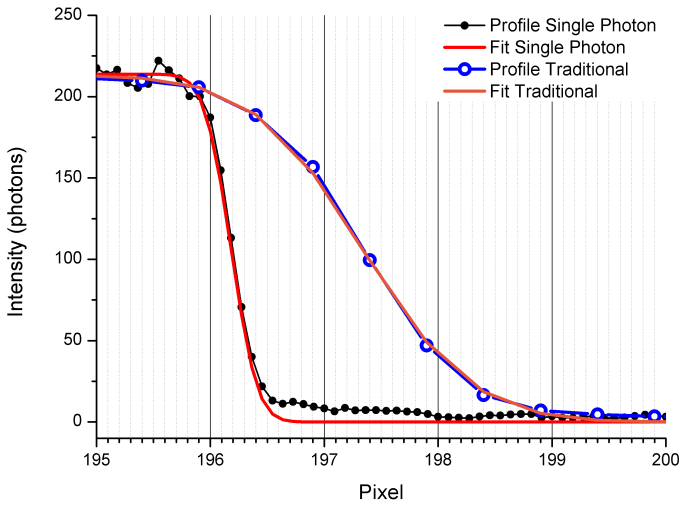

Figure 5.5: Experimental results of resolution tests.

Resolution estimate

In order to evaluate the achieved resolution a fit of the obtained profiles was performed. In the ideal case of infinite resolution, the profile of the blade shadow should be a step function, but the limited resolution softens the transition from light to darkness. Supposing that the system's response to a point source is represented by a gaussian, the experimental profile should be given by the convolution between a gaussian and a step function, i.e. an error function. Therefore a fit with an error function was performed and the resolution was then estimated using the $FWHM$ of the gaussian. The red and orange lines in Figure 5.5 illustrate the fit results.
The resolution enhancement is evident from the graph, where the gaussian's $FHWM$ changes from about 2.5 pixels when traditional algorithm is used, to 0.6 pixels with single photon counting algorithm. The corresponding resolution are estimated to be around 7 μm with single photon counting method and 30 μm with traditional one.
To find the absolute contribution of the image elaboration to the combined resolution other analysis should be carried out, varying other parameters as the blade-CCD distance and the slits openings to determine their influence. Furthermore, a finer analysis on the optimal slope value should be carried out, because, as already discussed, a little variation of the slope could cause a very important error on the

resolution estimation.
However, the presented values indicate an enhancement in the resolution of about 4-5 times using the developed algorithm, which is an excellent result for this preliminary analysis.

Problem: oscillations

Despite the above discussed great results about the resolution enhancement, a possible problem for the future applications of the software was observed. An modulation of the intensity, with one pixel period, was observed on the images obtained after the elaboration. This modulation can cause severe oscillations along the final profile (or spectrum) and therefore it is very problematic for applications. The cause of this oscillations is an error introduced by the COM calculation, that will be discussed in the next Chapter, using simulated images.

COM distribution histograms

The histograms representing the distribution of the calculated COM positions inside the spot central pixel, the so called *COM position histograms*, were very useful to understand the origin of these oscillations. In Figure 5.6 the COM position histogram relative to low, medium and high intensity spots are depicted, together with the one resulting by the sum of the previous three.
Both medium intensity spots' and all spots' histograms show a broad peak in the center and a fast drop near the edges of the central pixel. This effect was later confirmed by the simulations (see Chapter 6 for details) to be caused by the centroid reconstruction through a COM calculation. This kind of calculation may involve a systematic error that shifts the calculated COM positions towards the center of the pixels. This higher probability to assign a photon in the center of the central pixel causes a modulation of the intensity inside each pixel of the final image and this leads to the presence of oscillations in the final spectrum.

For the sake of completeness also the histograms relative to low intensity spots and high intensity spots are depicted. The former is characterized by a narrower peak shape. Low intensity spots generate smaller charge clouds, that do not split much

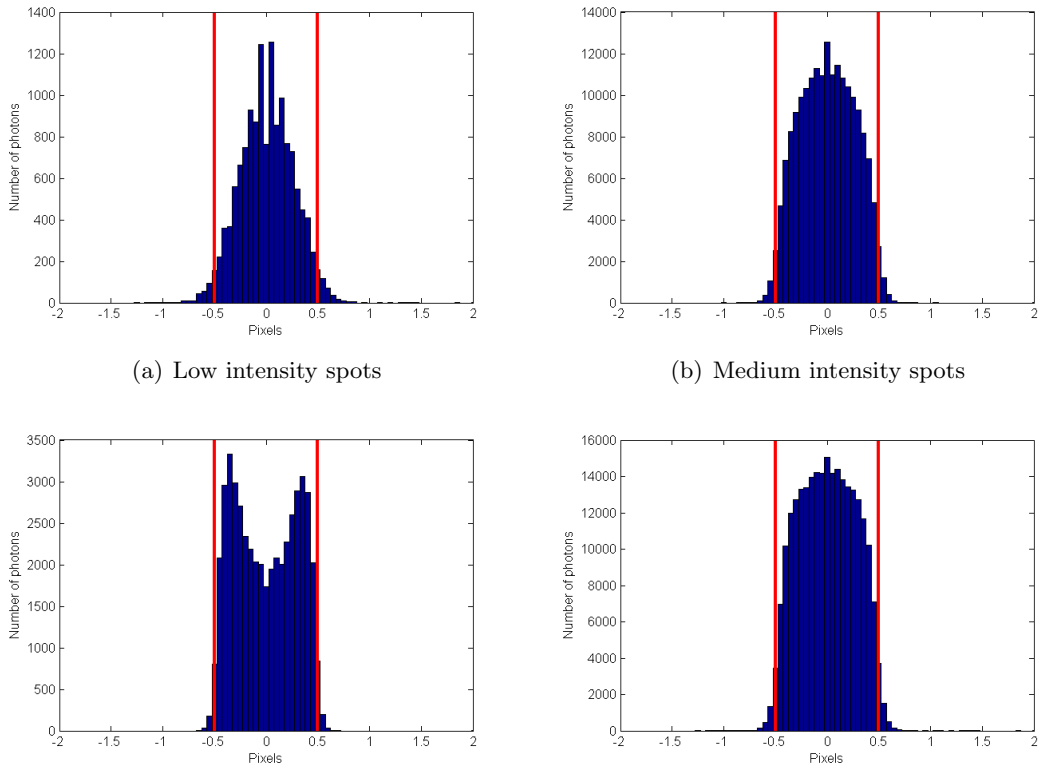

(a) Low intensity spots

(b) Medium intensity spots

(c) High intensity spots

(d) All spots

Figure 5.6: Histograms of the center of mass distribution inside the central pixel. The central pixel edges are represented by red lines.

among neighbouring pixels, and therefore the signal is accumulated almost exclusively in their central pixel. Therefore the COM calculation on such spots assigns the photons positions near the center of the central pixel, causing the peak seen in the histogram.

The high intensity spots histogram has a "v" shape in the center, with two lateral peaks just before a drop at the edges. This can be caused by two factors. First of all, spots with very high intensities are often constituted by two photons falling near one another. The second photon falling at the boundary of the spot area can shift the result of the COM calculation outwards. This leads to have an higher probability of finding centroids near the edges of the pixels. Moreover, the higher threshold on central pixels' intensities (HCPT) discards spots with high intensity in the central pixels. Therefore, the only high intensity spots reconstructed by the software are those generated by photons falling near the pixel edge, which split more the charge cloud among neighbouring pixels and thus have a lower signal in the central one.

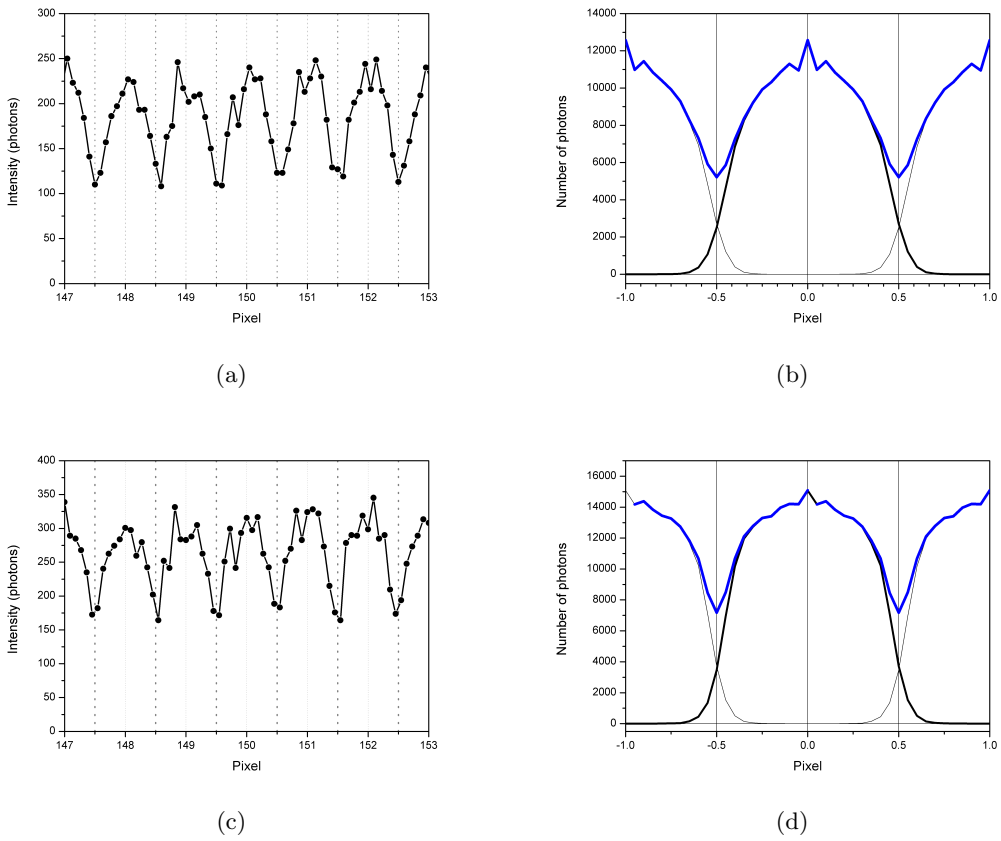

Figure 5.7: Sum along horizontal lines of reconstructed images using (a) medium intensity spots and (c) all spots and, (b) and (d), corresponding COM position histograms summed for adjacent pixels.

Oscillations projected along one direction

The profile oscillations due to the described effect were not visible in Figure 5.5 on the profile elaborated by the single photon counting algorithm. This was probably due to a smoothing caused by the integration along an inclined line and to the shift applied at each of the 18 profiles, obtained by the 18 groups of images acquired, in order to align them.

In order to study these oscillations, an integration along horizontal lines was performed, i.e. a zero slope was used, and no realignment was applied to the 18 different profiles before summing. The resulting profiles relative to an uniformly illuminated region of the images are depicted in Figure 5.7 (a) and (c), respectively for medium intensity spots and for all spots. In the same figure, the COM distribution histograms are repeated at one pixel distance and then summed together, to obtain a profile representing the mean

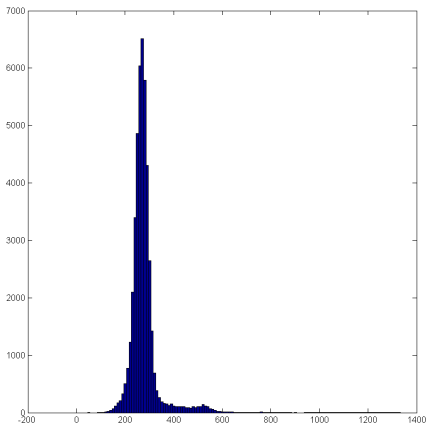

Figure 5.8: Spot intensity histogram for the ESRF test. The horizontal axis is in electrons.

oscillations expected by the COM histogram shape.
The experimental oscillation profile and the one obtained from the COM distribution histograms seem a lot alike. In particular the profile obtained with all spots seems flatter in the center of the pixels, as its histogram does. The variation between the center of the pixel and the edge is about 50% for both graphs obtained with medium intensity spots and slightly less for graphs obtained using all spots.
Thus the systematic error due to barycenter reconstruction is clearly the cause of these oscillations and many different ways to overcome this problem, which involve a correction of images once that this systematic error is known, are currently under study.

5.4 Test at ESRF

Images acquisition and parameters

A very fast test was carried out in ESRF during a beamtime. Some images were acquired and analysed with the single photon counting algorithm in order to study what are the specifical problems related to the use of this algorithm to elaborate experimental RIXS spectra. The spectra shown here are acquired at $\delta = 45°$ with vertical polarization of incoming light on an YBCO sample.
In order to have a very low photon density on each image, the exposure time was reduced to 40 seconds. This value is much lower than the usual exposure time of 5-10 minutes

used for the acquisition of images to be processed with the traditional algorithm, but it was necessary to avoid multiple events. 30 images were acquired, with a very small ROI around the interesting spectral lines, in order to reduce the readout time and to gain duty cycle. Furthermore, no hardware horizontal binning (see Section 3.3) was applied, contrary to the usual acquisition mode, in order to avoid the overlap of spots falling at a distance (in pixel) smaller than the number of pixels binned.

Due to the very low statistics, the number of subpixels was set to 3, otherwise a too low number of photons would be assigned to each channel, resulting in a very noisy line. Thus the result is not useful to test the resolution achieved on spectra but it is anyway interesting to evaluate the optimal photon flux and exposure time for the use of the single photon counting algorithm on images.

The spot size was set to 5×5, because, in this situation with low noise and very well known offset, it helps reducing the oscillations and the systematic errors (see Chapter 6 for the comparison between 3×3 and 5×5 spots for the 13.5 μm pixel). As it can be seen in Figure 5.8 the total number of double events (around 500 electrons) is very low compared to the big peak around 250 electrons, due to single events. The monochromaticity of the beam allowed to set thresholds on spot intensity at values very near to the expected single photon intensity, i.e. around 0.7 photons for the lower threshold and 1.3 photons for the higher one.

Spectrum

In Figure 5.9 the spectra are shown. The traditional algorithm was divided by 1.5, in order to keep into account the division of photons among a different number of channels (2 points per pixel for the traditional algorithm and 3 points per pixel for the single photon counting one) and vertically shifted to subtract the offset.

As it can be seen, due to low statistics, the photon counting spectra are very noisy. However, the spectrum is well elaborated when all spots are considered (orange line), while discarding multiple events, and thus discarding high intensity spots, would lead to lower the *dd* peak (blue line). As a matter of fact, even if the total number of multiple events is very low compared to single events, they all fall in the *dd* region, where the total intensity is higher. However, the interesting region of the spectrum is

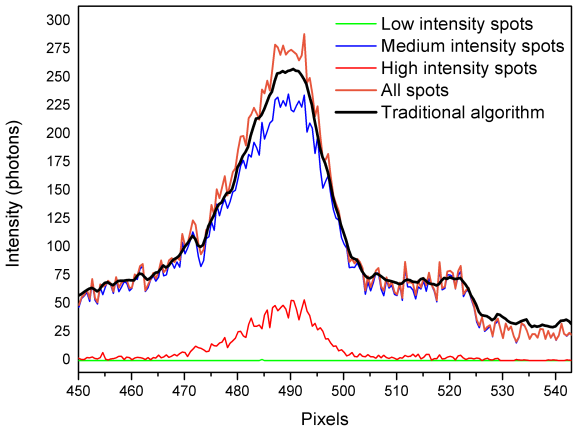

Figure 5.9: Spectra obtained by the test at ESRF.

often the one on the right near the elastic peak, that is not affected by multiple events and thus the presented experimental conditions can be considered suitable for analysing these low energy excitations.

5.5 Conclusions

The results of these experimental resolution tests show that the software actually works as expected, allowing to an excellent enhancement of the resolution. The estimated value of the achieved resolution is around 7 μm, while the traditional software's resolution is about 30 μm. Both values are slightly higher than what expected, probably due to some uncertainties occurring in the experiments, one of these being the exact slope value of the direction along which the integration has to be performed.

The tests on the software revealed also a problem for the future applications for spectroscopy, that is the possible presence of oscillations in the final spectra. This is caused by a systematic error introduced by the calculation, that is widely discussed in the next Chapter. Some methods to overcome this problem are currently under study.

Finally, the test performed at ESRF showed that the software guarantees a good elaboration of the spectrum but, how it was expected, the high intensity of the signal on peaks is actually a problem. In the regions of the image corresponding to high

intensity peaks, there is an high percentage of multiple events, that cannot be used correctly by the software for the centroid reconstruction. However, the acquisition configuration used for the test (i.e. a small ROI and an exposure time of 40 seconds) showed this problem only on the *dd* peak, which is the most intense part of all the spectrum. Therefore this exposure time may be useful anyway, in order to study low intensity regions in the spectra, such as the low energy excitations in cuprates.

Moreover, these problems become negligible in some experiments. An example is when the polarimeter is used to resolve the polarization of the light emitted by the sample. The polarimeter reflects only light with a particular polarization, and thus that component of the signal can be isolated and analysed. By using the polarimeter a big fraction of the total intensity is lost, reducing the photon intensity on the detector by a factor from 15 to 20. This reduction of the photon flux on the detector can allow to use a longer exposure time, gaining duty cycle and avoiding multiple events.

Chapter 6

Monte Carlo Simulations of Single Photon Detection

In addition to the resolution tests on the images acquired with the experimental setup in Milan, some Monte Carlo simulations were performed. Simulations were useful to confirm the gain in resolution already proved with experimental tests and to broaden the knowledge about the algorithm functioning. As a matter of fact, with simulated images the exact position of spots centroids is known and this allows to study the difference between the calculated positions of COMs and the real spot centers, evaluating the error introduced using the barycenter reconstruction.

This Chapter will show the most important results obtained with these simulations in terms of evaluation of the resolution enhancement achieved and study of the errors related to the centroid calculation.

The results of simulations performed with parameters similar to those of the resolution experiment will be discussed widely and compared to experimental data. Then, simulations concerning the 13.5 μm pixel size detector will be shown. Although the resolution test has still to be performed with this detector, it is worth to discuss briefly these simulations because in software's final application at ESRF images will be acquired by a 13.5 μm pixel size detector.

6.1 Monte Carlo simulation

In order to have some images on which carry out analysis under completely controlled conditions, a MATLAB script that simulates the generation and splitting of a charge cloud between neighbouring pixels was developed by Prof. Giacomo Ghiringhelli.

The software arranges the electrons inside the pixels following a statistical distribution determined by the mean spot shape, that, according to the analysis presented in Section 4.3 and to previous studies [39], was chosen as a bidimensional gaussian with 25 μm FWHM. The total number of electrons generated by a photon can vary, according to statistical noise, and has an average value of $N_{el} = E_{photon}[eV]/3.6[eV]$.

Thanks to this script two different kind of simulations were performed. First of all some images similar to the experimental ones were generated, by centering photons' spots in random positions on a wide image and then cancelling those spots that fall under a line, that represents the blade edge. This was useful to test the resolution enhancement achieved by the software, avoiding the many other contributions occurring in experiments as noise, non monochromaticity of the radiation emitted by the lamp and uncertainties about the optimal slope parameter.

The second application of the script was focused on understanding the systematic error introduced by the COM calculation on images, that, as already mentioned in Section 5.3, is the cause of the possible oscillations in the final spectra. This simulation generates many $N \times N$ matrixes, each one containing a single spot, whose center lies in the central cell. Spots are generated distributing their centers uniformly inside the central pixel. The value N, defined by the user, determines the spot size, in pixel, used to perform the COM calculation. Knowing the exact position of the centroid in each image, and calculating the COM of spots, the error involved in this calculation can be evaluated. Moreover, analysing the distribution of the calculated COMs, it can be studied how the error affects the COM distribution histogram. The last version of this software allows to introduce a readout noise on pixels signals and a baseline, in order to simulate an error on the offset subtraction.

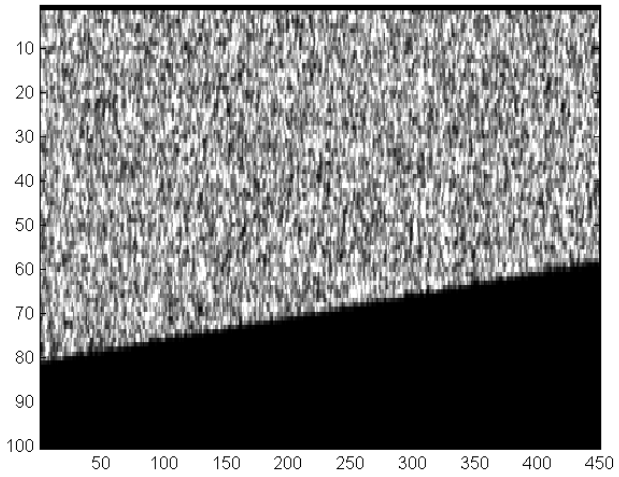

Figure 6.1: Sum of the 3000 simulated images analysed.

6.2 Simulation of resolution experiments

3000 simulated images of 450 × 100 pixels were generated with the software, each one with about 100 photons in the illuminated region. The sum of these images is depicted in Figure 6.1 and the result of the analysis is shown in Figure 6.2(a). The analysis were carried out using the same algorithm parameters used for experiments, (see Section 5.2), in order to have comparable results. However, these parameters are less critical on simulated images, thanks to the monochromaticity of the beam and the absence of noise.

The resolution enhancement is evident from the comparison between the profiles obtained using the traditional algorithm and the single photon counting one. The estimated resolution is about 25 μm with traditional algorithm and 2 μm with single photon counting. The resolution obtained with traditional algorithm is exactly the value that was expected using 25 μm FWHM gaussian shaped spots; this value of spatial resolution was already measured by other groups using experimental data [45] and this makes presented results on simulated images reliable. The excellent resolution achieved with single photon counting algorithm confirms the effectiveness of the developed software in enhancing resolution. The resolution of about 2 μm is near to the best value achievable using a COM calculation, as it will be shown in next Section. Furthermore, using 11 points per pixel, with pixels of 20 μm side, i.e. about 0.91 μm

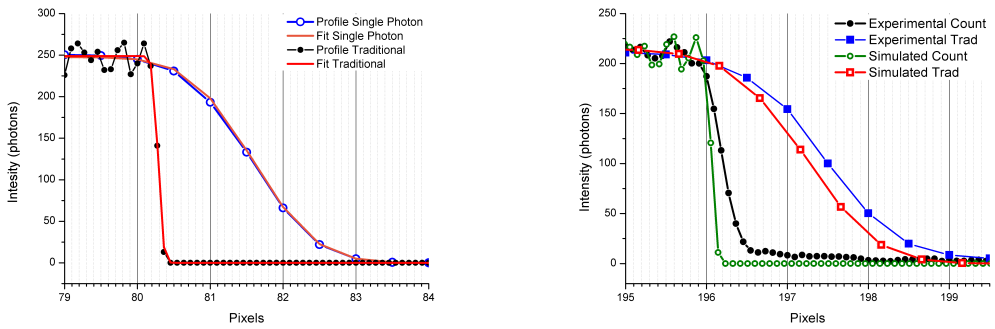

(a) Result of the resolution test on the simulated images.

(b) Comparison between the profiles resulting form the experiments and the simulations.

Figure 6.2: Results of the resolution test on simulated images and comparison with experimental data.

per point, an edge of a step function thinner than 2 μm is very difficult to resolve.

A further consideration on experimental data can be done comparing experimental profiles with those elaborated by simulated images. As it can be seen in Figure 6.2(b), the resolution achieved in experiments is worst using both traditional and photon counting algorithms. Both steps seem wider due to a constant contribution, of about 2.5 tenth of pixel, resulting in a loss of resolution of 5 μm in both cases. This suggests that this contribution is related to some uncertainties in the experiments, such as the slope of the line along which the integration is carried out, whose criticality was already discussed in Section 5.2. Another cause of error may be an imperfect alignment of the 18 profiles obtained by different runs.

The simulations can give information also about the oscillations detected in the experimental images after the elaboration with the single photon counting algorithm. As it can be seen in Figure 6.3(a), some oscillations very similar to those of Figure 5.7 arise if images are analysed with single photon counting algorithm using a $slope = 0$, in order to integrate the image along horizontal lines. These oscillations are fitted very well by the blue line, generated by repeating in each pixel the COM distribution histogram and summing these histograms where they overlap near the pixels' edge. The COM distribution histogram is shown in Figure 6.3(b). Presented results are obtained using only medium intensity spots, but the analysis with all spots gives exactly the same results, because, due to the absence of non-idealities in simulated images, only 0.5% of spots were discarded and classified as high intensity ones,

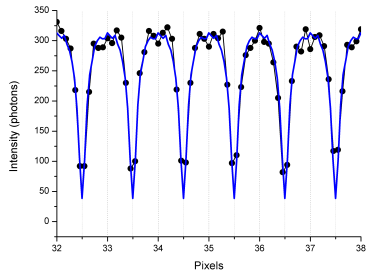

(a) Oscillations profile of simulated images analysed with the single photon counting algorithm and integrated along horizontal lines (black) and the oscillation profile obtained by the COM histogram.

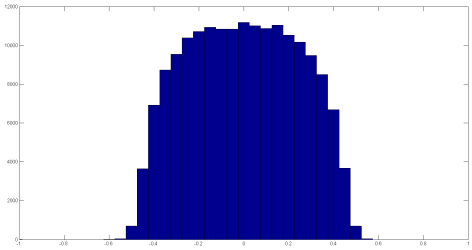

(b) COM distribution histogram resulting from the analysis on the simulated images.

Figure 6.3: Oscillations and COM distribution resulting from the simulations.

probably due to some multiple events.

6.3 Simulation of errors introduced by centroid calculation

Systematic and random error in resolution tests

Some simulations were performed in order to study the above mentioned artifacts introduced by the centroid reconstruction through the barycenter calculation. Many spots were generated distributing their centers uniformly inside the central pixel and the difference between the positions of the exact center of each spot and the calculated COM was studied. To perform this analysis the central pixel was divided in a 19×19 subpixels grid and 1000 photons were simulated hitting each subpixel. The simulations were performed using 3×3 pixel and 5×5 pixel for the spot size and 20 μm pixel size. A systematic error was detected, together with a random contribution due to the stochastic nature of the diffusion of electrons in the neighbouring pixels, which is reproduced by the Monte Carlo simulation.

Figure 6.4 shows the analysis results on spots of 3×3 pixel size. Figure 6.4(a) represents the modulus of the mean error caused by the COM calculation when the photon hits different positions of the central pixel. This error is always smaller than 1.3 μm and increases on pixel edges and vertices. Panel (b) shows the systematic error direction, always pointing towards the center of the pixel in this case. This is the cause of the COM distribution already shown: spot centers are shifted from the edges

towards the center, leading to a wide peak in the center of the central pixel and a depletion of its edges. The random error shown in panel (c) is almost constant and equal to 1 μm. The combination of the two errors gives about 2 μm of total error on the COM calculation, that is exactly the resolution found in our simulated resolution test above discussed.

In panel (d) is depicted the COM distribution inside the central pixel and in panel (e) the same distribution is shown along one direction; the red line shows the expected oscillations due to this COM distribution, after summing the single histogram build on a pixel with the tails of neighbouring ones. These are very similar to what already found in experiments. To have a direct comparison, panel (f) is the experimental result of COM distribution that corresponds to panel (e).

These simulations were very important to understand the cause of the oscillations and to discard the previous hypothesis of an hardware contribution to the oscillations.

The same analysis was carried out using 5×5 pixels spots and some results are shown in Figure 6.5. The systematic error in this case is reduced to zero, as it can be seen in Figure 6.5(a), where all arrows directions are uncorrelated, suggesting that the systematic error that shifts COM positions is negligible in this situation. The fourfold symmetry of the figure is just a consequence of the algorithm used, that works only on a quarter of pixel and then mirrors the result to fill the entire pixel. The random error, depicted in Figure 6.5(b) is the same of the 3×3 spot case, being 1 μm all over the pixel.

The COM distribution inside the central pixel and the oscillations arising along one direction are depicted in Figures 6.5(c) and (d). They are both very flat, as predictable by the absence of any systematic error in the centroid reconstruction. Comparing this result with the previous one, obtained with 3×3 spots, it could be stated that 5×5 spots allow a better centroid reconstruction, because of the contribution of second neighbour pixels, which accumulate a charge that is not negligible.

However, larger spots lead to an higher probability of multiple events, because each spot occupies a wider area and it is therefore more probable to have another photon falling near this area. This is an important problem for applications, because it requires a lower photon flux on the detector or a lower exposure time, resulting in a loss of duty cycle and efficiency. Furthermore, these results are obtained without

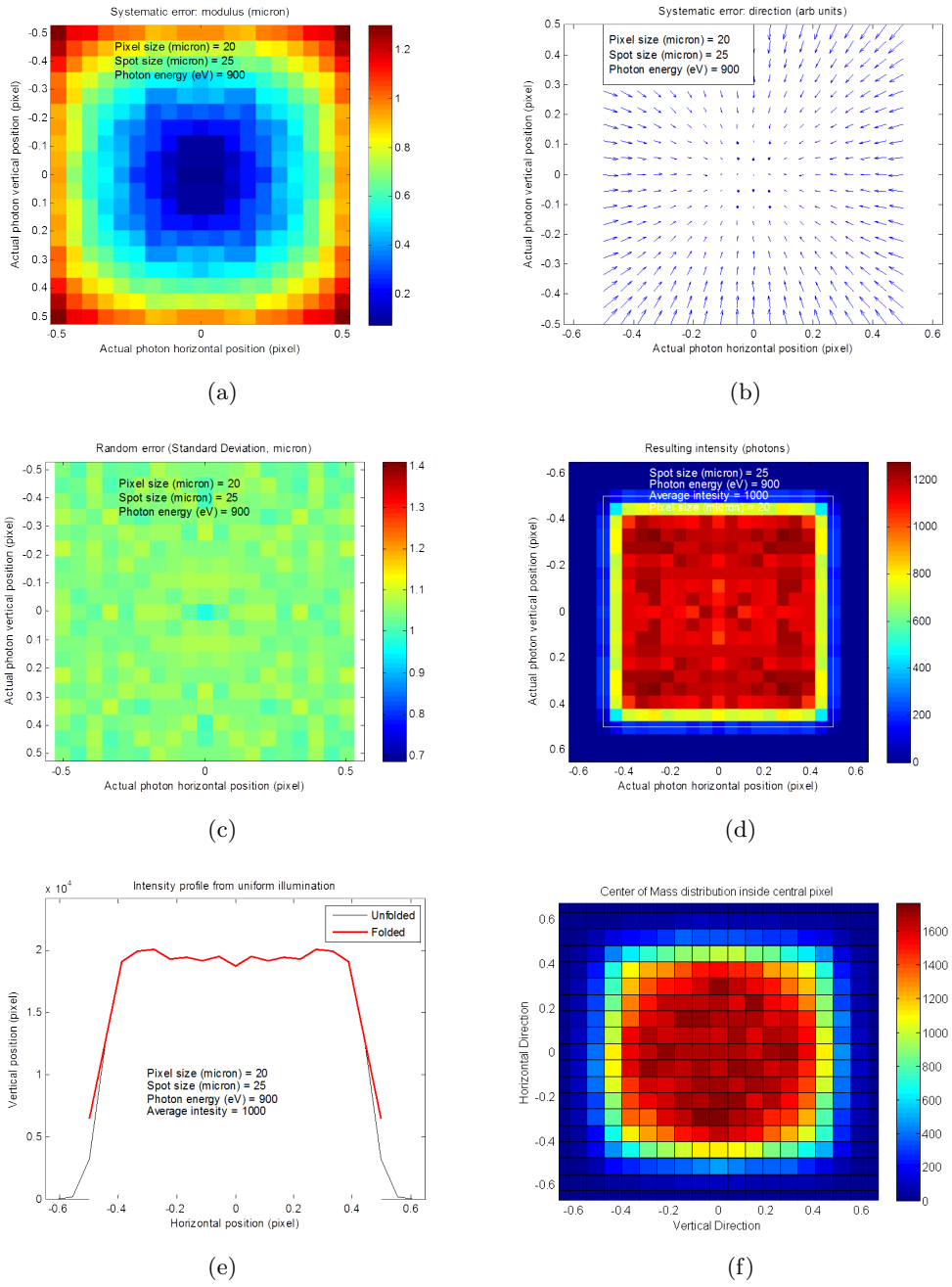

Figure 6.4: Analysis of errors arising from COM calculation with a 3×3 spot on 20 μm pixels.

introducing in simulations the effect of noise or errors on offset subtraction, while these contributions are expected to be higher than the charge accumulated in second neighbouring pixels. Therefore, considering 5×5 spots could cancel the systematic error, but errors due to noise and offset would increase, leading to an overall loss in resolution and less robust results. These two contributions will be described in next

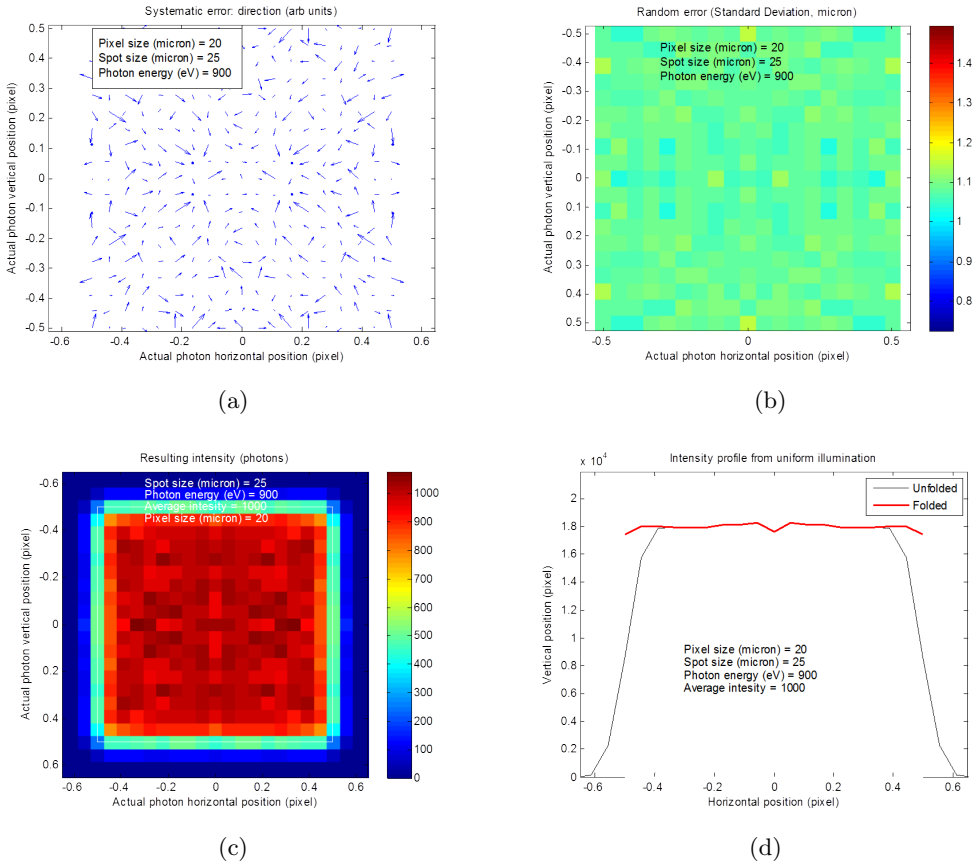

Figure 6.5: Analysis of errors arising from COM calculation with a 5×5 spot on 20 μm pixels.

Section, referring to 13.5 μm pixels, where theoretically these effects on second neighbouring pixels should be lower than in the 20 μm pixel case. As a matter of fact, being nearer to the center of the spot, lateral pixels should accumulate more charge and thus being less sensible to errors.

However, considering the small errors introduced by the barycenter calculation on 3×3 spots, the excellent resolution achieved with this spot size and the problems that would arise using wider spots, the best solution for future applications with 20 μm pixel size could be to use 3×3 spots; if necessary, the oscillations may be canceled by using the information about the average oscillations provided by the COM distribution histogram to correct the image after the elaboration.

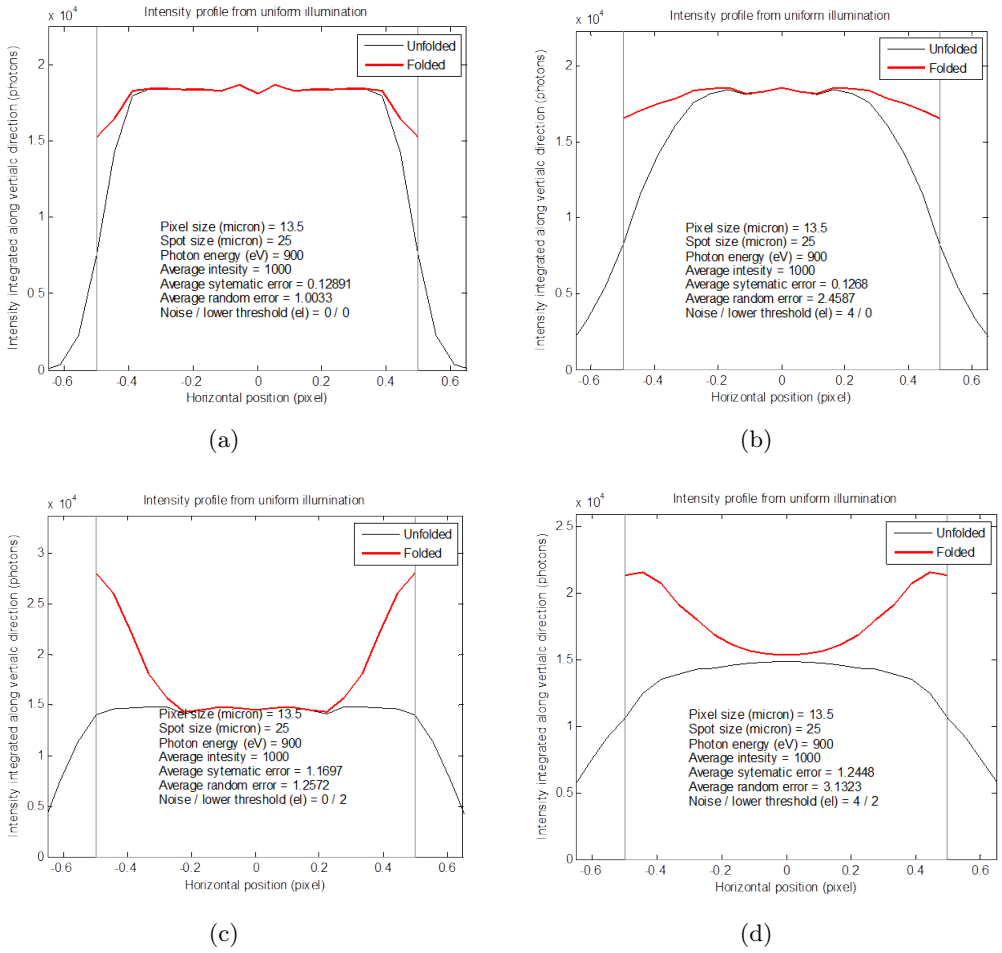

Figure 6.6: Effect of noise and offset on COM distribution inside the central pixel (black line) and oscillations (red line) with 13.5 μm pixels and 5×5 spots.

Simulation of errors with 13.5 μm pixel

Similar simulations were performed using 13.5 μm as pixel size and introducing a readout noise and an error on offset subtraction, to study the robustness of the results.

The results with 3×3 spots are shown in Figure 6.7. The COM distribution shows a complete depletion near the pixels edges, resulting in oscillations of the same amplitude of the signal. With 13.5 μm pixel size the portion of the charge cloud that is accumulated in the second neighbouring pixels is bigger than in the 20 μm case, therefore neglecting the outer pixels leads to bigger systematic errors. As a matter of fact, the average of the the systematic error is 1.6 μm, while in the 20 μm case the systematic error never exceeded 1.3 μm (Figure 6.4(a). The introduction of the readout noise (Figure 6.7 (b)), of an offset error, or of both (Figures (c) and (d)) does not change the shape

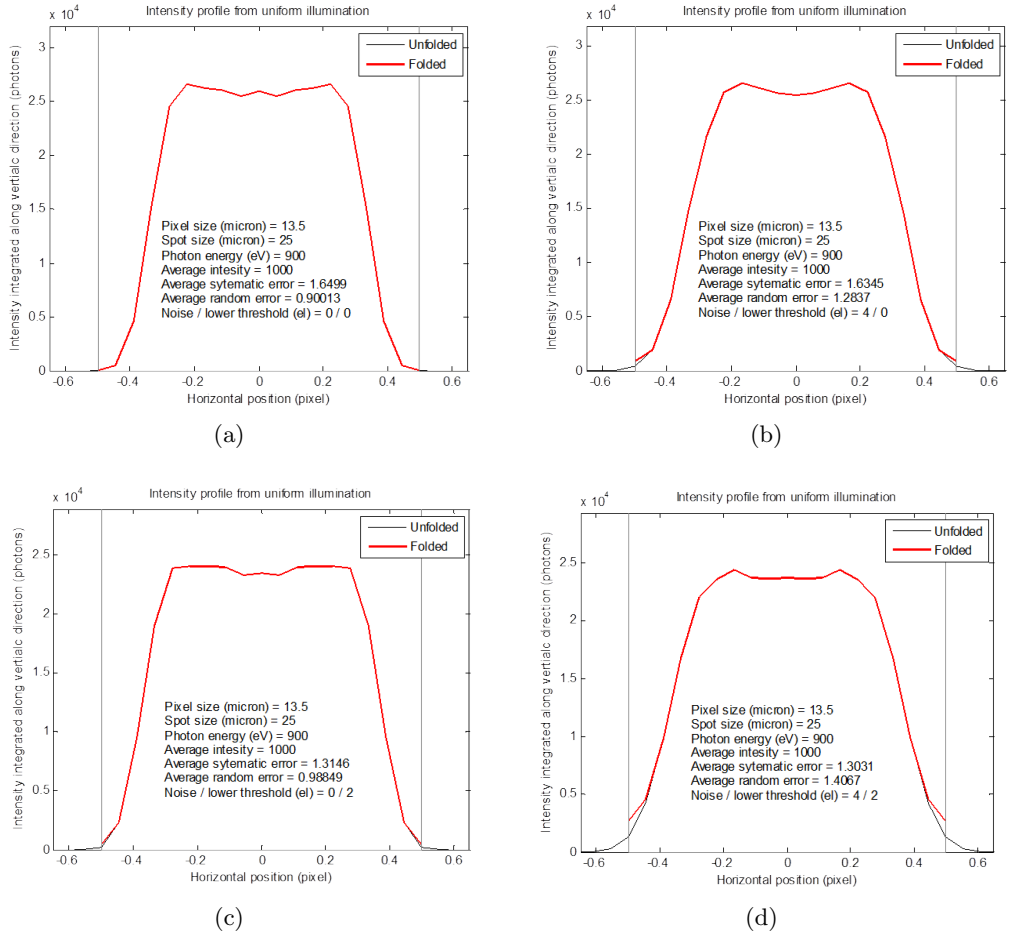

Figure 6.7: Effect of noise and offset on COM distribution inside the central pixel (black line) and oscillations (red line) with 13.5 μm pixels and 3×3 spots.

of the distribution. As a matter of fact, with 3×3 spots, only pixels with high signal are considered, that are not affected by these contributions. It is interestingly that the systematic error average decreases with the introduction of a positive error of 2 electrons on the offset value (panel (c) and (d)). This situation is similar to that already discussed in Figure 4.6, where it is shown that an offset error could compensate the systematic error on the COM reconstruction. On the other hand, random error increases in panel (b) and (d) because of the noise, as it is obvious.

The results of the simulation on 5×5 spots are shown in Figure 6.6. Panel (a) confirms that, without any noise or error in offset subtraction, wider spots allow to reduce the systematic error to almost zero. However, panels (b), (c) and (d) show how these results are very sensible to noise and offset, due to the low signal in outer pixels. As a matter of

fact, the introduction of the readout noise (panel (b)) makes the average random error reach 2.5 μm, which is a value higher than any other found with 3×3 spots. Even the systematic error increases from 0 to 1.2 μm as soon as an error on offset is introduced. This systematic error has a big influence on the COM distribution, that changes from the flat shape in the upper part of the image, to a strongly convex shape in the lower part, where a positive error of 2 electrons is introduced on the offset.

6.4 Conclusions

The test on simulated images confirmed the resolution enhancement achievable through the use of the single photon counting algorithm developed. The resolution achieved by the analysis on simulated images was even higher than that obtained by the experiments, being around 2 μm.

However, this result was obtained in an ideal case, without any noise and other uncertainties, which are present in the experiments and can affect the resolution estimation. Moreover, it must be stressed that also the profile obtained by the analysis of simulated images through the traditional algorithm is narrower than the one obtained with experiments. This suggests the possible presence of a constant error in the experiments, due to the many different contributions which are very difficult to have under control. This discrepancy between experimental and simulated data has to be kept in mind for future tests.

The analysis on simulated images confirmed the presence of oscillations after the elaboration of the images with the software. The oscillations found in these tests on virtual images are very similar to those found using experimental data; therefore these oscillations are clearly an artifact introduced by the software and are not due to the detector structure.

This problem on the centroid reconstruction was further confirmed by other simulations performed to study the errors connected to the barycenter calculation. Spots' COMs are actually shifted towards the center of the pixels, causing the depletion of the pixels' edges. The error seems to decrease using a wider area for the spot reconstruction. With wider spots, and in an ideal case without noise, the resolution achievable could be even higher than what found here, due to the smaller

errors on the COM calculation.

This suggests that the discussed error is primarily caused by not considering the signal stored in the outer pixels of a spot, when a 3×3 matrix is considered for the reconstruction. However this does not mean automatically that wider spots guarantee smaller errors and negligible oscillations. As a matter of fact, the lateral pixels of a 5×5 matrix contain a very low signal inside them and thus are very sensible to noise and to possible other errors. Therefore, depending on the particular conditions, the COM distribution histogram can be severely affected, causing strong oscillations with a shape difficult to predict. Moreover, the average error on the COM calculation using a 5×5 can be even higher than that obtained with 3×3 spots, due to this higher contribution of uncertainties.

Many different methods for the centroid reconstruction are now under test and they bode well for a future elimination of the problem of the oscillations. However, using the described barycenter calculation it seems that oscillations are impossible to be canceled simply by choosing the right combination of parameters. Therefore some methods for the correction of these errors are under analysis. The simplest of these methods consists in the division of the elaborated image by another image (i.e. a matrix) representing the mean oscillations, obtained by the 3D COM distribution. This method should not lead to a big modification of the spectrum and ensures a robust method to overcome the oscillations problem. Other methods, such as a shift of every COM position according to the calculated errors may be too much sensible to uncertainties and thus could lead to a further loss in resolution.

Bibliography

[1] Luuk JP Ament, Giacomo Ghiringhelli, Marco Moretti Sala, Lucio Braicovich, and Jeroen van den Brink. Theoretical demonstration of how the dispersion of magnetic excitations in cuprate compounds can be determined using resonant inelastic x-ray scattering. *Physical review letters*, 103(11):117003, 2009.

[2] P Glatzel, M Sikora, and M Fernandez-Garcia. Resonant x-ray spectroscopy to study K absorption pre-edges in 3*d* transition metal compounds. *The European Physical Journal Special Topics*, 169(1):207–214, 2009.

[3] Masahiko Matsubara, Takayuki Uozumi, Akio Kotani, Yoshihisa Harada, and Shik Shin. Polarization dependence of resonant x-ray emission spectra in early transition metal compounds. *Journal of the Physics Society Japan*, 69(5):1558–1565, 2000.

[4] Luuk JP Ament, Michel van Veenendaal, Thomas P Devereaux, John P Hill, and Jeroen van den Brink. Resonant inelastic x-ray scattering studies of elementary excitations. *arXiv preprint arXiv:1009.3630*, 2010.

[5] Akio Kotani and Shik Shin. Resonant inelastic x-ray scattering spectra for electrons in solids. *Reviews of Modern Physics*, 73(1):203, 2001.

[6] Luuk JP Ament, Giniyat Khaliullin, and Jeroen Van den Brink. Resonant inelastic x-ray scattering on spin-orbit coupled insulating iridates. *arXiv preprint arXiv:1008.4862*, 2010.

[7] SG Chiuzbăian, G Ghiringhelli, C Dallera, M Grioni, P Amann, X Wang, L Braicovich, and L Patthey. Localized electronic excitations in nio studied with

resonant inelastic x-ray scattering at the Ni M threshold: Evidence of spin flip. *Physical review letters*, 95(19):197402, 2005.

[8] Giacomo Ghiringhelli, NB Brookes, E Annese, H Berger, C Dallera, M Grioni, L Perfetti, A Tagliaferri, and L Braicovich. Low energy electronic excitations in the layered cuprates studied by copper L_3 resonant inelastic x-ray scattering. *Physical review letters*, 92(11):117406, 2004.

[9] Jagdeep Singh, Carlo Lamberti, and Jeroen A van Bokhoven. Advanced x-ray absorption and emission spectroscopy: in situ catalytic studies. *Chemical Society Reviews*, 39(12):4754–4766, 2010.

[10] Cullie J Sparks Jr. Inelastic resonance emission of x rays: anomalous scattering associated with anomalous dispersion. *Physical Review Letters*, 33(5):262, 1974.

[11] Luuk JP Ament, Michel van Veenendaal, Thomas P Devereaux, John P Hill, and Jeroen van den Brink. Resonant inelastic x-ray scattering studies of elementary excitations. *Reviews of Modern Physics*, 83(2):705, 2011.

[12] Soleil. ring structure. http://www.synchrotron-soleil.fr/.

[13] Albert Hofmann. *The physics of synchrotron radiation*, volume 20. Cambridge University Press, 2004.

[14] David T Attwood. *Soft x-rays and extreme ultraviolet radiation: principles and applications*. Cambridge university press, 2000.

[15] Janos Kirz and David Attwood. X-ray data booklet. *X-RAY DATA BOOKLET*, page 13, 1986.

[16] M Minola. *Magnetic, orbital and charge fluctuations in layered cuprates studied by resonant soft X-ray scattering*. PhD thesis, Politecnico di Milano, Dipartimento di Fisica, http://hdl.handle.net/10589/74562, 2013.

[17] Shigemi Sasaki, Kazunori Kakuno, Takeo Takada, Taihei Shimada, Ken-ichi Yanagida, and Yoshikazu Miyahara. Design of a new type of planar undulator

for generating variably polarized radiation. *Nuclear Instruments and Methods in Physics Research Section A: Accelerators, Spectrometers, Detectors and Associated Equipment*, 331(1):763–767, 1993.

[18] M Moretti Sala, V Bisogni, C Aruta, G Balestrino, H Berger, NB Brookes, GM De Luca, D Di Castro, M Grioni, M Guarise, et al. Energy and symmetry of dd excitations in undoped layered cuprates measured by Cu L_3 resonant inelastic x-ray scattering. *New Journal of Physics*, 13(4):043026, 2011.

[19] Øystein Fischer, Martin Kugler, Ivan Maggio-Aprile, Christophe Berthod, and Christoph Renner. Scanning tunneling spectroscopy of high-temperature superconductors. *Reviews of Modern Physics*, 79(1):353, 2007.

[20] Pierre Monceau. Electronic crystals: an experimental overview. *Advances in Physics*, 61(4):325–581, 2012.

[21] G Grüner. The dynamics of charge-density waves. *Reviews of Modern Physics*, 60(4):1129, 1988.

[22] Tao Wu, Hadrien Mayaffre, Steffen Krämer, Mladen Horvatić, Claude Berthier, WN Hardy, Ruixing Liang, DA Bonn, and Marc-Henri Julien. Magnetic-field-induced charge-stripe order in the high-temperature superconductor $YBa_2Cu_3O_y$. *Nature*, 477(7363):191–194, 2011.

[23] J Chang, E Blackburn, AT Holmes, NB Christensen, Jacob Larsen, J Mesot, Ruixing Liang, DA Bonn, WN Hardy, A Watenphul, et al. Direct observation of competition between superconductivity and charge density wave order in $YBa_2Cu_3O_6$.67. *Nature Physics*, 8(12):871–876, 2012.

[24] Mathieu Le Tacon, G Ghiringhelli, Jiří Chaloupka, M Moretti Sala, V Hinkov, MW Haverkort, M Minola, M Bakr, KJ Zhou, S Blanco-Canosa, et al. Intense paramagnon excitations in a large family of high-temperature superconductors. *Nature Physics*, 7(9):725–730, 2011.

[25] G Ghiringhelli, M Le Tacon, M Minola, S Blanco-Canosa, C Mazzoli, NB Brookes, GM De Luca, A Frano, DG Hawthorn, F He, et al. Long-range incommensurate charge fluctuations in (Y,Nd)$Ba_2Cu_3O_{6+x}$. *Science*, 337(6096):821–825, 2012.

[26] JM Tranquada, BJ Sternlieb, JD Axe, Y Nakamura, and S Uchida. Evidence for stripe correlations of spins and holes in copper oxide superconductors. *Nature*, 375(6532):561–563, 1995.

[27] P Abbamonte, A Rusydi, S Smadici, GD Gu, GA Sawatzky, and DL Feng. Spatially modulated'mottness' in $La_{2-x}Ba_xCuO_4$. *Nature Physics*, 1(3):155–158, 2005.

[28] S-Wo Cheong, G Aeppli, TE Mason, H Mook, SM Hayden, PC Canfield, Z Fisk, KN Clausen, and JL Martinez. Incommensurate magnetic fluctuations in $La_{2-x}Sr_x$ CuO_4. *Physical review letters*, 67(13):1791, 1991.

[29] TR Thurston, PM Gehring, G Shirane, RJ Birgeneau, MA Kastner, Y Endoh, M Matsuda, K Yamada, H Kojima, and I Tanaka. Low-energy incommensurate spin excitations in superconducting $La_1.85Sr_0.15CuO_4$. *Physical Review B*, 46(14):9128, 1992.

[30] TE Mason, G Aeppli, and HA Mook. Magnetic dynamics of superconducting $La_1.86$ $Sr_{0.14}$ CuO_4. *Physical review letters*, 68(9):1414, 1992.

[31] K Yamada, CH Lee, K Kurahashi, J Wada, S Wakimoto, S Ueki, H Kimura, Y Endoh, S Hosoya, G Shirane, et al. Doping dependence of the spatially modulated dynamical spin correlations and the superconducting-transition temperature in La_{2-x} Sr_xCuO_4. *Physical Review B*, 57(10):6165, 1998.

[32] J Lorenzana and G Seibold. Metallic mean-field stripes, incommensurability, and chemical potential in cuprates. *Physical review letters*, 89(13):136401, 2002.

[33] G Seibold and J Lorenzana. Doping dependence of spin excitations in the stripe phase of high-T_c superconductors. *Physical Review B*, 73(14):144515, 2006.

[34] C Stock, WJL Buyers, RA Cowley, PS Clegg, R Coldea, CD Frost, R Liang, D Peets, D Bonn, WN Hardy, et al. From incommensurate to dispersive spin-fluctuations: The high-energy inelastic spectrum in superconducting $YBa_2Cu_3O_6.5$. *Physical Review B*, 71(2):024522, 2005.

[35] V Hinkov, Ph Bourges, S Pailhes, Y Sidis, A Ivanov, CD Frost, TG Perring, CT Lin, DP Chen, and B Keimer. Spin dynamics in the pseudogap state of a high-temperature superconductor. *Nature Physics*, 3(11):780–785, 2007.

[36] B Vignolle, SM Hayden, DF McMorrow, HM Rønnow, B Lake, CD Frost, and TG Perring. Two energy scales in the spin excitations of the high-temperature superconductor $La_{2-x}Sr_xCuO_4$. *Nature Physics*, 3(3):163–167, 2007.

[37] Elizabeth Blackburn, J Chang, AT Holmes, EM Forgan, MN Zimmermann, R Liang, and WN Hardy. Direct observation of charge ordering in underdoped YBCO in high magnetic fields, 2012.

[38] James R Janesick. *Scientific charge-coupled devices*, volume 117. SPIE press Bellingham, WA, 2001.

[39] ME Dinardo, A Piazzalunga, L Braicovich, V Bisogni, C Dallera, K Giarda, M Marcon, A Tagliaferri, and G Ghiringhelli. Gaining efficiency and resolution in soft x-ray emission spectrometers thanks to directly illuminated ccd detectors. *Nuclear Instruments and Methods in Physics Research Section A: Accelerators, Spectrometers, Detectors and Associated Equipment*, 570(1):176–181, 2007.

[40] George G Pavlov and John A Nousek. Charge diffusion in CCD x-ray detectors. *Nuclear Instruments and Methods in Physics Research Section A: Accelerators, Spectrometers, Detectors and Associated Equipment*, 428(2):348–366, 1999.

[41] Princeton Instruments. *PI-LCX:1300 handbook.*

[42] Nicola Pezzotta. Algoritmi avanzati per il trattamento dei dati grezzi di uno spettrometro per scattering anelastico di raggi X. Master's thesis, Politecnico di Milano - Dipartimento di Fisica, 2007/2008.

[43] A Abboud, S Send, N Pashniak, W Leitenberger, S Ihle, M Huth, R Hartmann, L Strüder, and U Pietsch. Sub-pixel resolution of a pnCCD for x-ray white beam applications. *Journal of Instrumentation*, 8(05):P05005, 2013.

[44] Joe M Davis. Statistical theory of spot overlap in two-dimensional separations. *Analytical Chemistry*, 63(19):2141–2152, 1991.

[45] MR Soman, DJ Hall, JH Tutt, NJ Murray, AD Holland, T Schmitt, J Raabe, and B Schmitt. Improving the spatial resolution of a soft x-ray charge coupled device used for resonant inelastic x-ray scattering. *Journal of Instrumentation*, 6(11):C11021, 2011.